

**PROCESSING AND CHARACTERIZATION OF NANOCELLULOSE  
COMPOSITES: THE LEAP FROM POLY(LACTIC ACID) TO  
POLYAMIDE 6**

by

**Caitlyn M. Clarkson**

**A Dissertation**

*Submitted to the Faculty of Purdue University*

*In Partial Fulfillment of the Requirements for the degree of*

**Doctor of Philosophy**



School of Materials Engineering

West Lafayette, Indiana

May 2020

**THE PURDUE UNIVERSITY GRADUATE SCHOOL  
STATEMENT OF COMMITTEE APPROVAL**

**Dr. Jeffrey P. Youngblood, Chair**

School of Materials Engineering

**Dr. Gregory T. Schueneman**

Forest Products Laboratory

**Dr. Carlos Martinez**

School of Materials Engineering

**Dr. Kendra Erk**

School of Materials Engineering

**Dr. John Howarter**

School of Materials Engineering

**Approved by:**

Dr. David Bahr

*This work is dedicated to my mother, whose relentless love and support I can never repay.*

## ACKNOWLEDGMENTS

I would like to thank my graduate research advisor, Dr. Jeffrey Youngblood. His mentorship in my research and professional career has been invaluable and I can easily say that I am a better engineer because of his guidance. His support and insightful ideas about my research enabled me to achieve research I am proud of. I would also like to thank my external research advisors, Dr. Greg Schueneman and Dr. James Synder for their continued support, inspiring conversations, and professional mentorship.

I would like to thank Dr. Carol Handwerker, who supported me in the NSF IGERT: Global Sustainability in Electronics program at Purdue. The space created by the IGERT program significantly broadened my research interests as well as my knowledge of sustainability. This program exposed me to subjects and people I would never have met otherwise and has shaped the way I think about my own research, science, and engineering's role in creating a sustainable, global economy.

I would also like to acknowledge and thank my graduate student mentors and collaborators. First, Dr. Gamini Mendis who was always a watchful and helpful mentor in the lab when I first arrived. Of all the grad students in my group, Gamini took the most interest in the new grad students and in seeing that they were settled and adjusted in the lab for which I am very grateful. Secondly, I would like to thank Dr. Reaz Chowdhury and Sami M. El Awad Azrak who have been exceptional collaborators during my time at Purdue. Lastly, Dr. Matthew Korey, my colleague and dear friend who has always lent an ear to hear out my thoughts and ideas. Matthew is an excellent teacher, invaluable friend, and colleague.

# TABLE OF CONTENTS

LIST OF TABLES.....	8
LIST OF FIGURES.....	9
LIST OF COMMON SYMBOLS & ABBREVIATIONS.....	12
ABSTRACT.....	13
1. INTRODUCTION.....	14
1.1 Nanocellulose Background.....	14
1.2 Putting Polymer Sustainability into Context.....	16
1.3 Polymer Nanocomposites General Context.....	19
1.4 Research Objectives and Scope.....	21
2. DRY-SPINNING OF CELLULOSE NANOCRYSTALS/POLY(LACTIC ACID) COMPOSITE FIBERS.....	23
2.1 Introduction.....	23
2.2 Materials and Methods.....	25
2.2.1 Materials.....	25
2.2.2 Dry-Spinning Method.....	25
2.2.3 Characterization of Dry-Spun Fibers.....	26
2.3 Results and Discussion of Dry-Spun Fibers.....	27
2.3.1 Surface Morphology.....	27
2.3.2 Crystallinity of Composite Fibers.....	29
2.3.3 Mechanical Performance and Micromechanical Modeling.....	32
2.4 Conclusions on Dry-Spinning of PLA Nanocomposite Fibers.....	36
2.5 Acknowledgments for Dry Spinning.....	36
3. MELT SPINNING OF CELLULOSE NANOFIBRIL/POLY(LACTIC ACID) COMPOSITE FIBERS.....	37
3.1 Introduction.....	37
3.2 Methods and Materials.....	39
3.2.1 Materials.....	39
3.2.2 Melt spinning and Post-Processing.....	41
3.2.3 Morphology and Dispersion.....	42

3.2.4	Fiber Crystallinity and Orientation .....	43
3.2.5	Tensile Properties .....	45
3.3	Results and Discussion .....	46
3.3.1	Nanoparticle and Surface Morphology .....	46
3.3.2	Crystallinity.....	47
3.3.3	Orientation.....	51
3.3.4	Mechanical Performance.....	54
3.4	Conclusions on the Melt-Spinning of PLA Nanocomposite Fibers.....	56
3.5	Acknowledgments for Melt-Spinning.....	57
4.	PRELIMINARY INVESTIGATION OF SMALL CONCENTRATIONS OF CNMS IN PLASTICIZED POLY(LACTIC ACID) .....	58
4.1	Introduction .....	58
4.2	Materials and Methods.....	59
4.2.1	Materials.....	59
4.2.2	Fourier Infrared Spectroscopy (FTIR).....	61
4.2.3	Microscopy.....	61
4.2.4	Characterization of Crystallinity.....	62
4.2.5	Heat Deflection Temperature.....	62
4.3	Results & Discussion .....	62
4.3.1	Nanoparticle Characterization .....	62
4.3.2	Appearance of Nanocomposites .....	66
4.3.3	Crystallinity.....	69
4.3.4	Heat Deflection Temperature of Nanocellulose/PLA Composites.....	71
4.4	Conclusions on Bulk Properties of PLA Nanocomposites .....	72
5.	SMALL CONCENTRATIONS OF CELLULOSE NANOFIBRILS AND CELLULOSE NANOCRYSTALS IN PLASTICIZED PLA: CRYSTALLIZATION KINETICS.....	73
5.1	Introduction .....	73
5.2	Materials and Methods.....	75
5.2.1	Materials.....	75
5.2.2	Processing of Nanocomposites .....	75
5.2.3	Methods for Thermal Analysis .....	79

5.2.4	Characterization of PLA Spherulites .....	79
5.3	Results and Discussion .....	79
5.3.1	Avrami Crystallization Kinetics .....	79
5.3.2	Effects on Melting Behavior .....	90
5.3.3	Nonlinear Hoffman-Weeks Extrapolation of the Equilibrium Melting Temperature .....	92
5.3.4	Nucleation Efficiency from Secondary Nucleation Theory .....	93
5.3.5	Crystal Morphology .....	96
5.4	Conclusions for Crystallization Kinetics .....	101
5.5	Acknowledgments for Crystallization Kinetics .....	101
6.	PRELIMINARY PROCESSING OF NANOCELLULOSE/POLYAMIDE COMPOSITES .....	103
6.1	Introduction .....	103
6.2	Methods and Materials.....	104
6.2.1	Materials.....	104
6.2.2	Exchanging CNCs from Water into Additives .....	104
6.2.3	Nylon 6 Nanocomposite Processing.....	105
6.2.4	Thermal Properties of Potential Additives and Nanocomposites .....	106
6.3	Results for Polyamide Processing.....	106
6.3.1	Thermal Properties of Polymers and Potential Additives .....	106
6.3.2	Nylon 6/CNC Composites.....	107
6.3.3	Thermal Properties of Nylon 6/CNC Composites .....	108
6.4	Summary and Future Work .....	111
7.	SUMMARY.....	112
	APPENDIX A: DRY-SPINNING POLY(LACTIC ACID) NANOCOMPOSITE FIBERS .....	114
	APPENDIX B: MELT SPINNING POLY(LACTIC ACID) NANOCOMPOSITE FIBERS .....	116
	APPENDIX C: POLYLACTIC ACID NANOCOMPOSITES .....	119
	APPENDIX D: POLYAMIDE NANOCOMPOSITES .....	128
	REFERENCES .....	138
	PUBLICATIONS .....	145

## LIST OF TABLES

Table 1.1 Environmental impacts of bio-polymers and petroleum-based polymers. All references in order from left to right along columns of data.....	17
Table 1.2 Polymer properties.....	19
Table 3.1 Thermal properties for three thermal histories.....	50
Table 4.1 CNM particle dimensions.....	66
Table 4.2 Summary of thermal properties for preliminary plasticized PLA nanocomposites.....	71
Table 5.1. Thermal properties measured from non-isothermal experiments.....	81
Table 5.2 Avrami isothermal kinetics data.....	84
Table 5.3 Surface energies of various materials.....	85
Table 5.4 Secondary nucleation theory parameters.....	95
Table 6.1 Table of thermal properties for polymers and potential additives for nylon 6 composites.....	107
Table 6.2 Thermal properties of nylon 6 composites.....	108

## LIST OF FIGURES

Figure 1.1 Transmission electron microscopy (TEM) images of A) CNCs B) CNFs. ....	15
Figure 1.2 Images of polyamide 12 (PA12)/CNC nanocomposites: (a) Neat PA12; (b) 10% phosphoric acid CNCs; (c) 10% sulfuric acid CNCs. This figure was adapted and republished with permission of Wiley.[8].....	20
Figure 2.1 Schematic of fiber testing geometry.....	27
Figure 2.2 Fiber morphology from SEM: A) Neat PLA fiber produced at 1 RPM, B) 15 RPM, C) 100 RPM. Fiber morphology at 25 RPM for different concentrations C) 0 wt%, E) 1 wt%, and F) 5 wt% at a fixed RPM. ....	28
Figure 2.3 DSC thermograms for nanocomposite fibers for A) different CNC concentrations and B) different screw speeds. Exothermic is up in all DSC thermograms. ....	30
Figure 2.4 Summary of thermal properties from DSC thermograms: A) Degree of crystallinity, $\chi$ and B) $T_{cc}$ versus CNC content.....	31
Figure 2.5 Mechanical properties of nanocomposites: A) Engineering stress-strain curves for select samples B) E versus CNC concentration and C) tensile strength versus concentration and D) Prediction of E for various micro-mechanical models. ....	35
Figure 3.1 TEM images of A) unmodified, mechanically fibrillated CNF and B) after chemical modification. C) FTIR of the CNF before and after chemical modification. ....	40
Figure 3.2 Process of exchanging CNFs into PEG.....	41
Figure 3.3 Birefringence in composite fibers for the composite 0.6 wt% mCNF-C12- 5 wt% PEG fiber is shown for draw ratios of A) 0X B) 2X C) 3X D) 4X E) 5X and F) 6X. Draw ratio was defined for this study as the change in length over original length. ....	42
Figure 3.4 Optical micrographs of 0.05% mCNF-C12 under cross-polarized light at A) approximately 45° and B) 0°/90° to demonstrate the analysis of fiber micrographs for estimating the orientation. ....	44
Figure 3.5 A-C) Optical micrographs at select concentrations of mCNF-C12. D-F) SEM images showing surface morphology with the addition of up to 1.3 wt% mCNF-C12. ....	47
Figure 3.6 DSC thermograms of A) As-spun PLA composite fibers and B) composites fibers at the maximum hot-draw ratio (6X for all but PLA control, which was 4X). Exothermic is up in all thermograms.....	49
Figure 3.7 Intensity vs. $2\theta$ extracted from 2D WAXS results for A) as-drawn fibers and B) hot-drawn fibers. Shows evidence of amorphous and crystalline content in composite fibers and that the $\alpha$ - phase is the predominate phase in composite fibers. ....	51
Figure 3.8 2D WAXS diffraction patterns for three thermal histories. ....	52

Figure 3.9 . A) Herman’s order parameter effect of hot-drawing and mCNF-C12 content at a constant PEG content of 5% (dotted lines are unmodified PLA) and B) visualization of the effect of hot-drawing on fibers with low mCNF-C12 and high mCNF-C12 content. ....	53
Figure 3.10 A) Elastic modulus vs mCNF-C12 content and B) strength-at-failure vs mCNF-C12 (filled shapes for up to 6X the original length). The 0 wt% mCNF-C12 refers to fibers with 5 wt% PEG and the PLA without any additives is shown as individual points (empty shapes). ....	54
Figure 3.11 Fracture faces of A) PLA fibers and B) 1.3 wt% mCNF-C12 composite fibers. Failure changes from a more ductile-like to brittle-like behavior. ....	55
Figure 4.1 Images of various solutions used containing A) unmodified, pristine sulfuric acid CNCs B) CNC-g-pla-C12 and C) CNF-g-pla-C12. From left to right, CNMs in solvent (water or ethanol), 600g/mol PEG, and CNMs/PEG after water removal at three concentrations denoted on image. 60	
Figure 4.2 TEM images of A) CNC from water B) mechanically fibrillated CNF from water C) modified mCNC-C12 D) and mCNF-C12 from PEG solution. ....	64
Figure 4.3 A) Summary of FTIR spectra of CNMs before and after chemical modification. B) FTIR spectra of chemically modified CNMs at a narrow wavenumber distribution showing evidence of primary peak confirming chemical modification. ....	65
Figure 4.4 Images of nanocomposite plaques prepared with various CNMs at 0.05%, 0.26%, and 0.55% nanocelluloses with 5% PEG. ....	68
Figure 4.5 DSC thermograms of the second heat on A) CNC nanocomposites B) mCNC-C12 nanocomposites, and C) mCNF-C12 nanocomposites. Exothermic is up in all thermograms. ....	70
Figure 4.6 Heat deflection data for slow-cooled, compression molded samples. ....	72
Figure 5.1 Polarized optical micrographs of cellulose nanocrystal (CNC) and polyethylene glycol (PEG) solutions at A) 1 wt% CNC, and B) 10 wt% CNC and cellulose nanofibril (CNF) in polyethylene glycol at C) 1 wt% CNF. ....	77
Figure 5.2 Non-polarized and polarized optical microscopy images of nanocomposites after compounding: A1-2) PLA, B1-2) PLA+5%PEG C1-2) 0.05% CNF-5%PEG-PLA, D1-2) 0.05% CNC-5%PEG-PLA, E1-2) 0.55% CNC-5%PEG-PLA F1-2) 0.05% Talc-5%PEG-PLA. ....	78
Figure 5.3 Experimental data for a 50°C/min cool followed by subsequent heating at 10°C/min. Exothermic is up in all thermograms. ....	81
Figure 5.4 Progression of Avrami analysis from isothermal data at 100°C: A) Experimental isothermal data, B) Crystallinity conversion versus experiment time and C) Avrami type plot of $\text{Log}(\text{Ln}(1-V_c))$ vs $\text{Log}(t-t_0)$ . Exothermic is upwards in all thermograms. ....	82
Figure 5.5 A) crystallization rate, $k$ , and B) Half-time, $\tau_{1/2}$ , versus $T_c$ for all compositions .....	87
Figure 5.6 Thermograms after isothermal crystallization at A) 90°C B) 100°C C) 110°C D) 115°C E) 120°C F) 130°C. Exothermic is upwards in all thermograms. ....	89
Figure 5.7 A) $T_{m1}$ versus $T_c$ and B) the crystallinity, $\chi$ , versus $T_c$ . ....	91

Figure 5.8 Summary plot of nonlinear Hoffman-Weeks estimation of the equilibrium melting temperature for all materials. ....	92
Figure 5.9 Plot of $\ln(1/\tau_{1/2})+U^*/(R(T_c-T_\infty))$ vs. $1/(T_c\Delta Tf)$ . ....	94
Figure 5.10. Scanning electron micrographs of chemically etched specimens isothermally crystallized at 130°C: A) Neat PLA, B) 5 wt% PEG, C) 0.05 wt% CNF-5 wt% PEG, D) 0.05 wt% CNC-5 wt% PEG, E) 0.55 wt% CNC-5 wt% PEG, and F) 0.05 wt% Talc-5 wt% PEG. Arrows indicate regions where “core-shell” morphologies (single bands which were preferentially etched away) formed in some of the spherulites. ....	98
Figure 5.11 Scanning electron micrographs of compositions isothermally crystallized at 90°C and then chemically etched for 4hrs in a 1:1 ratio of water and methanol with 0.025mol/L NaOH. Compositions are as follows: A) Neat PLA, B) 5 wt% PEG, C) 0.05 wt% CNF-5 wt% PEG, D) 0.05 wt% CNC-5 wt% PEG, E) 0.55 wt% CNC-5 wt% PEG, and F) 0.05 wt% Talc-5 wt% PEG. ....	99
Figure 5.12 Micrograph of 0.05 wt% CNF-5 wt% PEG isothermally crystallized at 130°C and then chemically etched. ....	100
Figure 6.1 A) Compression molded films of nylon 6 nanocomposites: nylon 6 (1), 5 wt% GMS (2), (3) 5 wt% GMS-0.55 wt% FPL CNC; (4) 5 wt% GMS-0.55 wt% BGU2 CNC. B) Plasticizer solutions used to prepare films: (1) GMS; (2) 1 wt% FPLCNC-GMS; (3) 5 wt% FPL CNC-GMS; (4) FPL CNC-GMS; (5) BGU.....	107
Figure 6.2 DSC thermograms of heating cycles of A) 5 wt% GMS-nylon 6 and B) 10 wt% GMS in nylon 6; both are with FPL CNC at 0.05 wt%, 0.25 wt% and 0.55 wt% and C) comparison of 5 wt% GMS and 5 wt%GMS/0.55 wt% CNC (BGU <sup>2</sup> CNC or FPL CNC). Exothermic is up in all DSC thermograms. ....	110

## LIST OF COMMON SYMBOLS & ABBREVIATIONS

### Common Symbols

$\chi$	Degree of crystallization, %
$\Delta H_m$	Enthalpy of melting, J/g
$\Delta H_m^\circ$	Theoretical enthalpy of melting, J/g
$\Delta H_c$	Enthalpy of crystallization, J/g
$\Delta H_{cc}$	Enthalpy of cold crystallization, J/g
$T_g$	Glass transition temperature, °C
$T_m$	Melting temperature, °C
$T_{cc}$	Cold crystallization temperature, °C
E	Young's elastic modulus, GPa
$\rho$	Density, g/cc
$\Phi$	Volume fraction

### Common Abbreviations

PLA	Poly(lactic acid)
PEG	Poly(ethylene glycol)
CNF	Cellulose nanofibrils
CNC	Cellulose nanocrystals
DSC	Differential scanning calorimetry
TGA	Thermal gravimetric analysis
DMA	Dynamic mechanical analysis
SEM	Scanning electron microscopy
TEM	Transmission electron microscopy
FTIR	Fourier infrared transmission spectroscopy

## ABSTRACT

Cellulose nanomaterials (CNMs) are abundant, renewable nanomaterials with unique properties leading to the exploration of these materials in industries such as the textile, electronics, automotive and packaging industries. In polymer-composites, they have been heavily investigated as mechanical reinforcements since CNMs have densities comparable to polymers, but high axial strength and stiffness. One of the key challenges in nanocellulose composites is processing. Early studies focused on solution processes that would be challenging to make industrially viable or they focused on water-soluble polymers with limited application space, while more recent research has emphasized melt-processing. Some of the key challenges to creating CNM/polymer composites are overcoming temperature stability differences and chemical compatibility.

This thesis concentrates primarily on poly(lactic acid) (PLA). PLA is a biopolymer derived from corn known for its use as 3D printer filament, biomedical applications, and packaging. The focus for PLA was two-fold: 1) to improve mechanical properties like stiffness and strength, and 2) to drive the crystallization rate, in turn leading to improvements in properties. Two projects for creating PLA nanocomposite fibers were explored, with the second leading to the development of a generalizable process for the solvent-less dispersion and distribution of CNMs into polymers. In the first project, a dry-spinning process for creating nanocomposite fibers was developed. In the second project, a melt-spinning process was developed in which CNMs were exchanged from their native solvent (water) into a known plasticizer which acted as a compatibilizer and processing aid as well. By exchanging the CNMs, no solvents were spent in the melt-processing step and the plasticizer served multiple functions during processing, but also served a final purpose in the composite as well. The fiber spinning projects fell under the first direction for PLA. The process developed became the basis for a preliminary investigation into the bulk properties of plasticized PLA. Since the process produced very small concentrations of CNMs in PLA, concentrations typical of commercial heterogeneous nucleation agents, the crystallization kinetics were investigated for very small concentrations in plasticized PLA; this fell under the second direction for PLA. Both the first and second set of projects under the two directions suggest that small concentrations of PLA can be effective in modifying composite properties. Lastly, the plasticizer method was investigated in a preliminary study on nylon 6 where the primary goal is to create dispersed nanocomposites.

# 1. INTRODUCTION

## 1.1 Nanocellulose Background

Cellulose nanomaterials (CNMs) encompass a wide variety of cellulose-based nanoparticles. Their exceptional properties, inherent abundance and renewability, and non-toxicity are all motivations that have driven research with these nanomaterials. Applications for these materials and their composites include uses in the packaging, automotive, and electronics industries<sup>[1,2]</sup>. CNM's and their polymer composites have been shown to enhance thermal properties,<sup>[3,4]</sup> gas barrier behavior,<sup>[5]</sup> as well as mechanical performance<sup>[6]</sup>. The diverse application space for these materials continues to expand as methods to process these materials and chemically modify them are developed.

CNMs are natural polymer nanoparticles that come from cellulose-containing resources like wood, cotton, fungi or bacteria<sup>[2]</sup>. Natural cellulose is comprised of amorphous and crystalline regions. During the isolation of these nanoparticles, the CNMs are subjected to a combination of chemical and mechanical treatments where the material is purified, homogenized, and refined<sup>[1]</sup>. Depending on the treatments, different types of nanoparticles can be obtained with different properties (e.g. aspect ratio, surface chemistry, etc.). One common method of refinement is acid hydrolysis<sup>[1,2]</sup>. Sulfuric acid, which creates a negative charge on the surface of CNM's, is very common in acid hydrolysis processes as the electrostatic repulsion between nanoparticles results in a more stable dispersion<sup>[2,7]</sup>. Furthermore, CNMs differ with cellulose source material; i.e. bacterial cellulose will produce different microfibrillar cellulose structures than wood-based cellulose which translates to differences in the nanoparticles isolated from these two sources<sup>[2]</sup>. Two important classes of CNMs are cellulose nanocrystals (CNCs) and cellulose nanofibrils (CNFs), which are the focus of the current work. CNCs, like those in Figure 1.1 A, are rigid rod-like nanoparticles while CNFs are long fibrillar, flexible nanoparticles (Figure 1.1 B). Both are high aspect ratio nanoparticles and due to their small size have a high surface area to volume ratio that composites take advantage of<sup>[1]</sup>.

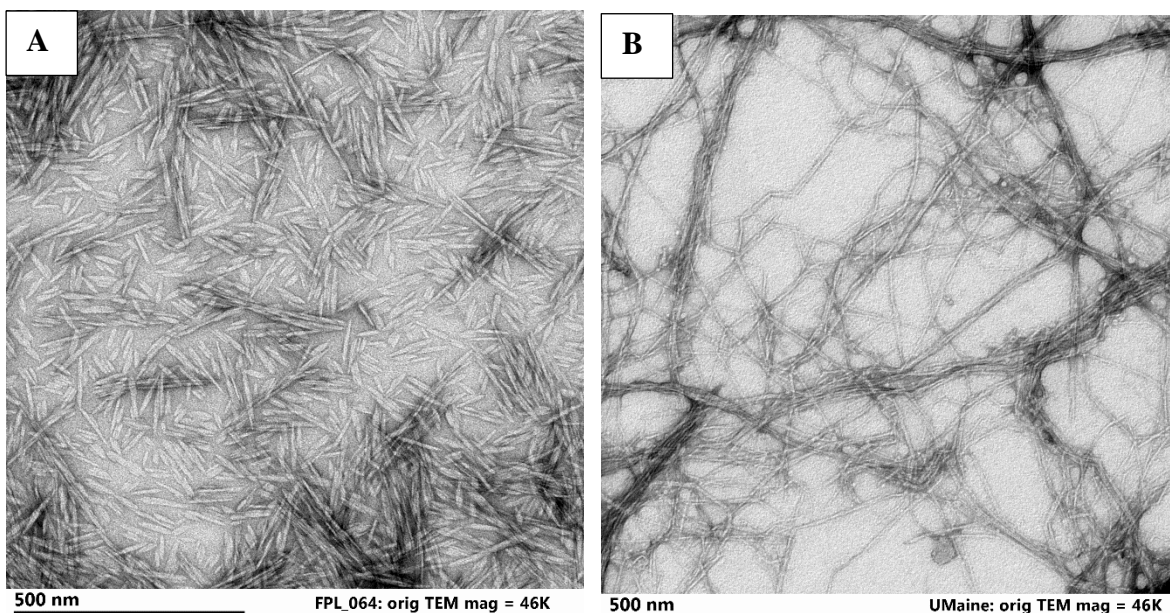


Figure 1.1 Transmission electron microscopy (TEM) images of A) CNCs B) CNFs.

CNCs are high-aspect-ratio nanoparticles with dimensions between 5-20 nm wide and 20-500 nm long and crystallinities between 54-88%<sup>[2]</sup>. In wood-CNCs, such as those used in this dissertation, these nanoparticles are typically produced from the acid hydrolysis of cellulose after it has been cleaned of lignin and hemicellulose in a pretreatment phase<sup>[2]</sup>. One of the most common variants is sulfuric acid hydrolysis CNCs. However, other variants include phosphoric acid CNCs, which are less susceptible to browning during nanocomposite processing<sup>[7,8]</sup>. CNCs are anisotropic in their mechanical, optical, and thermal properties. CNCs have a high axial elastic modulus, 57-145 GPa, and transverse elastic modulus, 18-50 GPa as well as high strength (although this has not been experimentally validated yet to the best of the author's knowledge)<sup>[2]</sup>. Additionally, CNCs are birefringent. When viewed through cross-polarized film, oriented CNC films can exhibit direction or angle-dependent color and CNC solutions exhibit Schlieren or "finger-print" structures when agitated<sup>[2]</sup>. Research has shown the CNCs and CNC films can exhibit high modulus, strength, thermal conductivity, and low coefficients of thermal (CTE) and hygroscopic (CHE) expansion<sup>[2-4,9,10]</sup>.

CNFs are also high-aspect-ratio nanoparticles but are significantly larger. CNFs are 4-100 nm wide, but can have lengths over 10  $\mu\text{m}$ <sup>[1]</sup>. These nanoparticles are typically much less crystalline than their CNC counterparts. CNFs typically is a good mechanical reinforcement in polymers due to their high entanglement density, which can be seen in Figure 1.1 B<sup>[2]</sup>. These

bigger nanoparticles are typically lower cost compared to CNCs since they are after only subjected to mechanical treatments, however, oxidized versions exist; for example, 2,2,6,6-tetramethylpiperidine-1-oxyl radical (TEMPO) CNF.

## **1.2 Putting Polymer Sustainability into Context**

One of the appeals of using bio-polymers like poly(lactic acid) (PLA) or CNCs/CNFs is that they are renewably sourced; both materials are derived from natural resources. However, these materials are not inherently more sustainable compared to petroleum alternatives due to the expenditure of resources over the course of the material or product life cycle. The life cycle comprises of the extraction of raw resources, processing, and manufacturing of those resources to create a material or product, its distribution and use phases, and its end of life (landfill, reuse, recycling, etc.). When discussing life cycles, the entire life cycle is not always considered; for instance, the production of polymer resins which can be used for a variety of different products, is usually cradle-to-gate. A cradle-to-gate analysis covers the production of raw resources through the manufacturing phase while “cradle-to-grave” covers through the entire life cycle. The accumulated environmental impact from the life cycle of a product can be determined by applying the life cycle assessment (LCA) methodology to account for various material and energy inputs/outputs throughout the course of a product life. The idea of conducting an LCA is to use that information to direct changes that will increase sustainability. Common environmental impact indicators from LCA are the global warming potential (GWP) in CO<sub>2</sub> eq. (sequestered heat by greenhouse gases relative to CO<sub>2</sub>), acidification potential (acidification of soil and nutrient depletion), abiotic depletion potential (i.e. fossil fuel depletion), and freshwater ecotoxicity potential. The GWP and waste generation for various polymers is shown in Table 1.1. For highly ubiquitous, commercialized products like polyethylene (PE), polyethylene terephthalate (PET), polyvinyl chloride (PVC) or polypropylene (PP), the waste generated (2015) is also provided<sup>[11]</sup>. Packaging applications, which account for 146 million tons of plastic produced yearly (2015), are a primary target for PLA<sup>[11]</sup>. Many packaging polymers, like PP, PE, and PET also account for a large amount of the plastics waste generated every year (Table 1.1).

Table 1.1 Environmental impacts of bio-polymers and petroleum-based polymers. All references in order from left to right along columns of data.

Polymer	GWP kg CO <sub>2</sub> eq/kg	Waste generation (2015) 10 <sup>6</sup> tonnes	Ref.
Nanocellulose (CNF)	0.7-3.1 <sup>^</sup>	-	[12]
CNF (Carboxymethylation treatment)	99	-	[12,13]
CNF (enzymatic or no treatment)	0.79-1.2	-	[12,13]
CNC (acid hydrolysis)	29.64	-	[12,14]
PLA	0.6*, 1.4-2.3**	-	[11,15,16]
Low Density Polyethylene	2.2*, 1.3-2.3**	57	[11,15,16]
High Density Polyethylene	1.9*, 1.0-1.5**	40	[11,15,16]
Polyethylene Terephthalate	2.7*, 2.2-2.7**	32	[11,15,16]
Polypropylene	1.9*, 1.1-2.0**	55	[11,15,16]
Polyvinyl Chloride	2.4*, 1.9-2.5**	15	[11,15,16]

<sup>^</sup> Many LCAs on nanocelluloses, CNCs or CNFs, are available for lab-scale/pilot-scale plants. The largest functional unit (1-ton production) for a sulfite pulp-based nanocellulose is reported in this table.

\*Cradle to gate (factory-resin)<sup>[15]</sup>

\*\*Cradle to gate plus end of life; range shown for multiple common scenarios on petroleum-based resin products. All petroleum-based polymers assumed to be landfilled. <sup>[16]</sup>

Several LCAs have been conducted on nanocelluloses, with cradle-to-gate analyses, yielding GWPs as low as 0.75 kg CO<sub>2</sub> eq/kg and as high as 1120 kg CO<sub>2</sub> eq/kg <sup>[12]</sup>. The materials selected were chosen as these materials are thought to best represent the CNCs and CNFs used in this dissertation. The GWP range for a 1-ton function unit of CNF from sulfite pulp was 0.7-3.1 kg CO<sub>2</sub> eq/kg and the range for 1 kg functional unit of CNF for three conditions (untreated, enzymatic treatment, and carboxymethylation) was 0.79-99 kg CO<sub>2</sub> eq/kg <sup>[12]</sup>. CNCs from an acid hydrolysis process using bleached kraft pulp was 30 kg CO<sub>2</sub> eq/kg <sup>[12]</sup>. Generally, it appears that the addition of a chemical-based treatment, like carboxymethylation or TEMPO-oxidation result in higher GWP because of the addition of additional chemicals and solvents, however, these pretreatments can also reduce the amount of energy required for fibrillation in mechanical processes<sup>[12]</sup>. The LCA conducted by the Forest Products Laboratory is informative in this regard,

as the GWP is quite large compared to the CNF LCAs. This is largely due to the production of sodium hydroxide (NaOH), a chemical used to neutralize the CNCs after acid hydrolysis, and electricity use<sup>[12,14]</sup>. Considering the relatively high GWP of some nanocelluloses investigated in the literature, there is room for improvement in these processes which have largely been conducted at lab-scale and are scaled up for the LCA. However, these early analyses are key in identifying the areas for design which could have the largest impact on the environment.

The GWP of various polymers, biologically derived and petroleum derived, is shown in Table 1.1 for two scenarios: one cradle-to-gate and the other cradle-to-gate plus disposal. The GWP of PLA for the cradle-to-gate scenario from NatureWorks LLC, the largest PLA producer (2020), is the lowest when compared to petroleum-based polymers (data from 2014)<sup>[15]</sup>. This low GWP is largely due to the carbon sequestration in growing corn, the resource used to produce the lactic acid monomer for PLA, in addition to other by-products that are used in the food industry like cooking oil<sup>[15]</sup>. Considering the scenario which incorporated end-of-life emissions into a cradle-to-gate LCA, the GWP of PLA is of comparable range to petroleum-based polymers. The range shown for PLA is for multiple scenarios where it is landfilled or composted. Due its molecular structure, this material can degrade/compost to release an additional 1.6 kg CO<sub>2</sub> eq/kg plastic and, potentially, exceed the environmental benefits or credits from carbon sequestration early in its life cycle<sup>[16]</sup>.

Neither study accounted for additional manufacturing steps or use which may be equally or more important in determining the GWP of a PLA product compared to a petroleum-based polymer product simply because of the difference in polymer properties (Table 1.2). While comparable in some of its properties (tensile strength for instance), PLA is very brittle compared to other polymers and has a very low heat deflection temperature (HDT) which will be discussed in subsequent chapters. Moreover, it has a higher density than polymers like PE or PP which are used in food packaging. The key implication is that, to create a product with comparable performance, the weight of the PLA product may be much higher and result in negative environmental impacts downstream in its life cycle.

Creating polymer composites to modify the properties of the polymer is a common strategy to achieve better performance regardless of polymer source (natural vs. petroleum) but is not a guarantee that the composite will have a lower environmental impact. Hervy *et al.* demonstrated that PP/glass fiber (GF) reinforced composites could exhibit lower environmental impact

compared to a product made of neat PLA or a CNF/epoxy composite in a cradle-to-grave analysis for an automotive product<sup>[17]</sup>. Some important considerations in this study were the processing methods, which are different for GF/PP composites and CNF/epoxy composites. PP is a thermoplastic that can be injection molded, while epoxy thermoset composites are primarily laid up using vacuum-assisted forming methods; the latter is more resource intensive (consumable items used). There were higher environmental impacts (GWP and abiotic depletion potential) associated with the expenditure of consumable items in the production of CNF/epoxy composites in the study by Hervy *et al.*<sup>[17]</sup>. This is not to say that CNF or CNC-based composites cannot be more environmentally friendly, only that materials and products need to be evaluated on a case by case basis, especially where some technologies may be premature. Should the GWP of CNCs and CNFs remain relatively high, even after significant development, the improvements in composites might still justify the use of these materials.

Table 1.2 Polymer properties.

Polymer	HDT (°C)	Tensile Strength (Mpa)	Young's Modulus (Gpa)	Elongation (%)	Density (g/cc)	Ref.
Nanocellulose (CNCs)	-	-	57-145	-	1.5	[2]
PLA	49 - 52	47 - 70	3.3 - 3.6	2.5 - 6	1.24 - 1.27	[18]
PE (LDPE and HDPE) *	121	20.7 - 44.8	.621 - .89	200 - 800	0.939 - 0.960	[18]
PET**	70	51.8 - 63.8	2.79 - 3.01	270 - 330	1.29 - 1.39	[18]
PP***	100	27.6-41.4	0.89-1.55	100-600	0.89-0.91	[18]
PVC****	92	37.7-43.9	2.2-3.1	40-80	1.29-1.45	[18]

\* low density polyethylene (LDPE) and high-density polyethylene (HDPE)

\*\* polyethylene terephthalate (PET)

\*\*\* polypropylene (PP)

\*\*\*\* polyvinyl chloride (PVC)

### 1.3 Polymer Nanocomposites General Context

Polymer nanocomposites have been prepared for several polar and non-polar engineering polymers by solution processing<sup>[19,20]</sup>, melt-processing<sup>[6,8]</sup>, solvent-assisted processes<sup>[21]</sup>, in situ

polymerization<sup>[22,23]</sup>, and milling<sup>[7]</sup>. PLA in particular has been widely studied, perhaps in part because it is a good candidate for an entirely renewable polymer/nanocellulose composite (PLA is a biopolymer derived from corn)<sup>[6,21,24–27]</sup>. This dissertation explored nanocomposites made primarily of PLA, but also polyamide 6 (nylon 6). As each chapter in this dissertation provides a thorough introduction to the nanocomposite system and the processes implemented, this section will provide a brief overview to give context to the work as a whole.

Processing of nanocomposites poses several challenges that have been previously alluded to. For the context of this work, it comes down to several interrelated issues: the difference in thermal stability between the polymer and CNM that can complicate processing, inherent differences in chemical compatibility as nanocelluloses are very hydrophilic compared to many engineering polymers and overcoming agglomeration issues either upon drying or in processing with the CNM slurry. The thermal stability of CNMs begins to degrade around 200-250°C which is why polymer nanocomposites processed at high temperatures, like polyamide 11<sup>[7]</sup> or polyamide 12<sup>[8]</sup> turn yellow or brown after being exposed to high temperatures (Figure 1.2). Moreover, CNCs tend to hydrogen bond strongly with neighboring CNCs, especially when dried and so re-dispersing them can be challenging. Several methods are common in the literature for addressing the problems facing polymer nanocomposites. One method is to surface modify the CNMs through the

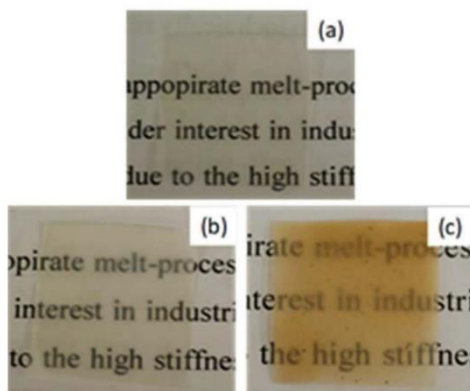


Figure 1.2 Images of polyamide 12 (PA12)/CNC nanocomposites: (a) Neat PA12; (b) 10% phosphoric acid CNCs; (c) 10% sulfuric acid CNCs. This figure was adapted and republished with permission of Wiley.[8]

hydroxyls available on the nanocellulose surface. Several studies have grafted various chemical groups to the surface such as PLA<sup>[28]</sup> to tune the hydrophilicity of the nanoparticles which inherently prefer water. These methods have shown varying degrees of success<sup>[27,29,30]</sup>. Similarly,

using CNCs with different surface groups from the acid hydrolysis process, like those discussed previously for polyamide 11 and polyamide 12 can also address these issues<sup>[7,8]</sup>. Another method is to coat the CNCs with a material that can shield the CNCs from each other and, ideally, is compatible with the polymer matrix<sup>[31,32]</sup>. A last and important method is to use an additive, such as a plasticizer, as a processing aid and compatibilizer to carry CNMs into the polymer melt<sup>[21]</sup>.

#### **1.4 Research Objectives and Scope**

The overarching goal of this work was to develop new processing methods for creating nanocellulose/polymer composites. Naturally, the nanocomposites produced by these methods were characterized and assessed in terms of their target properties which were driven by a specific application or interest.

The initially targeted application space for this work was in fibers. The goal of the first two projects was to create high strength and high stiffness fibers using a continuous, scalable process. The benchmark was to obtain similar specific stiffness and specific strength to fiberglass by using CNMs as reinforcements in polymers such as PLA and polyvinyl alcohol (PVOH). If the benchmark was met, then considerable weight savings in fiber-reinforced composites, like those used in aerospace, could be made. One of the benefits of using a nanocellulose reinforced polymer is that polymers are very affordable (dollars/lbs vs. hundreds of dollar/lbs) and very low density (1-1.5g/cc) already.

In the first iteration of the fiber spinning project, a solution-based fiber spinning process was envisioned. Solution spinning processes are used commercially for polymers like Kevlar and poly(acrylonitrile) (PAN), which is commonly a precursor to carbon fiber. For nanocellulose composites, the idea was to develop a solution spinning processes that would facilitate orientation along the fiber axis during processing and enable high CNC loading. In the first project, trying to maximize CNC loading was a primary effort as previous solution-spinning efforts had shown CNC concentration to be important in maximizing properties<sup>[33]</sup>. In the second iteration of this project, a melt-spinning process was developed. There are several reasons for the change to a melt process. 1) Melt-spinning is a simple process as it only relies on heat transfer while solution processes also depend on mass transfer (solvents evaporating or diffusion from the fiber to solidify). 2) Melt-spinning is much faster than solution spinning processes. 3) Melt-spinning processes typically do not release volatiles into the air like solution processes. The second project emphasized the

importance of alignment along the fiber axis and instead focused on smaller concentrations of CNMs, but hot drawing to facilitate alignment. Both projects examined PLA as the primary phase in the nanocomposite fibers.

Working with PLA, the scope of the research expanded to include other properties such as the HDT and the crystallization rate. The HDT of PLA is close to its  $T_g$ , around 50-60°C. The goal of the preliminary study exploring the effects of different types of CNCs at different concentrations was to determine if these materials could be used to improve the HDT to expand the potential application space for these materials. This project led naturally to the investigation of CNCs and CNFs in plasticized PLA. The method developed for the melt-spinning process enabled very small concentrations of CNC and CNF to be dispersed in PLA and for the combined effect of a plasticizer and a CNM on the crystallization kinetics to be studied. Lastly, since the method to create the melt-processed PLA nanocomposites was successful, the final preliminary study aimed to see if the process could be adapted to create other nanocellulose/polymer composites. Nylon 6 was chosen as it is particularly challenging in processing due to its high melting point that is within the thermal stability limit of unmodified CNMs.

## **2. DRY-SPINNING OF CELLULOSE NANOCRYSTALS/POLY(LACTIC ACID) COMPOSITE FIBERS**

All lab work performed in this chapter was done by Caitlyn Clarkson. All writing was done by Caitlyn Clarkson. Dr. Youngblood, Dr. Schueneman, and Dr. Snyder advised on research directions and provided editing and guidance on all writing.

This chapter contains content reproduced with permission from C. M. Clarkson, G. T. Schueneman, J. F. Snyder, J. P. Youngblood, *Green Mater.* 2018, 6, 6.

### **2.1 Introduction**

Fiber spinning is commercially used to produce many synthetic fibers. Three primary commercial techniques are described in the literature which are melt-spinning, and the two primary solution processes: dry-spinning and wet-spinning. Melt spinning produces fibers at the highest production rate by the simplest process. A polymer is melted and extruded through a spinneret into a cooler where it then undergoes any number of post-processing steps. Similarly, in dry-spinning, solutions of polymer and solvent are extruded from a spinneret. However, dry-spinning is a more complex process as solidification depends on solvent evaporation which in turn depends on many variables including the solution composition and concentration of constituents and processing variables such as temperature. The slowest process is wet-spinning where the solution is extruded into a miscible solvent bath and solidification occurs by diffusion of the fiber solvent into the bath solvent. These processes offer different advantages. For instance, solution spinning processes offer lower operating temperatures and the ability to process polymers that do not melt or flow-easily.

Nanocellulose reinforced polymer composites have been explored for fiber applications due to the large stiffness and strength gains in low cost, commodity polymers<sup>[6,33-35]</sup>. Solution spinning processes are the primary method to produce CNC nanocomposite fibers. These studies focus primarily on polymers soluble in water and water-miscible organic solvents such as acetone/dimethylacetamide to address challenges<sup>[33,35-37]</sup>. A study on polyvinyl alcohol and cellulose nanocrystal composite fibers produced by gel spinning obtained improvements in tensile strength and Young's modulus with hot drawing<sup>[35]</sup>. In cellulose acetate fibers, the elastic modulus increased by 637 % and the tensile strength increased by 137 % with the addition of 34 wt% CNC

<sup>[33]</sup>. However, the maximum alignment was achieved around 30 wt% after which the alignment was constant and CNC content alone determined the mechanical performance<sup>[33]</sup>. The CNC concentration at which the transition from alignment-dependent to CNC-loading controlled properties varies between polymers as aggregation of the nanocellulose will change with polymer system and processing. A ductile to brittle failure transition may accompany the aforementioned change as was observed in dry-spun CA-CNC fibers with the addition of CNC and a reduction in strain at failure was observed at as little as 2.5 wt% CNC <sup>[33]</sup>.

Poly(lactic acid) (PLA) is a sustainably sourced alternative to many industrially available polymers but is insufficient in mechanical performance. PLA fiber is primarily melt-spun, but the dry-spinning of PLA has been explored previously from solvents such as chloroform and trichloromethane <sup>[38-41]</sup>. Tensile strengths were as high as 2.3 GPa and elastic moduli were as high as 15 GPa have been observed for dry-spun poly(lactic acid) fibers<sup>[41,42]</sup>. However, melt fracture and heavy surface texturing is also observed in dry-spun fibers<sup>[38]</sup>. Alternatively, direct-injection of a CNC/water solution into a polymer melt has been employed to produce fibers with the end goal of creating films<sup>[43]</sup>. This study reported good dispersion in the fibers, however, the introduction of water during processing can create issues such as the development of bubbles due to solvent evaporation and residual water may be leftover.

In the present study, dry-spinning of CNC/PLA composite fibers (as opposed to melt-spinning and wet-spinning) was explored as an option for producing CNC composite fibers as it could enhance CNC dispersion in the polymer matrix for unmodified CNC, provide lower processing temperatures which are essential to prevent thermal degradation of CNC, and eliminate water from poly(lactic acid) processing which can degrade molecular weight. To understand the viability of this process for producing high strength, high stiffness fibers from CNC/PLA fibers were produced and the surface morphology, crystallinity, and mechanical properties of the reinforced fibers were investigated. To the best of our knowledge, these properties and this system have not been reported.

## 2.2 Materials and Methods

### 2.2.1 Materials

CNC slurry at 11.8 wt % (Batch 2014-FPL-CNC-064, 1 wt% sulfur on dried sodium CNC-form) in water was received from University of Maine (Orono, ME, USA), the distributor for nanocellulose manufactured by the USDA Forest Service- Forest Products Laboratory (FPL) (Madison, WI, USA) who produces the material. Dimethylformamide (DMF) was purchased from Sigma-Aldrich, St. Louis, MO, USA. NatureWorks 6202D fiber-grade polylactic acid (PLA) for fibers and non-wovens was purchased from a distributor, Jamplast Management Co., Ellisville, MO, USA. Resin pellets were dried at 80°C for 24 hrs before use. DMF was dried over molecular sieves for 2-3 days before use. Solvent exchange of the CNCs from water into DMF was performed on a rotary evaporator at 50 Torr to get a solution of approximately 8.5 wt% CNC. Thermogravimetric analysis (TGA) was used to confirm that water had been removed from the solvent/CNCs solution because water can initiate chain scission in PLA and thus lower the molecular weight.

CNC/PLA solutions were prepared at a fixed concentration of polymer in solution, 30 wt%, and varying CNC content to achieve a final concentration of 1 wt%, 3 wt%, and 5 wt% CNC in the composite fiber. Solutions were prepared by first mixing the appropriate quantity of CNC/DMF solution into the quantity of DMF needed to make a 30 wt% PLA solution. A homogenous solution was achieved by first mechanically mixing the CNC/DMF solutions and then ultrasonicated to further disperse the CNC in solution. Ultrasonication on a Branson Sonifyer was performed for 1 minute at 30 % amplitude with a 1-second pulse and 1-second rest to avoid damaging the CNC. Under vigorous mechanical stirring, the final concentration of PLA in DMF was achieved by elevating the temperature to 80-90°C while dissolving the polymer. Higher concentrations of CNC could not be achieved because of a large increase in solution viscosity that inhibited the mechanical mixing of the polymer pellets into solution.

### 2.2.2 Dry-Spinning Method

Direct-winding fiber spinning was used to produce dry-spun fibers. Fiber spinning was performed on an Xplore 5cc twin-screw micro-compounder with a continuous feed hopper, 90° turn, and funnel-tapered (conical V-taper) 250 µm orifice. A multiple temperature profile was

employed for spinning where the top to bottom barrel temperatures were 100 °C, 110 °C, and 115 °C, respectively. The polymer solutions were loaded into the pre-warmed barrel and allowed to compound at low speed (5 rpm) for a maximum of two hours until a spinnable viscosity was achieved. The extrusion speed of the fibers was varied by altering the screw-speed of the compounder; screw-speeds of 1, 5, 25, 50, and 100 rpm were initially investigated. Fibers were collected directly from the orifice during the spinning process on a winding mandrel. The take-up speed of the winding mandrel was 150 rpm and was held fixed for all processes. Before testing, all fibers were dried in a vacuum oven at 70 °C for several hours to ensure all residual solvent and any water absorbed from the atmosphere were removed.

### **2.2.3 Characterization of Dry-Spun Fibers**

Optical microscopy images of as-spun fibers were taken on a Carl Zeiss (Axio Observer A1) inverted light microscope. Spinning conditions produced fibers with diameters from 20 µm to 80 µm. Individual fiber diameters were measured for tensile test analysis.

Scanning electron microscopy (SEM) was utilized to image fiber surfaces on an XL40 FE-SEM. Samples were prepared by first sputter coating surfaces with gold-palladium to provide a conductive barrier to dissipate charge from the organic media. For high-resolution images of organic fibers, a 3-5 keV accelerating voltage and a working distance of 10-15 mm was selected.

Thermal data was collected on a Thermal Analysis (TA) Instruments Q2000 differential scanning calorimeter (DSC). Heat-cool-heat temperature ramps were conducted at 10 °C/min in nitrogen. The average sample size was 6 +/- 2 mg and three samples per experiment.

Tensile testing of the fibers was performed on a TA Instruments Q800 dynamic mechanical analyzer (DMA). Stress/strain data was collected from a force ramp at 0.3 N/min and 0.001 N pre-load. To avoid pinch off during clamping and make sample loading easier, the carding configuration in Figure 2.1 was adapted to conduct tensile tests<sup>[24]</sup>. Fibers were selected at random from dry fiber bundles and the fiber diameter was measured before carding to screen specimens for fiber diameter and bin them for easier comparison of experimental parameters. The pattern below was printed onto heavy cardstock to use as a template and a hole punch was used to remove the center of the cardstock. After screening, the fibers were sectioned into 25.4 mm pieces for carding. The 25.4 mm long pieces were secured along the primary axis of the template and high-strength epoxy was used to secure the fiber. The final gauge was 6.2 +/- 1.1 mm length. From

optical microscopy images, the true gauge length and minimum diameter of the fiber were recorded for calculation of the engineering stress and engineering strain.

### 2.3 Results and Discussion of Dry-Spun Fibers

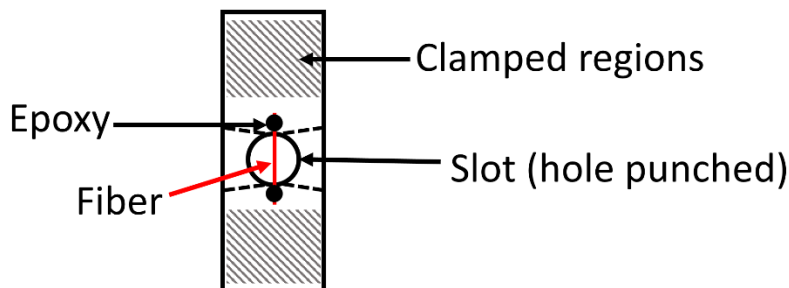


Figure 2.1 Schematic of fiber testing geometry.

#### 2.3.1 Surface Morphology

Mild to moderate melt fracture was observed on dry spun fibers as seen in Figure 2.2. By tuning the extrusion speed relative to the take-up/winding speed, the surface morphology of the fiber was seen to change, as seen in Figure 2.2. For slow screw speeds, the fiber morphology was relatively smooth with random dimpling across the fibers. By increasing the screw speed, the surface textures became much rougher with the onset of sharkskin (Figure 2.2 B&E) which transitioned to more moderate distortion at 100 rpm screw speed (Figure 2.2 C). Large scale distortion, like gross melt fracture, is thought to occur when an instability in the die forms that cannot be resolved<sup>[45]</sup>. For surface textures like sharkskin, the instability is thought to occur within the region of the die exit as the result of a cohesive failure and wall-polymer adhesion failure, while severe (melt) fracture is believed to be caused by fluid instabilities within the die which then propagate downstream<sup>[45]</sup>. Sharkskin melt fracture has been connected to many experimental factors including temperature, composition, die geometry, and extrusion and winding speeds<sup>[45-47]</sup>.

With those factors in mind, the experiment was designed to facilitate fiber diameter and drawing rather than to tune specific surface morphologies. A concentration of 30 wt% polymer in solution was chosen after preliminary studies showed stable jet formation and 115°C maximum temperature was chosen to facilitate solvent evaporation. In the case of melt spinning, increasing temperature has been shown to relieve melt fracture as the molecular mobility increases with increasing temperature and thus polymer will relax more rapidly after stretching and shearing

within the die and at the exit<sup>[46]</sup>. However, in dry-spinning, increasing temperature also increases solvent evaporation and could result in an increase in concentration which may have the opposite effect on melt fracture. Both were held constant as the effect of CNC content was the primary interest. Interestingly, CNC content did not appear to have a significant effect on surface texture despite some data which suggests that by promoting slip, melt fracture can be mitigated. CNCs are shear thinning and may promote slip, but in this case, did not appear to reduce melt fracture, but could have shifted the onset of severe sharkskin to lower screw speeds/extrusion speeds. This is possible because of the increase in solution viscosity with increasing CNC content at sufficiently high shear rates. Additionally, a conical v-tapered orifice with a diameter of 250  $\mu\text{m}$  was employed. It has been shown that zero-length or short length orifices like the one employed in the present study can contribute to the onset of melt fracture because the length of the die does not allow sufficient relaxation of the polymer and sharp entry angles create flow instabilities as the polymer is compressed and stretched inside the die. Increasing the extrusion rate or the polymer concentration can both exacerbate this effect as the polymer relaxation rate depends on how quickly it is deformed and how high the molecular mobility of the solution is.

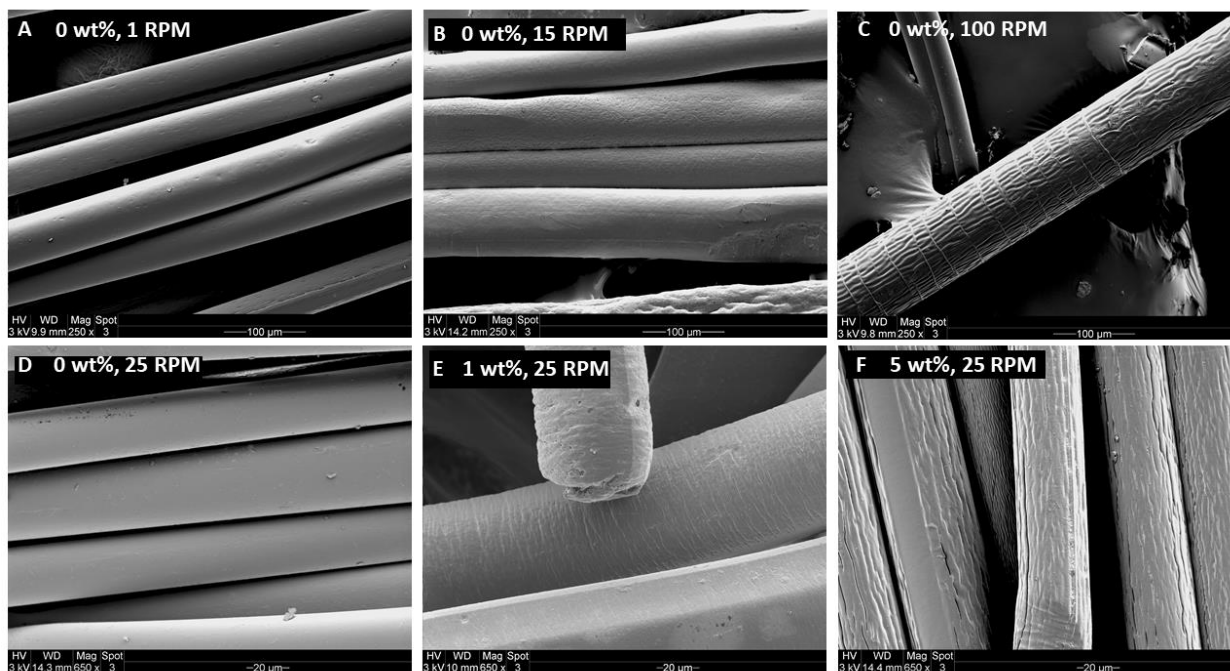


Figure 2.2 Fiber morphology from SEM: A) Neat PLA fiber produced at 1 RPM, B) 15 RPM, C) 100 RPM. Fiber morphology at 25 RPM for different concentrations C) 0 wt%, E) 1 wt%, and F) 5 wt% at a fixed RPM.

### 2.3.2 Crystallinity of Composite Fibers

Crystallinity was examined as a function of the processing history and composition in the as-spun fibers using DSC. Representative DSC thermograms are shown in Figure 2.3 A-B. All specimens exhibited a single melting peak despite a double melting peak being common in polylactides and PLA nanocomposites [43,48]. A double melting peak can be indicative of melt recrystallization in which imperfect crystals from the process melt at a lower temperature, re-crystallize to form new crystals during the heating scan, and subsequently re-melt at higher temperature [43]. This second peak, which occurs at temperatures 5-10°C lower than the primary melting peak, was absent in all dry-spun fibers which, in combination with the high melting point of 166 +/- 1.7 °C, suggested that stable crystals formed in the dry-spinning process or during cold crystallization upon heating.

Upon heating, the polymer can undergo crystallization above the glass transition temperature if the polymer reaches a temperature at which the molecular mobility is high enough for molecules to rearrange. PLA typically exhibits this phenomenon after rapid cooling because molecular chains do not have sufficient time to crystallize. Since total crystallization depends on nucleation and growth rate, both should be maximized to achieve the highest crystallinity possible. Cold crystallization peaks are evident in the DSC thermograms, though the degree of cold crystallization varied significantly with CNC content and screw speed. In the thermograms, a cold crystallization peak was observed for many combinations of conditions, as seen in Figure 2.3. However, some conditions, such as the 5 wt%, produced large cold crystallization peaks, while other conditions produced very small cold crystallization peaks, such as the 1 wt% (Figure 2.3 A). Highly crystalline fibers are desirable as the strength and stiffness should both increase with increasing crystallinity. It may be desirable to eliminate or reduce cold crystallization by achieving a high crystallinity during fiber spinning. This could reduce time and resources spent on post-processing steps and avoid shape and property changes that may happen during use if the fiber is heated above its glass transition temperature.

The degree of crystallinity,  $\chi$ , was calculated from Equation 2.1, where  $\Delta H_m$  is the enthalpy of melting, the  $\Delta H_c$  is the enthalpy of cold crystallization (the opposite sign of  $\Delta H_m$ ),  $\Delta H_m^\circ$  is the theoretical maximum enthalpy of melting (assumed to be 93 J/g), and  $x_{cnc}$  is the weight fraction of

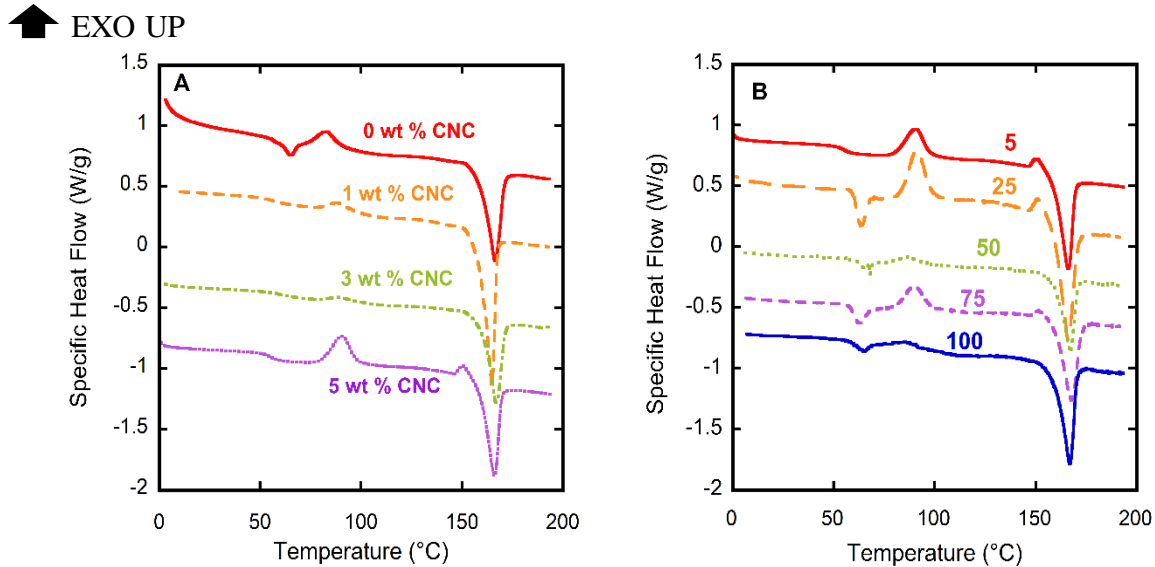


Figure 2.3 DSC thermograms for nanocomposite fibers for A) different CNC concentrations and B) different screw speeds. Exothermic is up in all DSC thermograms.

cellulose nanocrystals in the PLA/CNC fiber<sup>[43]</sup>. The cold crystallization temperature,  $T_{cc}$ , was also taken as the temperature of the maximum specific heat capacity.

Equation 2.1

$$\chi = \frac{\Delta H_m + \Delta H_c}{\Delta H_m^\circ (1 - x_{cnc})} \bullet 100\%$$

Figure 2.4 A summarizes the effects of CNC content and extrusion speed on as-spun polylactic acid fibers. CNC has been shown to act as a nucleating agent for polylactic acid which has a very slow rate of crystallization<sup>[29,31,33]</sup>. Of the fibers tested, the 1 wt% exhibited the highest  $\chi$ . However, further addition of CNC reduced  $\chi$  as CNCs can inhibit crystallization by acting as a barrier to polymer re-organization CNCs may act as a physical barrier or inhibit re-organization when weak secondary interactions between the ester group oxygen of PLA and the hydroxyl groups of the CNCs occur<sup>[34]</sup>. Weak hydrogen bonding has been thought to inhibit other molecular processes in polymers. This observation appeared true for all screw speeds examined and data

reached approximately similar degrees of crystallinity. Crystallinity in PLA is facilitated by strain-induced alignment in processes like fiber spinning and film orientation; so, by increasing the amount of spin drawing on the fiber, it was expected that  $\chi$  would change. However, this did not occur. It is possible that for the screw speeds examined, the difference in speed did not produce alignment differences large enough to overcome the slow crystallization rate of PLA and therefore samples achieved approximately the same amount of crystallinity. The variability in fiber thermograms may also be attributed in part to the complex mechanism of solidification during dry spinning in which evaporation and heat transfer occur simultaneously. Fibers were not drawn and wound in a controlled atmosphere chamber, but rather the winding process took place under a ventilated hood in an open lab which may have produced variations in evaporation rate. Regardless, of the lack of rate dependence, dry-spinning did produce a significant increase in  $\chi$  as compared to the cast PLA solution. This can be attributed to the preferential alignment of molecular chains and direct winding of the fibers from the orifice facilitating drawing of the fibers during processing. Both enhance crystallinity.

$T_{cc}$  decreased for the dry-spun fibers, as seen in Figure 2.4 B.  $T_{cc}$  is reduced from 133 °C for the 0 wt% solution to the 84-97°C for the as-spun fibers with a minimum value of 84°C for the 0 wt% fibers. As seen in  $\chi$ , where CNC content inhibited crystallization at CNC concentrations greater than 1 wt%,  $T_{cc}$  also began to increase as CNC content increased for the lowest screw

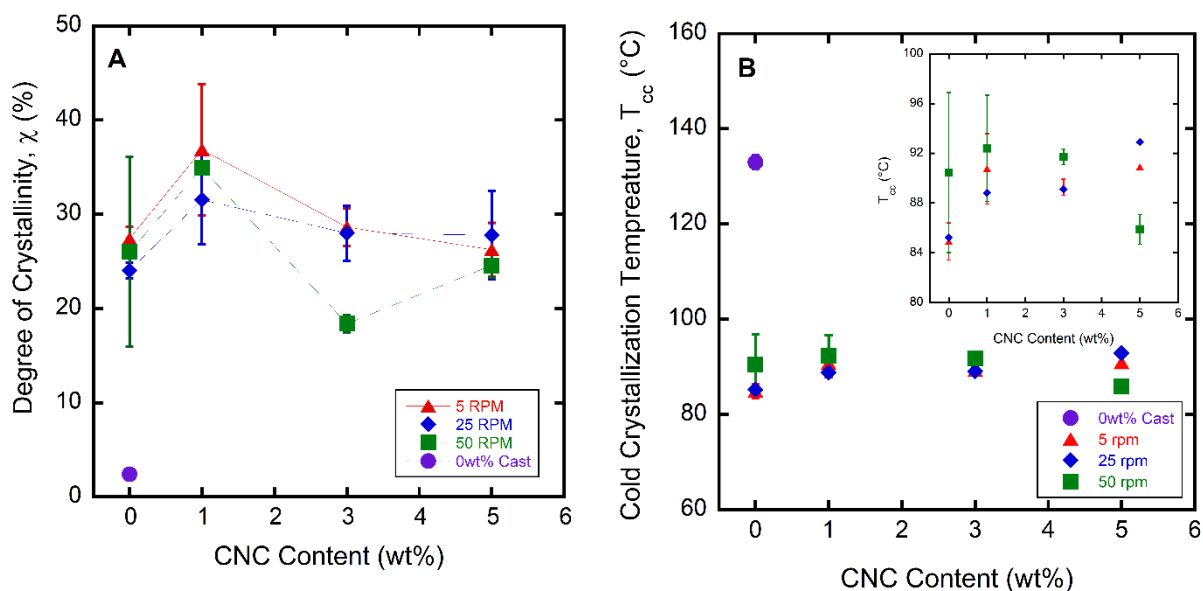


Figure 2.4 Summary of thermal properties from DSC thermograms: A) Degree of crystallinity,  $\chi$  and B)  $T_{cc}$  versus CNC content.

speeds (Figure 2.4 B inset). This suggests that even at 1 wt%, the CNCs behaved as a barrier to crystal growth because the temperature at which molecules had sufficient mobility to begin re-arranging was suppressed to higher temperatures despite a more conducive initial state from the spinning processing. For small screw speeds, fiber draw would be very large since the polymer is being extruded slowly but wound onto the barrel quickly. This should have produced more alignment of molecular chains and possibly the CNC along the tensile axis of the fiber, although the crystallization process during fiber spinning would be competing with higher rates of cooling and solvent evaporation. For the crystallinity and  $T_{cc}$ , this would imply a higher total crystallinity and a lower  $T_{cc}$  due to the preferential alignment. Of the as-spun fibers, the 50-rpm screw speed showed the most variability in  $T_{cc}$  with CNC content and the 5 and 25 rpm showed only small differences in  $T_{cc}$ . The weak dependence on screw speed may, again, be a symptom of variable atmosphere or it may be the efficient self-nucleation from solution was sufficient in all cases for fibers to achieve the same level of crystallinity, and thus, the dependence on screw speed was weak.

### 2.3.3 Mechanical Performance and Micromechanical Modeling

A representative stress-strain diagram for each CNC content is shown in Figure 2.5 A. Fibers exhibited a mixture of ductile and brittle behavior. Only the 5rpm condition was used for tensile testing because 1) all solutions produced continuous fiber at this condition and 2) the fibers were less brittle than faster extrusion speeds and could be handled throughout sample preparation. The fibers were binned into sub-sets of 20-35  $\mu\text{m}$ , 40-55  $\mu\text{m}$ , and 60-75  $\mu\text{m}$  +/- 2.5  $\mu\text{m}$ .

Increased stiffness and strength were primary motivations for reinforcing PLA with CNC. Factors which affected mechanical performance were crystallinity, and CNC loading. Elastic moduli from 2-6.5 GPa were achieved for dry spun fibers, which is comparable to dry-spun PLA values seen elsewhere (Figure 2.5 B) <sup>[23]</sup>. Of the three fiber diameter sets, the 40-55  $\mu\text{m}$  shows the clearest trend with CNC content; it increased linearly with increasing CNC content and approximately doubles from 0 wt% to 5 wt%. The increase in elastic modulus is primarily due to increasing CNC content as fiber crystallinity decreased with increasing CNC content, as seen in Figure 2.4 A. Fibers failed in either a brittle or ductile manner, without a strong dependence on CNC content, and thus, the strength at failure data is scattered (see Figure 2.5 C). The addition of CNCs was expected to introduce some brittleness into fibers, especially at high concentrations since other studies have observed embrittlement due to the addition of CNCs <sup>[33,53]</sup>. For fibers

exhibiting ductile failure, the strength at failure is similar to the yield point. These values are comparable to the low end of tensile strength values seen in polylactic acid fibers dry-spun from chloroform [20]. Interestingly, the average strength at failure for a fiber diameter bin decreased with increasing fiber diameter size, i.e. the smallest diameters exhibited the highest strength at failure. This agrees with Griffith's failure criterion which states that the likelihood of a defect being present increases with increasing size, which in this case, is fiber diameter<sup>36</sup>.

Fibers may have failed due to defects that arise particularly from the dry-spinning process. Defects included porosity and processing defects which resulted in variation in fiber diameter and thus higher stress at a failure site, as well as surface defects, like those in Figure 2.2, that may have initiated premature failure. Dry-spinning of PLA with CNC was challenging as more hydrophobic solvents such as chloroform could not be easily employed and thus a higher temperature solvent was employed. Moreover, the residual solvent that was removed during post-processing could leave behind larger porosity. During processing, fibers were at a higher temperature and subjected to an external drawing force that would help polymers diffuse into vacancies as the solvent was removed and closed porosity. Post-spinning thermal treatment processes were carried out far below the processing temperature and under static conditions.

Continuous and short- fiber micro-mechanical models were fit to the elastic modulus data for the 40-55 $\mu$ m data to predict the composite elastic modulus, E. Iso-strain and iso-stress models were fit to the data, as seen in Figure 2.5 D. These models assume a parallel or series relationship of the elastic moduli of the fiber and matrix material respectively [33,55]. The Halpin-Tsai model, Equation 2.2, was also fit to data as previous studies have demonstrated good agreement with data [33]. The geometry factor, in this case, is the aspect ratio, L/D,  $V_f$  is the volume fraction of the fiber, and  $\eta$  is the ratio defined below. The subscripts 'f' and 'm' stand for fiber and matrix. The average aspect ratio was calculated from TEM images of the CNC to find L/D=11.2.

Equation 2.2

$$E = E_m \left( \frac{1+(2L/D)\eta V_f}{1-\eta V_f} \right) \text{ where } \eta = \frac{\frac{E_f}{E_m}-1}{\frac{E_f}{E_m}+1}$$

The data is between the iso-strain and Halpin-Tsai predictions. Error in the Halpin-Tsai predictions may result from too wide a distribution of L/D or aggregation of CNCs changing the effective L/D [7]. In a previous study, the Halpin-Tsai was empirically fit to obtain a lower L/D ratio, which in turn, was attributed to the agglomeration of the CNCs in the polymer matrix as

agglomeration would result in a lower effective L/D; aggregation was probable as differences in chemical compatibility between the CNC and the hydrophobic PLA may inhibit dispersion<sup>[56]</sup>. However, this is most likely not the case with the present data set as the data lies above the L/D=11.2 prediction which implies that L/D is under-estimated for the current data set. This suggests a higher effective L/D ratio than what is predicted by the arithmetic average L/D from TEM images. Secondly, the Halpin-Tsai assumes that short fiber reinforcements are aligned along the primary fiber axis and that there is good adhesion between the matrix and the reinforcement. Poor chemical compatibility between CNC/PLA may invalidate the assumption of perfect adhesion, though it is difficult to resolve from the data. Additionally, the Halpin-Tsai does not accommodate for nanoparticle alignment which may result in a gross error for anisotropic particles like CNCs where the transverse and axial properties can vary by as much as an order of magnitude<sup>[57]</sup>.

Crystallinity was not incorporated into any of the micromechanical models which may also explain why the models under-predict the elastic modulus at certain concentrations of CNC, particularly at 1 wt% CNC. Crystalline and amorphous regions display different densities and elastic properties. As crystallinity increases, the elastic modulus and strength of polymers tend to increase as well. If the crystallinity content was assumed to be constant, which is not the case here, the assumptions of the iso-strain, iso-stress, and Halpin-Tsai would be valid as all three models assume the elastic modulus of the control as  $E_m$ . However, this assumption is not valid for the present study as  $\chi$  increased for 1 wt% and decreased with increasing CNC content. However, some contribution from the increased crystallinity may account for the vertical shift up from the Halpin-Tsai predictions as CNC acts as a nucleation agent<sup>[31,58]</sup>.

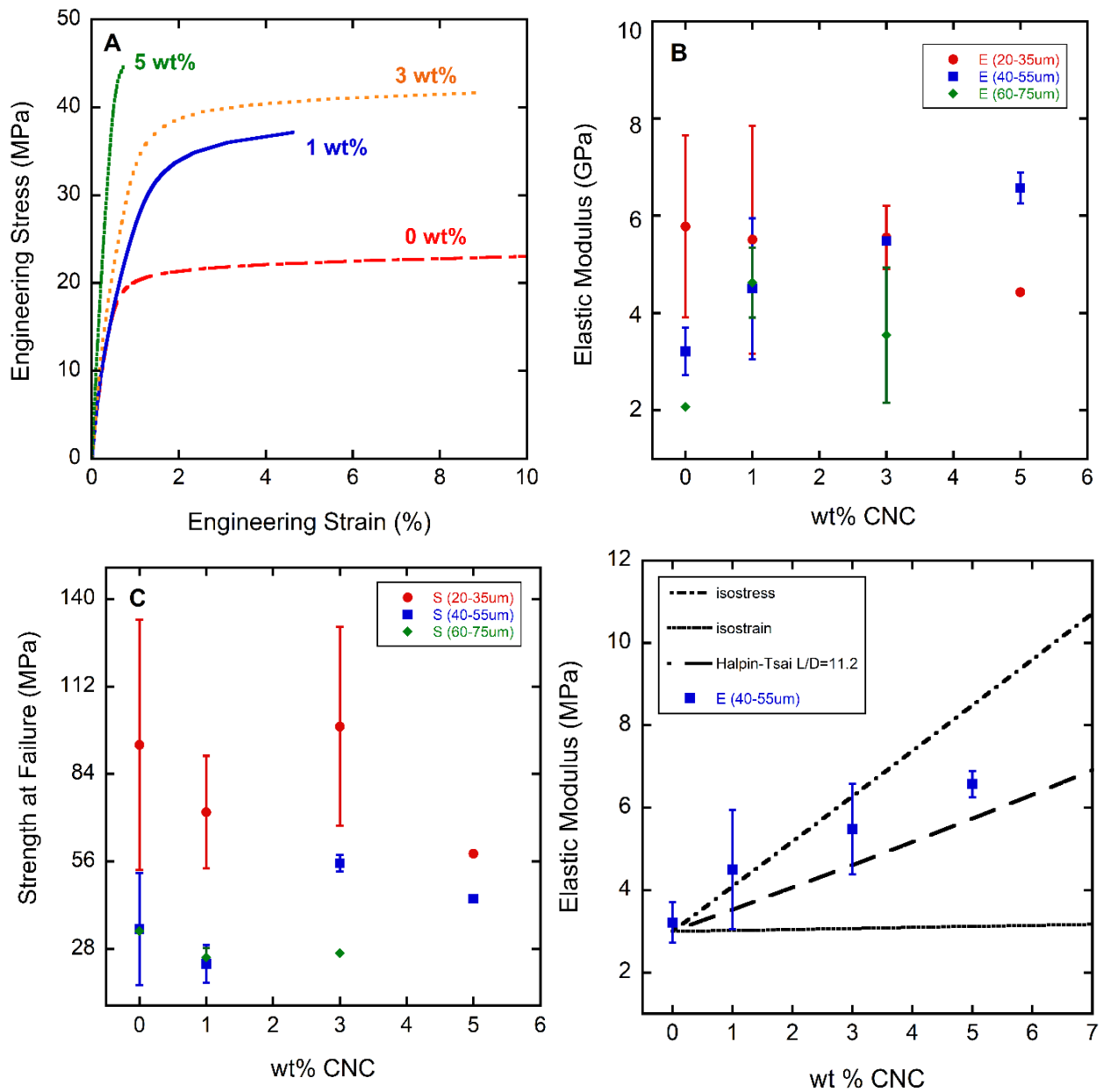


Figure 2.5 Mechanical properties of nanocomposites: A) Engineering stress-strain curves for select samples B) E versus CNC concentration and C) tensile strength versus concentration and D) Prediction of E for various micro-mechanical models.

## 2.4 Conclusions on Dry-Spinning of PLA Nanocomposite Fibers

Dry-spinning was investigated as a potential method for producing CNC/PLA fibers from dimethylformamide. While previous studies, such as Gogolewski *et al.* have successfully solution spun PLA using good solvents (for PLA) like dichloromethane and trichloromethane, these solvents were not chosen due to their toxicity [38]. Surface morphology differences were observed in fibers with and without CNC as a screw speed increased, assumed here to be proportional to extrusion speed. The onset of severe melt fracture occurred at high screw speeds and the addition of CNC did not help prevent melt fracture. The as-spun crystallinity of fibers was found to not depend heavily on processing conditions, however, small differences in the degree of crystallinity were observed that agree with previous observations on CNC in PLA. Dry-spinning produced fibers with moduli between 2-6.5 GPa and a maximum strength at failure 100 MPa. However, significant scatter in data is a shift from ductile to brittle-like behavior as CNC content increases and a result of pre-mature failure most likely due to processing defects from the spinning-process.

## 2.5 Acknowledgments for Dry Spinning

The authors would like to acknowledge financial support from the Private-Public Partnership for Nanotechnology in the Forestry Sector (P3Nano) under Grant No. 107528 and National Science Foundation Integrative Graduate Education and Research Traineeship: Sustainable Electronics Grant (Grant Number 1144843).

### 3. MELT SPINNING OF CELLULOSE NANOFIBRIL/POLY(LACTIC ACID) COMPOSITE FIBERS

This chapter contains work that was originally published in ACS Applied Polymer Materials under the title “Melt Spinning of Cellulose Nanofibril/Poly(Lactic Acid) (CNF/PLA) Composite Fibers for High Stiffness.” The original article has been modified in part to include information from the supplemental information of the published article. Moreover, this chapter contains experimental data collected by others. Data not collected by the author is: transmission electron microscopy images of nanoparticles, which were collected by Shoumya Nandy Shuvo and wide-angle x-ray diffraction data of fibers was collected by Sami M. El Awad Azrak. Conceptualization of how to measure/estimate orientation of fibers using optical microscopy was a collaborative effort with Reaz A. Chowdhury. Caitlyn Clarkson and Youngman Yoo made the chemically-modified CNF used in this chapter.<sup>[59]</sup> Otherwise, all lab work performed in this chapter was done by Caitlyn Clarkson. All writing was done by Caitlyn Clarkson. Dr. Youngblood, Dr. Schueneman, and Dr. Snyder advised on research directions and provided editing and guidance on all writing.

This chapter contains content reproduced with permission from C. M. Clarkson, S. M. El Awad Azrak, R. Chowdhury, S. N. Shuvo, J. Snyder, G. Schueneman, V. Ortalan, J. P. Youngblood, *ACS Appl. Polym. Mater.* **2019**, *1*, 166. Copyright 2019 ACS Applied Polymer Materials.

#### 3.1 Introduction

Fiber applications requiring high stiffness and strength, but low density may benefit from the development of nanocellulose/polymer composites because both components are low density (nanocellulose 1.5g/cc, polymers 1-1.5g/cc) and, as shown in previous literature, nanocellulose can increase stiffness and strength by over 100% <sup>[33,35,53,60]</sup>. High strength, high stiffness fiber could replace materials such as fiberglass but at a lower density and thus light-weighting components along with other environmental benefits as nanocellulose can be renewably sourced.

Cellulose nanocomposite fibers have been produced by solution-based spinning or melt spinning. Industrially, solution-based fiber spinning processes are primarily used where melt spinning processes are not otherwise possible. Polymers where the end properties justify the

increased cost, time, and chemical hazards, such as Kevlar™, are produced this way. Many researchers have investigated using solution-based spinning techniques to produce nanocellulose composite fibers. For instance, solution methods have been used to produce PVA/CNC fiber [35], PVA/CNC fiber mats [61], PVA/TEMPO-CNF fiber [37], cellulose acetate/CNC fiber [33], CNC/PLA fiber [62], CNC or CNF/alginate fiber mats [53], and CNC/PAN fiber [63,64]. These studies have demonstrated the significance of good matrix/reinforcement compatibility as well as orientation. Achieving orientation is crucial because highly oriented nanofibrils resulted in more effective stress transfer and subsequently better mechanical properties<sup>[35]</sup>. Melt spinning is a simpler and cheaper process than wet- or dry-spinning and is used industrially to produce materials like nylons and polyesters which are ubiquitous. Although melt processes have been used to produce bulk materials like CNC/PLA [21,65] and CNF/PLA [66], and CNC/PLA fibers [43,67,68] there are few examples of melt-spun fiber and of those, none are CNF composite fibers [69].

Melt-spun nanocellulose/polymer composite fibers have challenged researchers for several reasons including nanocellulose agglomeration and low thermal stability. Common approaches to address these challenges include direct liquid feeding of the nanocellulose/water solution into the polymer melt or working with the freeze-dried material; these methods have been performed with some success for bulk plastic and film [21,69]. However, agglomeration can still be present in either case [66,69]. Ideally, water should not be introduced as it plasticizes many polymers and can cause molecular weight degradation. Moreover, many polymers are processed above the thermal degradation temperature of nanocellulose. Processing over 250°C, and sometimes much lower depending on conditions, can cause yellowing or browning of the material and property loss due to oxidation [70–72].

Compatibilization also helps alleviate issues associated with agglomeration and thermal stability of nanocellulose. A wide variety of surface functionalization methods have been developed for attaching fatty acids, plasticizers, and small functional groups and ions (carboxylic acid, sulfate, phosphate) to make nanocellulose more compatible with hydrophobic media [28,73–76]. Surface modification can help shield or eliminate hydrogen bonding between neighboring particles or change the hydrophobicity of nanocellulose. Thermal stability also generally improves with modification. These methods are common for making nanocellulose/PLA composites as there is an inherent difference in hydrophilicity between the matrix and reinforcement [74,77–80]. In addition to changing the nanoparticle surface, polymer systems have been made more compatible with the

addition of plasticizers like polyethylene glycol (PEG) [81] or glycerol triacetate [21] to PLA. Although plasticizers are uncommon in fibers, they may impart additional benefits such as improving drawing or reducing embrittlement (commonly seen in nanocellulose composites).

PLA has generated interest because it is renewably sourced, industrially bio-compostable, and has environmental benefits like low CO<sub>2</sub> emissions during production. It has applications in 3D printing filament, bio-absorbable/bio-degradable materials for medicine, fibers, and nonwovens in domestic products, and food packaging. Nanocellulose/PLA composites primarily aim to improve the mechanical properties of PLA (which are generally inferior to other polyesters and nylon) or the crystallization rate. There is extensive evidence that nanocellulose can do both [21,43,62,67,78–80]. Additionally, PLA has a relatively low melting point (150-170°C) which allows for reduced processing temperatures.

The present study reports surface-modified CNF/PLA composite fibers by continuous melt spinning. To achieve this goal, CNF was chemically modified (mCNF) using a method developed previously by Yoo *et al.* [28] to improve nanoparticle/polymer interactions, which affect mechanical performance. Additionally, a compatibilizer was selected to carry the modified mCNFs into PLA. There are several reasons polyethylene glycol was chosen. Firstly, PEG is a miscible, known plasticizer for PLA. Secondly, mCNFs could be exchanged into PEG; this reduced potential molecular weight degradation by hydrolysis of PLA with water. Lastly, at low concentrations, low molecular weight PEG should not phase separate, but can increase the ductility of PLA [82,83]. Since mechanical performance also is strongly affected by nanoparticle alignment, fibers were hot-drawn post-fabrication. Mechanical properties were correlated to crystallinity and orientation with the use of differential scanning calorimetry (DSC) and wide-angle x-ray spectroscopy (WAXS).

## 3.2 Methods and Materials

### 3.2.1 Materials

Mechanically fibrillated CNF was acquired from the University of Maine, Orono, ME, USA (Lot # U22; 3% CNF-water slurry; 90% fines). Polyethylene glycol (PEG) was purchased from Sigma Aldrich, St. Louis, MO, USA (M<sub>n</sub> = 600g/mol). Nature Works INGEO-3001D polylactic acid was purchased from Jamplast, Ellisville, MO, USA. The CNF was chemically

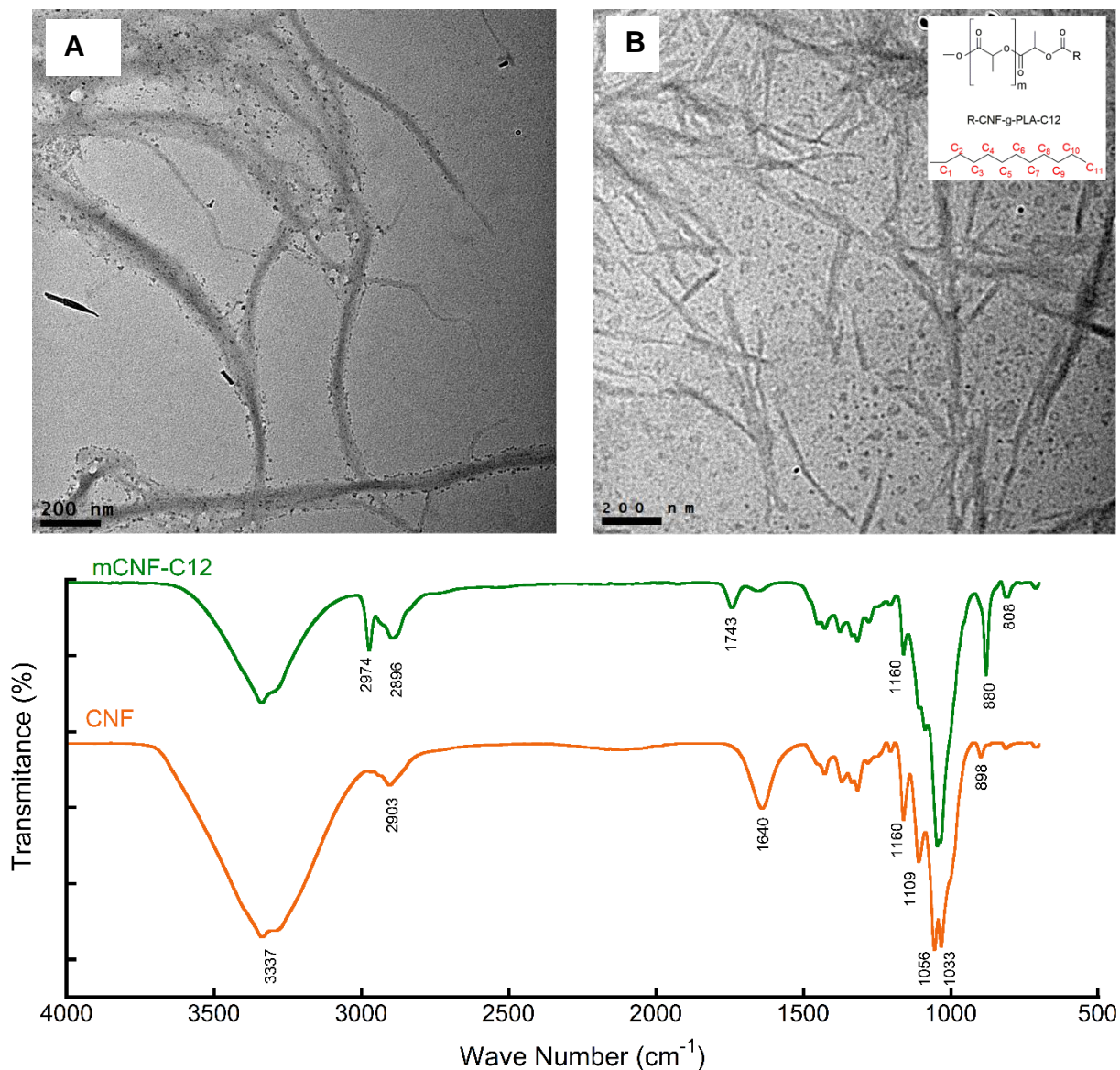


Figure 3.1 TEM images of A) unmodified, mechanically fibrillated CNF and B) after chemical modification. C) FTIR of the CNF before and after chemical modification.

modified through the hydroxyl group on the nanoparticle surface using methods outlined in Yoo *et al.*<sup>[28]</sup>. The process produced nanoparticles grafted with polylactic acid and capped with a twelve-carbon aliphatic chain as shown in the schematic in Figure 3.1 B (insert). Chemically modified CNF (mCNF) is referred to as mCNF-C12 henceforth. The modified product was approximately 8.5% mCNF-C12 in ethanol (EtOH) after modification; Fourier Transform Infrared spectroscopy (FTIR) data is shown in Figure 3.1 confirming the formation of the ester

Thermogravimetric analysis (TGA) confirmed that the onset of thermal degradation temperature was slightly improved after modification despite the reduction in particle size (Appendix B, Figure B. ). Chemical modification allowed higher CNF concentrations to be achieved in the PEG solutions as higher than 2 wt% of unmodified CNF in PEG could not be easily achieved. Nanoparticle morphology was characterized with transmission electron microscopy; a side-by-side comparison of before and after chemical modification is shown in Figure 3.1. To prepare final polyethylene glycol/mCNF-C12 solutions at 1, 5, 10, and 20 wt% mCNF-C12, an ethanol/water-based solution was made from solutions of PEG dissolved in water and mCNF-C12 in ethanol. A Branson Ultrasonifyer was employed to disperse mCNF-C12 into the ethanol at 30% amplitude with a 1-sec pulse and 1 sec off for a maximum of 30 seconds. The solutions were combined by first mechanically mixing and then ultra-sonification. To remove the solvent, a vacuum oven with liquid nitrogen cooled solvent trap was employed. The temperature of the vacuum oven was 70°C and 5-10 in-Hg. This process is visually represented in Figure 3.2 C.

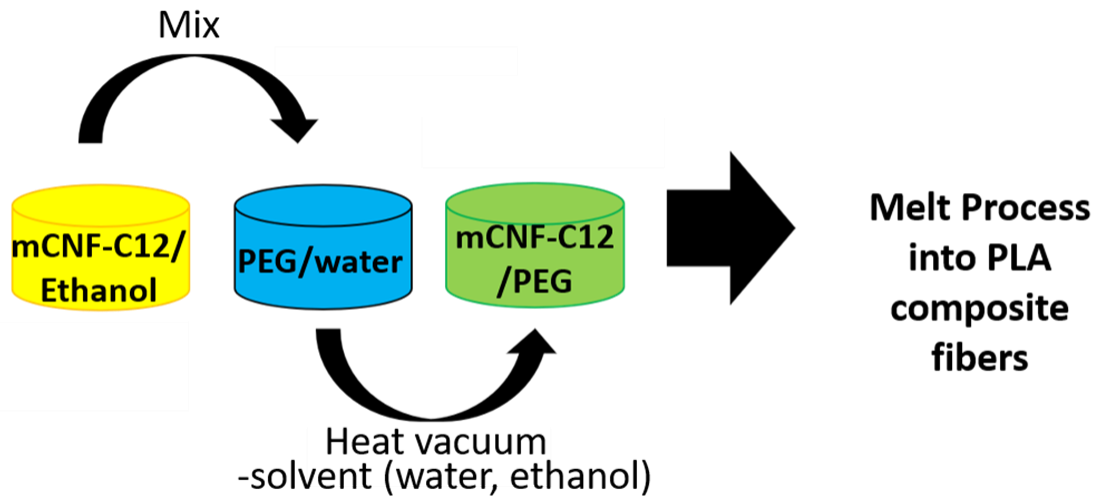


Figure 3.2 Process of exchanging CNFs into PEG.

### 3.2.2 Melt spinning and Post-Processing

A twin-screw Xplore 5 cc micro-compounder with a 90° turn and 1 mm orifice was used to produce melt-spun composite fibers at 200°C and 50 rpm rotary screw speed. Fibers were collected directly from the orifice on a Randcastle winding mandrel running at 150 rpm. PLA pellets were dried at 100°C overnight to remove absorbed water before compounding. The

PEG/mCNF -C12 solutions were measured to produce composite fibers at concentrations of 0.05, 0.3, 0.6, and 1.3 wt% mCNF-C12 from prepared solutions. Half of the material was first loaded through a continuous feed hopper, then the plasticizer was injected, and the remaining material was added again through the continuous feed hopper. The total compounding process was approximately 2.5 min, with 1.5 min of compounding the material after loading during which material can be recirculated through the compounder. Materials were compounded in sequential order with the transition material being disposed of between concentrations. The concentration of PEG was constant at 5 wt%. As a control, 0 wt% PEG 0 wt% mCNF-C12 fibers were also produced. Hot-drawing was performed over a 100°C heated parallel plate system by hand to draw ratios,  $L/L_0$ , up to six times the original length of the fiber, which was 25.4 mm initially. A change in birefringence was observed with hot drawing and representative images are shown in Figure 3.3.

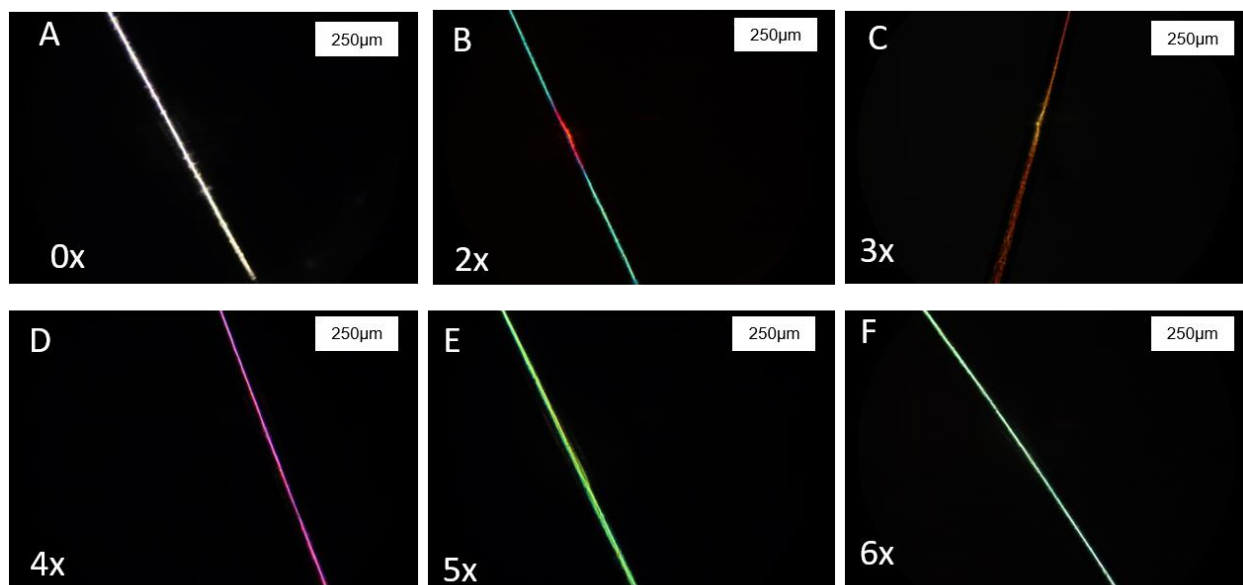


Figure 3.3 Birefringence in composite fibers for the composite 0.6 wt% mCNF-C12- 5 wt% PEG fiber is shown for draw ratios of A) 0X B) 2X C) 3X D) 4X E) 5X and F) 6X. Draw ratio was defined for this study as the change in length over original length.

### 3.2.3 Morphology and Dispersion

Fiber morphology was analyzed across multiple scales: optical microscopy and scanning electron microscopy (SEM). Optical microscopy images of as-spun fibers and hot-drawn fibers were taken on a Carl Zeiss (Axio observer A1) inverted light microscope equipped with a linearly

polarized light filter. Fiber morphology was imaged using an XL40 field emission scanning electron microscope. Sample surfaces were sputter-coated with a conductive gold-palladium barrier to help relieve charge built up on the polymer surface. Instrument parameters were 3-5 keV accelerating voltage and a working distance of 14-20 mm.

Transmission electron microscopy (TEM) images were taken before and after chemical modification of the mechanically fibrillated CNF as chemical modification can change nanoparticle morphology. A 0.5 wt% mCNF-C12 solution was prepared by mechanically mixing the appropriate amount of mCNF-C12 from ethanol with 10 ml of deionized, water with less than 10ppb total organic carbon (TOC) made in-house. The solution was then ultrasonicated using a Branson Ultrasonifyer for 30 seconds at 30 % power amplitude. Afterward, two drops of the sample mixture solution were drop cast on a 200-mesh copper grid with an amorphous carbon support membrane and were dried overnight in a sealed container to avoid any contamination before they were placed in the TEM holder the next day. BF-TEM images were taken at 300 kV on an FEI Titan ETEM 80-300 equipped with a Gatan Tridiem GIF without staining the sample with any staining agent. Several images at different regions of the samples, both in low and high magnification, were taken to fortify the data statistics.

### **3.2.4 Fiber Crystallinity and Orientation**

Thermal properties of as-spun and hot-drawn fibers were determined on a Thermal Analysis (TA) Q2000 differential scanning calorimeter (DSC). Heating experiments were performed at 10°C/min on hermetically sealed aluminum pans in a nitrogen atmosphere. DSC experiments are on multiple fibers that were bundled into a ‘hair-ball’ and then sealed in the pan. The sample mass was approximately 7 mg +/- 2.5 mg.

The order parameter,  $S$ , is a measure of the orientation. In nanocellulose and its composites,  $S$  has been primarily measured by wide-angle x-ray spectroscopy (WAXS) [3,33,35,84,85]. However, alternative methods, such as the determination of alignment from birefringence, also exist [86,87]. Optical methods can offer significant advantages over conventional x-ray spectroscopy in terms of cost and capability. Therefore, WAXS measurements are compared to measurements made using an optical microscopy-birefringence method. Methods for each measurement are subsequently provided.

For orientation experiments, samples were prepared by carding for ease of handling and transport. In brief, a 3 mm x 5 mm rectangular hole was cut from the center of thick cardstock. Three to five fibers were carefully glued parallel to each other and mounted in the WAXS such that the fiber axis was parallel to the source. The optical microscopy method used the same samples.

Estimation of the order parameter from optical microscopy images was performed using ImageJ and a Carl Zeiss (Axio observer A1) inverted light microscope equipped with a linearly polarized light filter. Two images were taken at 0° and 45° after finding the maximum intensity. Using ImageJ software, the mean pixel intensity and background intensity of the images were measured.  $S$  can be calculated from Equation 3.1<sup>[86]</sup>:

Equation 3.1

$$S = \frac{D-1}{D+2} \quad \text{where } D = I_{45}/I_0 \text{ and } I_{45 \text{ or } 0} = I_{Fiber} - I_{Background}$$

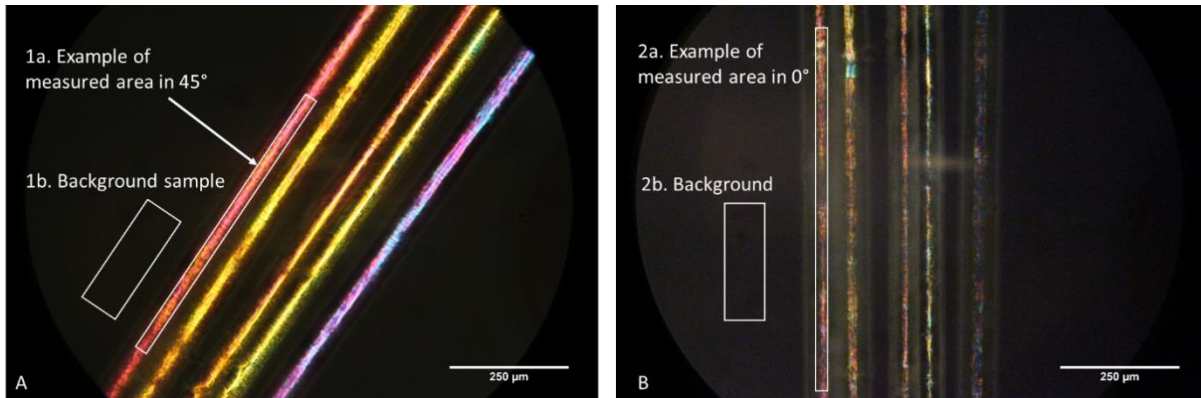


Figure 3.4 Optical micrographs of 0.05% mCNF-C12 under cross-polarized light at A) approximately 45° and B) 0°/90° to demonstrate the analysis of fiber micrographs for estimating the orientation.

Orientation in composite fibers was also measured by wide-angle x-ray diffraction (WAXS). The fibers were tested in transmission mode using a  $\text{CuK}\alpha$  beam with a wavelength ( $\lambda$ ) of 0.154 nm and a sample to detector distance of 79.248 mm. The equipment used was the SAXSpoint 2.0 (Anton Paar), equipped with a Dectris R1M photon counting hybrid pixel detector and a single crystal silicon scatter-less slits collimation tube. The detector was mounted on a tilted configuration to achieve wide-angle x-ray diffraction (up to  $2\theta = 60^\circ$ ). Due to equipment

limitations, half of the scattering pattern was available. Samples were mounted on cardboard for ease of handling and to facilitate easier alignment by mounting the fiber parallel to the short axis.

Fibers were irradiated for a total of 1000 seconds (4 intervals of 250 seconds each). Using the supplied software, the obtained 2D scattering patterns were converted to 1D scatter plots ( $I(\theta)$  vs.  $2\theta$ ) and background noise (cosmic radiation) was subtracted from all curves. Each curve was then normalized to the minimum intensity value to compare across all fiber scatter intensities. To obtain Herman's order parameter, ( $S$ ) the  $I(\phi)$  vs. azimuthal angle distribution was used. These distributions were generated by radial integration of the 2D scatter plots at a  $2\theta$  of  $16 \pm 0.1^\circ$  which represented the PLA (200) plane/peak. Thus, the order parameter can be calculated as follows in Equation 3.2 and Equation 3.3<sup>[88,89]</sup>:

Equation 3.2

$$S = \frac{1}{2}(3 \langle \cos^2 \phi_{200,Z} \rangle - 1)$$

Equation 3.3

$$\langle \cos^2 \phi_{200,Z} \rangle = \frac{\sum_0^{180^\circ} I(\phi) \sin(\phi) \cos^2 \phi}{\sum_0^{180^\circ} I(\phi) \sin(\phi)}$$

As described by Alexander and developed by P.H. Herman and his coworkers, because the fibers have been drawn to some degree and some of the crystal domains align with the fiber axis, this method can be used as a direct measure of crystallinity order with respect to the fiber axis<sup>[88,89]</sup>. In this case, total alignment represents a value of  $S = 1$  and completely random orientation has a value of  $S = 0$ <sup>[33]</sup>. Similarly, other researchers have used this technique to find the order parameter of alginate nanocomposite fibers<sup>[84]</sup>.

### 3.2.5 Tensile Properties

The mechanical performance of as-spun and drawn fibers were quantified using a TA Instruments Q800 Dynamic Mechanical Analyzer (DMA). Stress/strain experiments were performed using a force ramp at 0.3 N/min and 0.001 N pre-load; the temperature was 23°C and 30% relative humidity. Sample preparation followed the procedure outlined in Clarkson et al.<sup>[62]</sup>. The actual gauge length and minimum diameter of the fiber were recorded for calculation of the engineering stress and engineering strain from optical microscopy images taken prior to testing the sample. The sample size was 2-4 samples per condition and error bars are one standard deviation.

### 3.3 Results and Discussion

#### 3.3.1 Nanoparticle and Surface Morphology

The modification process produced nanoparticles with a very different morphology than the unmodified mechanically fibrillated CNF (Figure 3.1). Notably, the mCNF-C12 is shorter and thinner (thickness=26.2 +/- 9.6, length= 384.5 +/- 109.7). In the unmodified CNF, entanglements appeared to be very long-range (>500nm) and particles exhibited fibrillated structure. The mCNF-C12 still exhibits evidence of entanglements, however, there are now individual, small mCNF-C12s. Theoretically, the surface modification process could have broken down the amorphous regions of the CNFs while the stronger, more crystalline regions would have been left behind.

Microscopic evidence of increased surface roughness with mCNF-C12 concentration is evident in Figure 3.5 A-B. Ideally, individual nanoparticles would be homogeneously dispersed in the matrix, however, mCNF-C12 networks, which are entangled and long, are nearly impossible to completely break up during compounding regardless of chemical modification of fibrils and high shear rates. Despite ultrasonication of the mCNF-C12 solutions before solvent exchange, there is evidence of pre-existing entanglements of mCNF-C12s in the TEM image, Figure 3.1 A, of mCNF-C12 in PEG which would have been carried over into the compounding process. Instead, these nanoparticles may be distributed throughout the matrix in a mix of pre-existing entanglements and individual mCNF-C12s. There is some evidence of larger microscopic agglomerations in Figure 3.5 E-F, however, the sub-micron bumps appear to be uniformly distributed throughout the fibers.

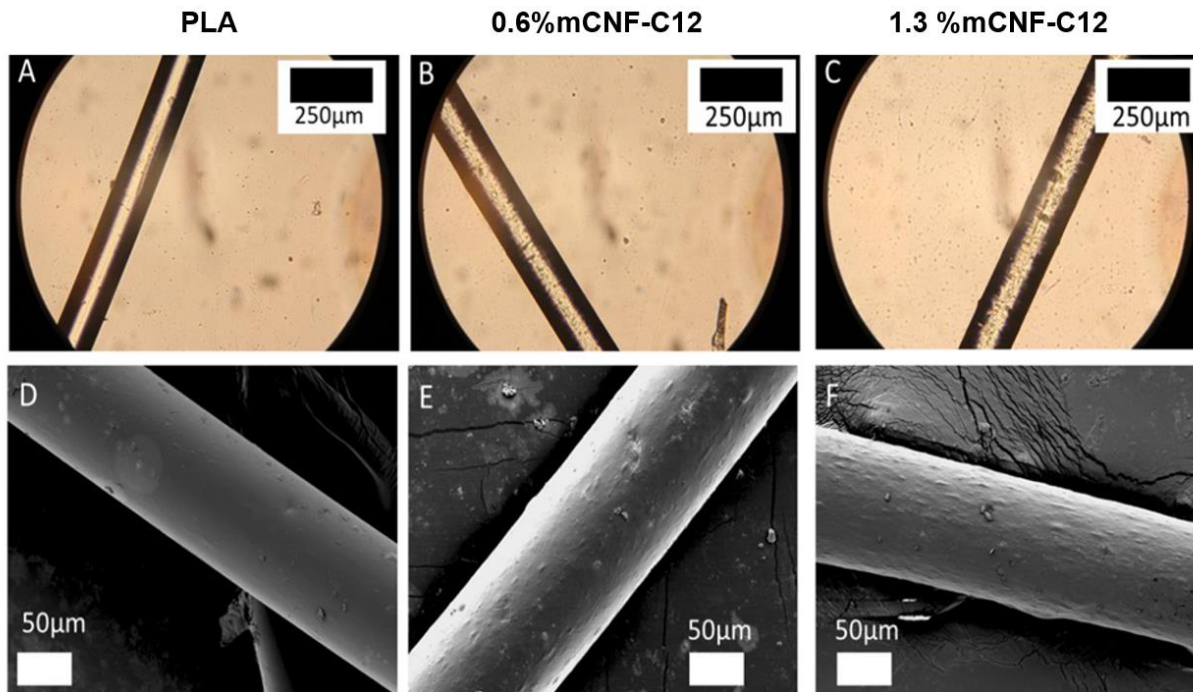


Figure 3.5 A-C) Optical micrographs at select concentrations of mCNF-C12. D-F) SEM images showing surface morphology with the addition of up to 1.3 wt% mCNF-C12.

### 3.3.2 Crystallinity

Crystallinity can be an essential component in obtaining good mechanical performance, however, PLA is a slow crystallizing polymer and does not usually obtain high degrees of crystallinity during rapid processing. Nevertheless, crystallization can be driven by the addition of various additives (such as nucleation agents) as well as through post-processing (hot-drawing) [35,43,77,78]. DSC was employed to measure the thermal properties of the composite fibers before and after hot-drawing and with increasing mCNF-C12 content (fixed PEG content). The thermal properties have been tabulated in Table 3.1 for DSC thermograms of three thermal histories. As many fibers had to be hand-drawn to produce a sufficient sample for DSC, the values represent an average of the material's thermal properties. The degree of crystallinity,  $\chi$ , was calculated with Equation 3.4 where  $\Delta H_m^0$ , the theoretical maximum melting enthalpy of PLA, is 93 J/g and  $x$  is the weight fractions of mCNF-C12 and PEG in the composite fibers [43,68,82,90,91]. The enthalpies of cold crystallization and experimental melting enthalpy are  $\Delta H_{cc}$  and  $\Delta H_m$ , respectively. Details for these measurements can be found in Appendix B, Figure B.

$$\chi\% = 100\%(\Delta H_m - \Delta H_{cc}) / (\Delta H_m^\circ (1 - X_{\text{CNF+PEG}}))$$

During reheating in the DSC, the material can undergo further crystallization and a cold crystallization peak can be observed. The DSC thermograms, Figure 3.6 A, show the cold crystallization peak over 85-100°C which is a consequence of the slow crystallization of PLA and is typically observed; also observed is an enthalpic peak immediately before the melting endotherm. This peak is most commonly associated with the formation of the less ordered  $\alpha'$  phase reordering at high temperatures. With the addition of mCNF-C12, these peaks are still present, however, the cold crystallization peak temperature ( $T_{cc}$ ), Table 3.1, is observed to shift to lower temperatures and the cold crystallization peaks generally appear sharper compared to neat PLA. Additionally, the glass transition temperature ( $T_g$ ) is suppressed to lower temperatures which can be indicative of a higher initial crystallinity. Although molecular confinement of amorphous regions by mCNF-C12 or the exclusion of PEG from the PLA crystal structure may also account for the decrease in  $T_g$  observed. By accounting for the cold crystallization during heating in the DSC, a relative value of the crystallinity,  $\chi$ , from the fiber processing history can be obtained from Equation 3.4.

Generally, the as-spun fibers all exhibited low degrees of crystallinity since, during processing, the fiber line experiences rapid cooling. However, at very small concentrations of (0.05 wt% and 0.3 wt% mCNF-C12)  $\chi$  was observed to increase from 3.8 % for neat PLA to a maximum of 10.2% crystallinity which suggests that at small concentrations the mCNF-g-PLA-C12 is a good heterogeneous nucleation agent (Table 3.1). Above 0.3%, the as-spun  $\chi$  values began to decrease, presumably because of mCNF-C12 percolation inhibiting molecular rearrangement which has been observed in other systems [35,62,92].

During hot-drawing, the material has a second chance to crystallize. The hot-drawing temperature was 100°C, which is just above the cold crystallization temperatures for all as-spun samples. For fibers hot-drawn to 3X the original fiber length,  $\chi$  increased compared to the as-spun conditions, but all fibers obtained  $\chi$  of ~20% or greater, with a maximum of 33.8% (PLA). Further hot-drawing did not produce a substantial increase in  $\chi$  as most values remained the same except for the 5% PEG and the 0.3% mCNF-C12 which were improved. Variation in these samples due to preparation might result in the difference observed in the 3X draw ratio and maximum draw ratio. Additionally, the hot-drawn fibers still exhibited cold crystallization upon heating in the DSC;

although the cold crystallization peaks largely decreased after hot-drawing compared to the as-spun material. Since the degree of crystallinity is similar across hot-drawn samples, this alone cannot account for mechanical performance. The other factors which will potentially affect performance are mCNF-C12 concentration as well as alignment.

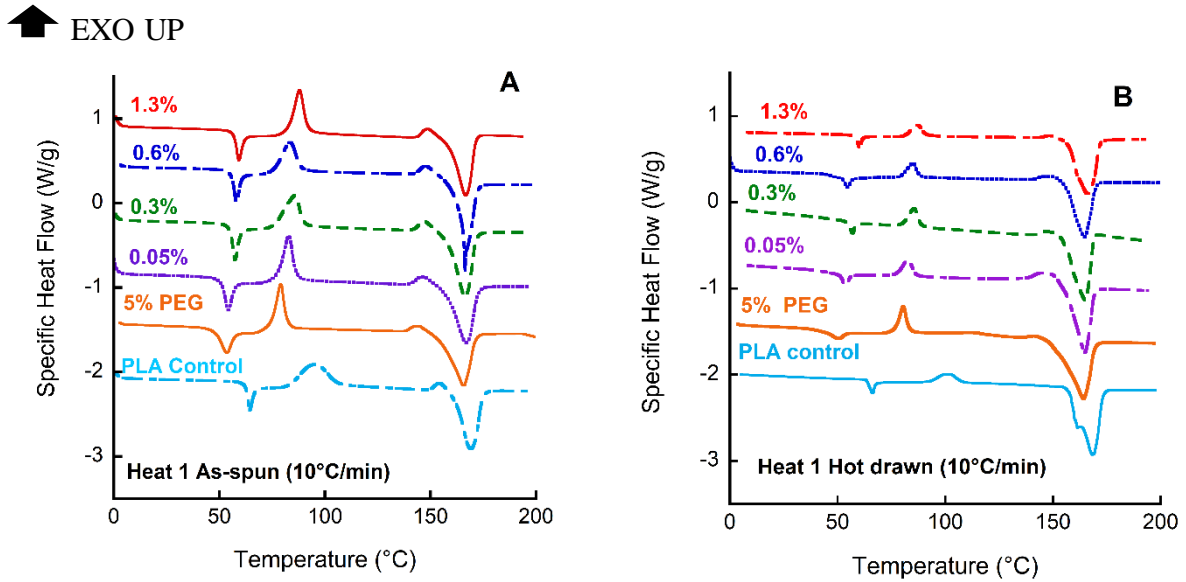


Figure 3.6 DSC thermograms of A) As-spun PLA composite fibers and B) composites fibers at the maximum hot-draw ratio (6X for all but PLA control, which was 4X). Exothermic is up in all thermograms.

Table 3.1 Thermal properties for three thermal histories.

As-spun			T <sub>g</sub>	T <sub>cc</sub>	T <sub>m</sub>	ΔH <sub>cc</sub>	ΔH <sub>m</sub>	X
DR	%PEG	%mCNF-C12	(°C)	(°C)	(°C)	(J/g)	(J/g)	(%)
0	0	0	63.1	95.1	169.0	31.1	34.6	3.8
0	5	0	50.0	79.1	165.6	28.9	35.7	7.8
0	5	0.05	52.3	82.9	166.9	27.0	35.7	9.8
0	5	0.3	56.5	85.8	166.5	28.6	37.5	10.2
0	5	0.6	56.8	83.4	166.4	23.8	32.1	9.4
0	5	1.3	58.4	88.0	166.7	26.4	31.7	6.1
Intended DR: 3X								
3	0	0	64.6	64.5	98.8	10.9	42.4	33.8
3	5	0	49.3	71.6	162.9	8.2	26.0	20.1
3	5	0.05	45.2	84.2	164.5	10.3	33.2	25.9
3	5	0.3	55.6	85.1	164.9	22.6	39.6	19.3
3	5	0.6	58.2	75.5	167.1	13.1	36.1	26.2
3	5	1.3	58.5	87.5	165.7	2.7	27.9	28.5
Maximum Draw								
4	0	0	63.1	102.2	168.4	10.7	44.8	36.6
6	5	0	47.9	80.6	164.1	8.8	43.6	39.4
6	5	0.05	52.7	82.8	164.7	6.6	30.7	27.3
6	5	0.3	56.1	85.7	164.9	7.2	37.2	34.0
6	5	0.6	53.6	85.0	164.6	5.6	30.6	28.5
6	5	1.3	58.3	86.6	165.9	6.4	36.7	34.7

### 3.3.3 Orientation

The orientation of the polymer and nanoparticles along the fiber axis is equally important in determining mechanical performance. As nanocellulose is highly anisotropic, maximizing the mechanical performance necessitated further alignment during hot-drawing and consequently, alignment of the polymer chains along the fiber axis has a similar effect. The orientation was measured using WAXS for three thermal histories (as-spun, 3X, and maximum draw) and the 1D information is shown in Figure 3.7 and the 2D information in Figure 3.8. WAXS diffraction patterns show an amorphous halo in the as-spun fibers and as fibers are hot-drawn, diffraction peaks appear due to increased crystallinity and alignment with hot-drawing. Herman's order parameter was calculated using Equation 3.2 and Equation 3.3 from the 2D diffraction patterns. Although PLA and CNF have (200) peaks at similar  $2\Theta$ , at such small concentrations of mCNF-C12, the WAXS patterns observed are effectively only for PLA. The 1D patterns, which were extracted from 2D plots, show only peaks corresponding to PLA and no evidence of nanocellulose (Figure 3.7).

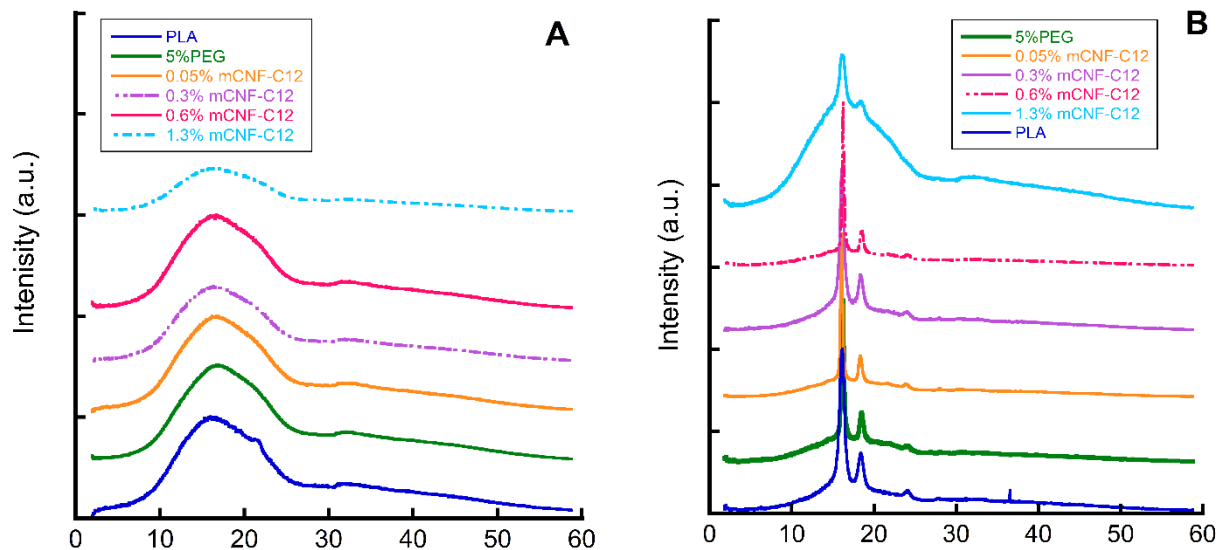


Figure 3.7 Intensity vs.  $2\Theta$  extracted from 2D WAXS results for A) as-drawn fibers and B) hot-drawn fibers. Shows evidence of amorphous and crystalline content in composite fibers and that the  $\alpha$ - phase is the predominate phase in composite fibers.

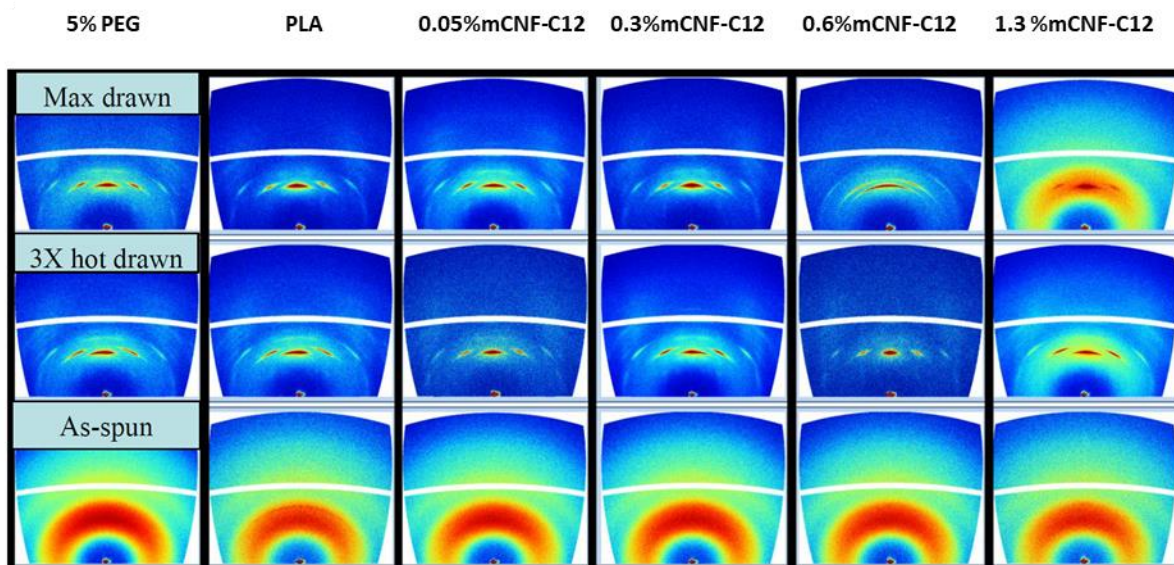


Figure 3.8 2D WAXS diffraction patterns for three thermal histories.

Herman's order parameter ( $S$ ) is plotted in Figure 3.9 A. Initially,  $S$  is less than 0.1 (unordered) since the as-spun fibers possess low crystallinity and low alignment. After hot-drawing,  $S$  increased to 0.65-0.75 (highly ordered) up to 0.6 wt% mCNF-C12 in the case of 3X and up to 0.3 wt% mCNF-C12 for the maximum hot-draw. Above 0.3 wt% mCNF-C12 the order parameter decreases with increasing mCNF-C12 concentration and with increasing draw ratio. This may be because of molecular confinement at higher mCNF-C12 concentrations. A potential explanation is shown in Figure 3.9 B. Initially, all fibers are comprised of mCNF-C12, amorphous and crystalline polymer, and free/unoccupied volume. The molecules are not highly ordered in this state. As the fiber is hot-drawn, the unoccupied volume is reduced, and the polymer can crystallize (resulting in additional densification). In the case of the low concentration, there are few mCNF-C12 to act as physical barriers and so the amorphous and crystalline polymer can be aligned along the fiber axis during drawing. However, at high concentration, the mCNF-C12 occupy a larger volume in the sample. Drawing of the fiber will bring nanoparticles closer together to the point where a percolation network is formed (if it did not already exist to some extent). Consequently, aggregation or molecular confinement may also impede crystallization (in addition to PLA alignment), this does not appear to be the case as observed in Table 3.1 (constant crystallinity) for the hot drawn fibers. Although  $S$  of PLA is decreasing, the nanoparticles may still be aligned along

the fiber axis, however, above a certain concentration, CNF alignment will also reach a maximum. Unfortunately, at a small concentration of CNF, WAXS cannot be used to determine the order of mCNF-C12 particles.

S was also calculated from optical microscopy (OM)-birefringence and S values are shown in Fig. 5A as well. A comparison of these two data sets is on a trend basis only as the procedures probe different levels of the fiber structure. WAXS measures the bulk properties of the fiber as data is collected from the entire sample from a crystalline material. The OM-birefringence can be used to study orientation locally or on average by selecting the area to measure intensity from the micrograph and crystalline and amorphous orientation will both contribute. For the S estimations in this study, the intensity was measured for a large area to be more comparable to the bulk properties measured by WAXS. There are some qualitative similarities to the WAXS data. Like the WAXS, S is high at low concentration for both the 3X and maximum draw ratios, however, S deviated at a different concentration compared to the WAX (0.3 wt% compared to 0.6 wt%). Additionally, S of the 3X did not decrease at 1.3wt% for the OM-data as it did for the WAXS measurements. Deviation in S between WAXS and OM-birefringence could be due to several sources such as small errors in alignment during imaging of the fibers in the 0° and 45° positions and measuring less than the maximum light intensity due to polarizer alignment.

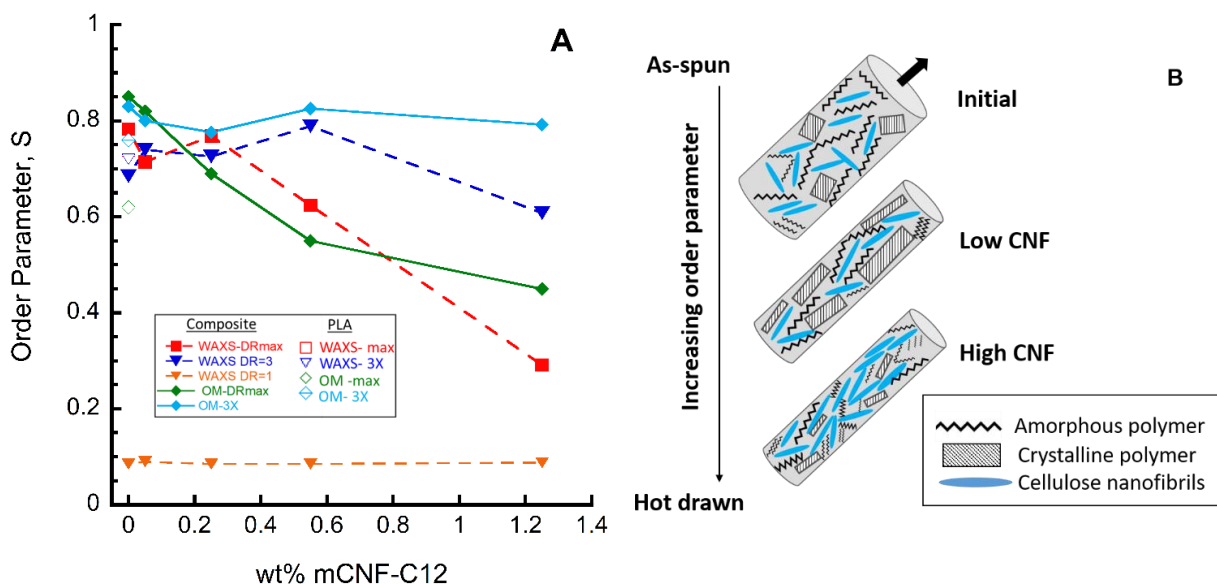


Figure 3.9 . A) Herman’s order parameter effect of hot-drawing and mCNF-C12 content at a constant PEG content of 5% (dotted lines are unmodified PLA) and B) visualization of the effect of hot-drawing on fibers with low mCNF-C12 and high mCNF-C12 content.

### 3.3.4 Mechanical Performance

Tensile tests were conducted on single fibers. The elastic modulus and strength at failure are reported in Figure 3.10A-B (Appendix B, Table B. 1). The addition of 5% PEG to PLA produced an initial decrease in elastic modulus and strength which is in good agreement with other studies that explored low molecular weight PEG as a plasticizer for PLA<sup>[82,83]</sup>. The elastic modulus was observed to depend strongly on mCNF-C12 content and processing history. In the as-spun fibers, the modulus was observed to increase with increasing mCNF-C12 content, however, the improvements were small until 1.3 wt% in which the elastic modulus went from 1.4 GPa to 4 GPa (up to 10.5 GPa with hot-drawing for 1.3 wt% mCNF-C12). The as-spun fibers exhibited low orientation (Figure 3.9 A) and low to moderate crystallinity (Table 3.1) which suggests that mCNF-C12 content alone is primarily responsible for the increase in stiffness. The strength at failure data of the as-spun fibers appears to remain constant, while at higher concentrations and draw-ratios the incidence of random failure during mechanical testing became more prevalent as a transition from more ductile-like behavior to brittle-like behavior was observed; this coincided with a transition in fracture type (Figure 3.11). Fibers may also have failed prematurely because

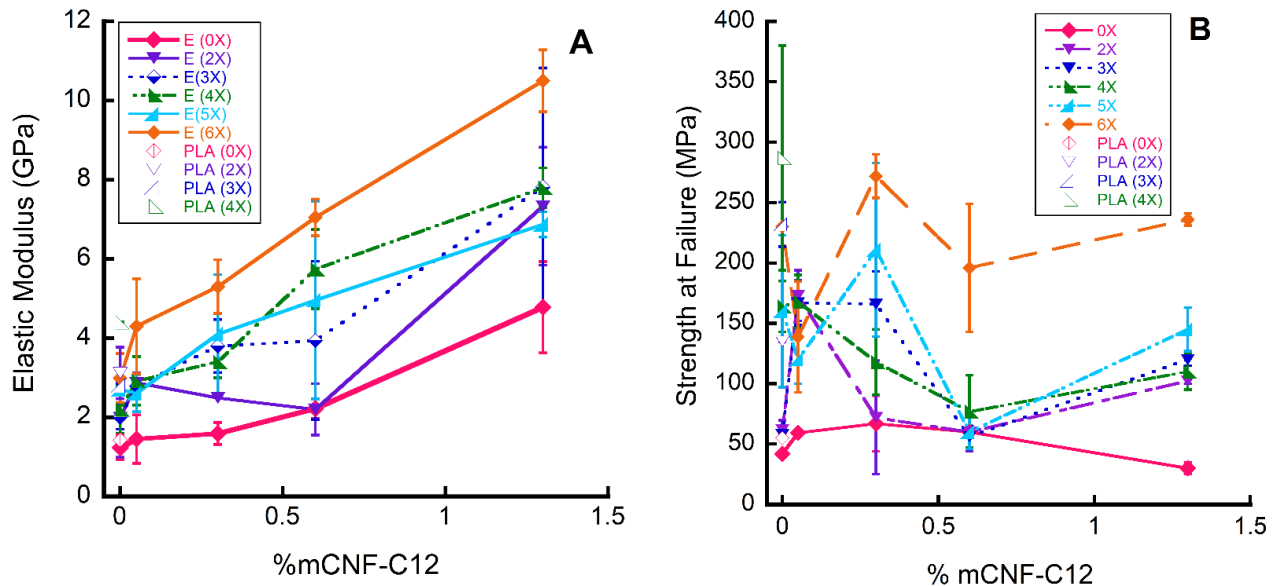


Figure 3.10 A) Elastic modulus vs mCNF-C12 content and B) strength-at-failure vs mCNF-C12 (filled shapes for up to 6X the original length). The 0 wt% mCNF-C12 refers to fibers with 5 wt% PEG and the PLA without any additives is shown as individual points (empty shapes).

of defects in the samples such as variation in fiber diameter or agglomerations/entanglements like those in Figure 3.3 which were not apparent in as-spun fibers until after drawing.

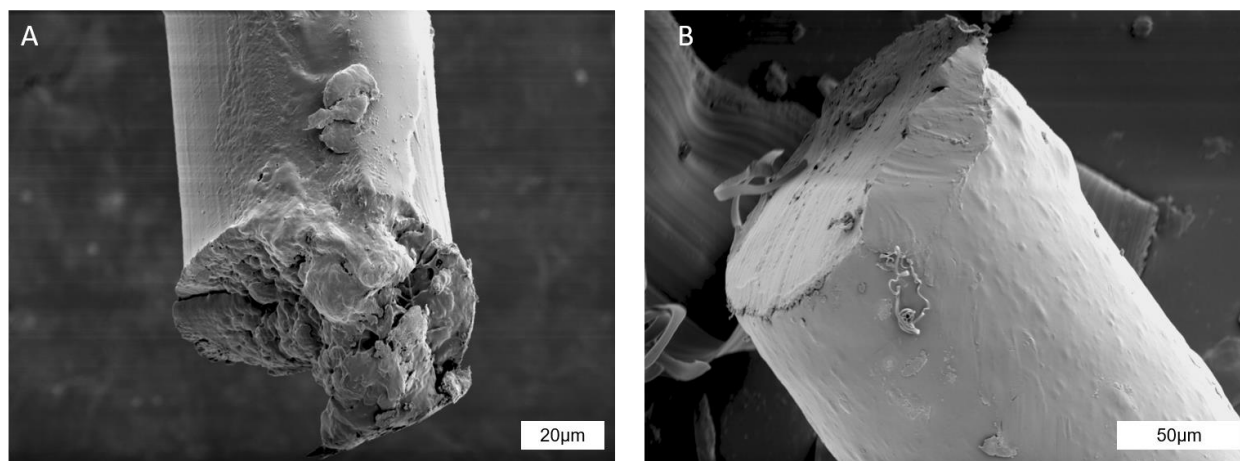


Figure 3.11 Fracture faces of A) PLA fibers and B) 1.3 wt% mCNF-C12 composite fibers. Failure changes from a more ductile-like to brittle-like behavior.

Several factors can affect the elastic modulus: crystallinity, alignment, and concentration. After hot-drawing, all fibers exhibited approximately the same degree of crystallinity, therefore orientation and concentration are suggested to be the primary factors affecting differences in the stiffness. Hot-drawing was performed to facilitate the alignment of both the polymer and mCNF-C12 along the fiber axis and was observed to improve the elastic modulus of both 0 wt% as well as composite fibers. From the as-spun state to the maximum hot-draw, stiffness improved over 200% for all conditions. Although  $S$  increased with hot-drawing, it did not exhibit the same monotonic dependence as the stiffness data. It increased substantially in neat PLA and at low concentrations of CNF and then at or above 0.6 wt% mCNF-C12 it exhibited increasing disorder both as CNF concentration increased and draw ratio increased. Despite achieving similar  $\chi$  and decreasing  $S$  parameter, the elastic modulus is highest for the maximum draw and at the highest concentrations of mCNF-C12, which suggests a strong dependence on concentration and implies that the mCNF-C12 are being preferably aligned along the fiber axis even though the polymer may be molecularly confined. Upon examination of Figure 3.10, from the as-spun 0 wt% to 1.3 wt%, the stiffness increase is primarily a function of increased concentration of the stiffer mCNF-C12 nanoparticles, however, with hot-drawing, the stiffness can be further increased, presumably by the alignment of stiffer axis of the mCNF-C12 particles along the fiber axis. Smaller draw ratios

exhibit similar qualitative behavior, although inconsistent processing of these fibers may have produced more variability in stiffness.

At the maximum DR, the strength at failure of the mCNF-C12 composites was approximately the value of the PLA. Although there are several confounding factors in the strength of failure data, an important factor is the reduction of the orientation parameter with increasing concentration of mCNF-C12 and draw ratio. At higher DR, the polymer components are trapped by the mCNF-C12 network and will not be aligned along the tensile axis and thus, the contribution to the strength from the PLA matrix may be less than the composite fibers with a lower concentration and at smaller DR. Moreover, the strength at failure of the composite will depend in part on the strength at failure of the individual components. Celluloses exhibit a strength at failure in the range of 200-1400 MPa [2]. The strength at failure of the mCNF-C12 used in the present study may be similar to those previously reported since nanocellulose is comprised of cellulose I and cellulose II. However, due to the brittle behavior exhibited by the neat PLA and composite fibers it is difficult to distinguish between the role of alignment, CNF concentration, and defect presence.

### **3.4 Conclusions on the Melt-Spinning of PLA Nanocomposite Fibers**

In the present study, a method to continuously melt spin mCNF-C12/PLA composite fibers without the introduction of water or solvent into the compounder was assessed. Composite fibers were produced by solvent exchanging modified CNF into PEG at various concentrations and melt blending into PLA. This method allowed very small concentrations of CNF (0.05 wt%) to be achieved and relatively high concentrations (1.3 wt%) as well. At high concentrations, there is some evidence that pre-existing entanglements or agglomerations of the mCNF-C12 were not removed during compounding, although dispersion appears good otherwise. Fibers were hot-drawn to facilitate alignment of the polymer matrix and mCNF-C12 which are highly anisotropic.

Despite the use of plasticizer as a processing aid and compatibilizer, the stiffness of the composite fibers was improved. The stiffness increased 280% for the as-spun fibers and 600% with hot-drawing. The strength at failure was scattered due to the embrittlement of the composite fibers with mCNF-C12 as well as agglomerations or entanglements acting as defects in the fiber. mCNF-C12 concentration appears to be the dominant factor in the improvement in stiffness as the

hot-drawn fibers achieved similar degrees of crystallinity and orientation (of the polymer) was observed to decrease at high mCNF-C12 concentrations.

### **3.5 Acknowledgments for Melt-Spinning**

The authors would like to acknowledge financial support from the Private-Public Partnership for Nanotechnology in the Forestry Sector (P3Nano) under Grant No. 107528, the Forest Products Laboratory Grant Number 17000384, and National Science Foundation Integrative Graduate Education and Research Traineeship: Sustainable Electronics Grant (Grant Number 1144843).

## 4. PRELIMINARY INVESTIGATION OF SMALL CONCENTRATIONS OF CNMS IN PLASTICIZED POLY(LACTIC ACID)

All lab work in this section was performed by Caitlyn Clarkson. All writing was performed by Caitlyn Clarkson with guidance and editing by Dr. Jeffrey Youngblood.

### 4.1 Introduction

Previously, many studies focused on achieving the maximum concentration of CNCs or CNFs in the nanocomposite to improve mechanical properties. For instance, Chen et al. created cellulose acetate/CNC composite fibers with up to 34 wt% CNC<sup>[33]</sup>, while Uddin *et al.* investigated PVOH/cellulose nanowhisker composite fibers with up to 30 wt%<sup>[35]</sup>. However, small concentrations of CNCs or CNFs have recently been shown to also be effective, especially when alignment can be facilitated. In the previous chapter, Chapter 3, it was shown the CNMs can be effective at improving properties even at relatively small concentrations (~1 wt% or less). By hot drawing to facilitate alignment along the fiber axis, the stiffness was further improved, but the fibers were brittle. Similar studies by Geng *et al.* have demonstrated the effectiveness of CNMs and alignment at small concentrations as well <sup>[27]</sup>. They explored solvent-cast plasticized PLA nanocomposites where 0.1 wt% of TEMPO-oxidized CNF were added and observed significant improvements in toughness and strength for nanocomposites <sup>[27]</sup>. Furthermore, CNMs have been shown to be potential nucleation agents. For instance, Gupta et al. explored the use of lignin-coated CNCs at 0.3 wt%, 1.0 wt%, and 2.0 wt% in PLA<sup>[31]</sup>. As little as 0.3% lignin-coated CNCs was needed to improve the crystallization rate and decrease the half time,  $\tau_{1/2}$  (time until 50% of the material has crystallized). For example, the control (neat PLA) had a  $\tau_{1/2}$  of 3.59 min at 95°C, while addition of 0.3 wt% lignin-CNCs decreased this value to 2.84 min<sup>[31]</sup>. These studies seem to be pointing to the usefulness of small concentrations of CNMs in some situations.

In Chapter 4, some preliminary work will be discussed on the development of plasticized PLA nanocomposites using small concentrations of unmodified and chemically modified CNCs and CNFs. The objective of this work was to investigate the effects of small concentrations of CNCs or CNFs on the properties of bulk plasticized PLA. While several plasticizers were

investigated, PEG was chosen as all CNMs could be exchanged into PEG and it is a known plasticizer for PLA<sup>[82]</sup>.

## 4.2 Materials and Methods

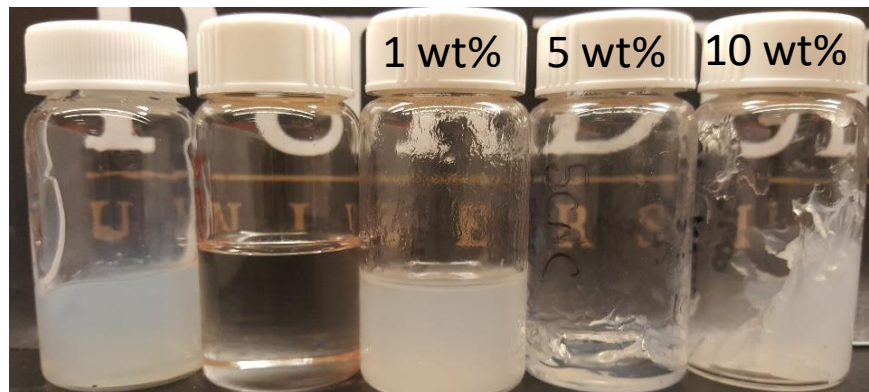
### 4.2.1 Materials

Nanocellulose crystals at 12 wt% aqueous slurry (2014-FPL-CNC-065; 11.9 wt% CNC-water slurry; 0.99 wt% sulfur on dry CNC) and micro-fibrillated nanocellulose fibrils at 3 wt% aqueous slurry (Lot # U22; 3 wt% CNF-water slurry; 90% fines) were acquired from the University of Maine, Orono, ME, USA. Chemical modification of nanocellulose crystals and nanocellulose fibrils was performed through the one-pot grafting process of Yoo *et al.*, whereby poly(lactic acid) is grafted through the surface hydroxyls on the nanoparticles. Nanoparticles were capped with a twelve-carbon chain, such as in Chapter 3 and will be referred to with a similar naming convention. The modified CNC as mCNC-C12 and the CNF are mCNF-C12. Modified nanocellulose solutions were produced in ethanol. Polyethylene glycol (PEG) was purchased from Sigma Aldrich, St. Louis, MO, USA (Mn= 600 g/mol). Nature Works Ingeo Polylactic Acid (PLA) 3001D was purchased from Jamplast Inc., Ellisville, MO, USA. Pellets were dried 24 hrs at 100°C before use.

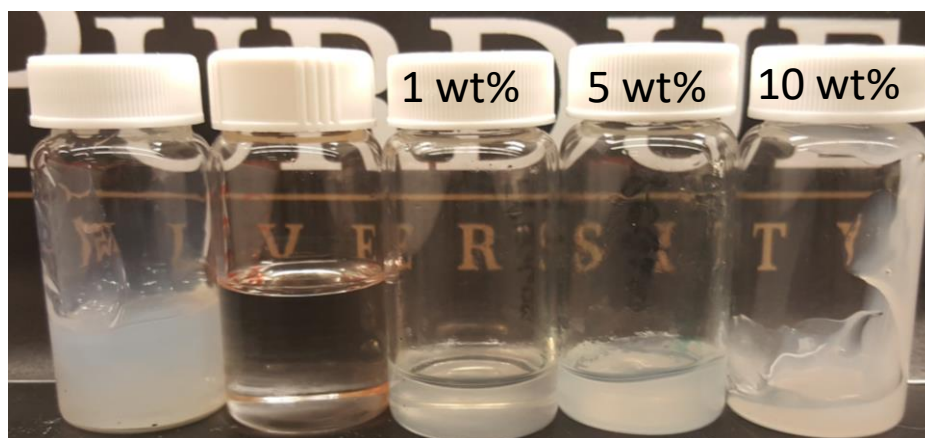
Stock solutions of nanocellulose/plasticizer were prepared at 1, 5, and 10 wt% nanocellulose content in PEG using the process introduced in Chapter 3, Figure 3.2. Unlike the mCNC-C12 and mCNF-C12, solutions prepared for CNC were in only water. Rotatory evaporation (70°C, 50 torr) followed by vacuum drying (70°C, 5 Torr) was employed to remove the residual solvent in either case. These solutions are shown in Figure 4.1

PLA/PEG/Nanocellulose materials were melt compounded on an Xplore 5cc twin-screw co-rotating compounder at 200°C following the compounding procedure detailed in Chapter 3, Melt spinning and Post-Processing. However, the fiber line was not equipped during this process, and the extrudate was collected on a steel plate instead. Samples were compression molded at 200°C for 5 min at 2 metric tons into various geometries. Two thermal histories were instilled in samples: a slow cool and a quenched history. Slowly cooled histories were cooled at approximately 10°C/min to room temperature under pressure. For quenched histories, the plaque was removed and quenched between two aluminum plates pre-cooled to 0°C.

### Pristine CNC/PEG600



### CNC-g-pla-C12/PEG600



### CNF-g-pla-C12/PEG600

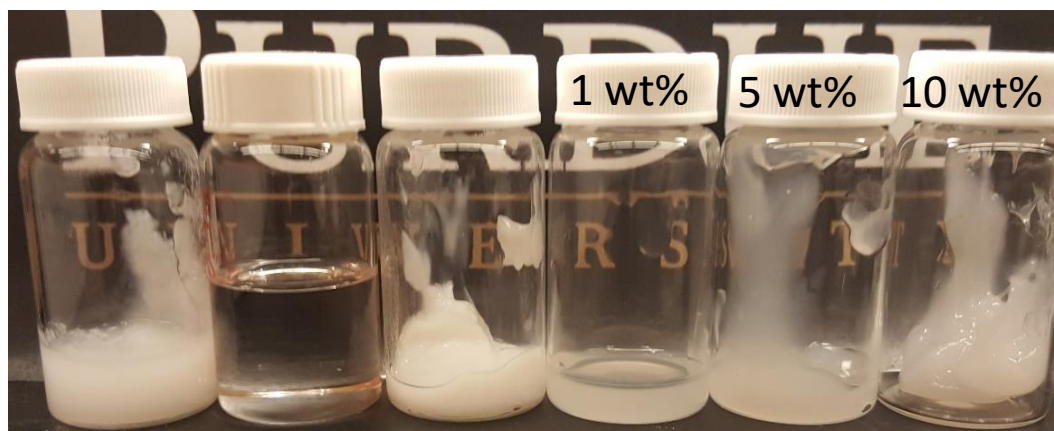


Figure 4.1 Images of various solutions used containing A) unmodified, pristine sulfuric acid CNCs B) CNC-g-pla-C12 and C) CNF-g-pla-C12. From left to right, CNMs in solvent (water or ethanol), 600g/mol PEG, and CNMs/PEG after water removal at three concentrations denoted on image.

#### **4.2.2 Fourier Infrared Spectroscopy (FTIR)**

A Fourier Infrared (FTIR) spectrophotometer was used to identify chemical information after chemical modification of the CNCs and CNFs was performed by Youngman Yoo, as well as confirm that the cleaning procedures were successful. FTIR was performed on modified CNC and CNF from ethanol and unmodified CNC and CNF from water for comparison. Ten scans were used and the wavelength range scanned was 500-1000 $\text{cm}^{-1}$ .

#### **4.2.3 Microscopy**

Optical microscopy images were made on a Carl Zeiss (Axio observer A1) inverted light microscope equipped with a linearly polarized light filter. Additionally, scanning electron microscopy (SEM) was used to image samples on an XL40 field emission scanning electron microscope. Sample surfaces were sputter-coated with a conductive gold-palladium barrier before imaging. Instrument parameters were 3-5 keV accelerating voltage and a working distance of 14-20 mm.

Transmission electron microscopy (TEM) images were collected on two occasions. The unmodified products were imaged at the time of purchase (Figure 4.2 A-B). Solutions were diluted to 0.5 wt% in water and sonicated using a Branson Ultrasonifyer (30% power amplitude, 1-sec on/1 sec off, 30 sec total). Samples were cast on copper wire grids from water and allowed to dry overnight then stained with a urea solution. The modified nanoparticles were imaged on a second system due to equipment availability (Figure 4.2 C-B). These samples were prepared after the mCNC-C12 and MCNF-C12 solutions were prepared by diluting the solutions to 0.5 wt% in water followed by ultrasonication on a Branson

Ultrasonifyer (30% power amplitude, 1 sec on/1 sec off, 30 sec total). Samples were drop-cast on a 200-mesh copper grid with an amorphous carbon support membrane and dried overnight in a sealed container. No additional staining was performed on these samples. A FEI Titan ETEM 80-300 equipped with a Gatan Tridiem was used to image specimens at 300 kV. Low and high magnification images were taken of the modified products.

#### 4.2.4 Characterization of Crystallinity

Thermal properties of composites were measured on a Thermal Analysis (TA) differential scanning calorimeter (DSC). A heat-cool-heat thermal cycle was performed on the compounded material at 10°C/min from 0 to 200°C. The results are from the second heat of the DSC experiment.

#### 4.2.5 Heat Deflection Temperature

Heat deflection temperatures were measured according to ASTM E2092-2 “Standard Test Method for Distortion Temperature in Three-Point Bending by Thermomechanical Analysis”. This standard was chosen over ASTM D648 “Deflection Temperature in Plastics Under Flexural Load in the Edgewise Position” due to equipment availability; the linear correlation coefficient between these two methods is 0.99. In brief, a bar is loaded into a three-point bend configuration on the TA Q800 DMA and constant stress, 0.455 MPa (1.82 MPa), is applied with the sample is heated at 2°C/min. The sample’s dimensions for these experiments were: 36 mm (span) x 12.5 mm x 3.15 mm. The force (F) needed to create stress ( $\sigma$ ) of 0.455 MPa was calculated using Equation 4.1. L is the length of the sample between contact points on the support (fixture span), b is the width, and d is the thickness. The deformation (D) is calculated from Equation 4.2. The  $\epsilon$  is 0.2%. The dimension change versus temperature is monitored and the temperature at which the sample dimension change equals D is the distortion or heat deflection temperature.

Equation 4.1

$$F = (2\sigma bd^2)/3L$$

Equation 4.2

$$D = (\epsilon L^2)(6d)$$

### 4.3 Results & Discussion

#### 4.3.1 Nanoparticle Characterization

One of the key concerns in PLA/nanocellulose composites is compatibility between the nanoparticle and polymer as it has a role in dispersion, thermal properties, and mechanical performance. In consideration, chemically modified CNCs and CNFs were investigated in addition to unmodified CNCs with PEG. Chemical grafting was performed on the sulfate half-ester form

of CNCs following the procedure of Yoo *et al.* who demonstrated that the one-pot method could successfully change the hydrophilicity of CNCs such that they would become dispersible in solvents such as toluene or chloroform, the latter of which PLA is highly soluble [28]. The one-pot method was also used to chemically modify mechanically fibrillated CNF. Although no previous work has been performed using this method with mechanically fibrillated CNF, Youngman Yoo ran his one-pot method to create the mCNF-C12 which was used in Chapter 3 and Chapter 4. Chemical modification was confirmed by FTIR (Figure 4.3). The appearance of a new peak at  $1740\text{ cm}^{-1}$ , adjacent to the absorbed water peak at  $1640\text{ cm}^{-1}$ , indicated the formation of the ester link in the modified group, while the absence of peaks occurring in lactic acid and lauric acid ( $1700\text{ cm}^{-1}$  and  $1730\text{ cm}^{-1}$ ) indicated that the washing steps were successful in removing residual reactants[28].

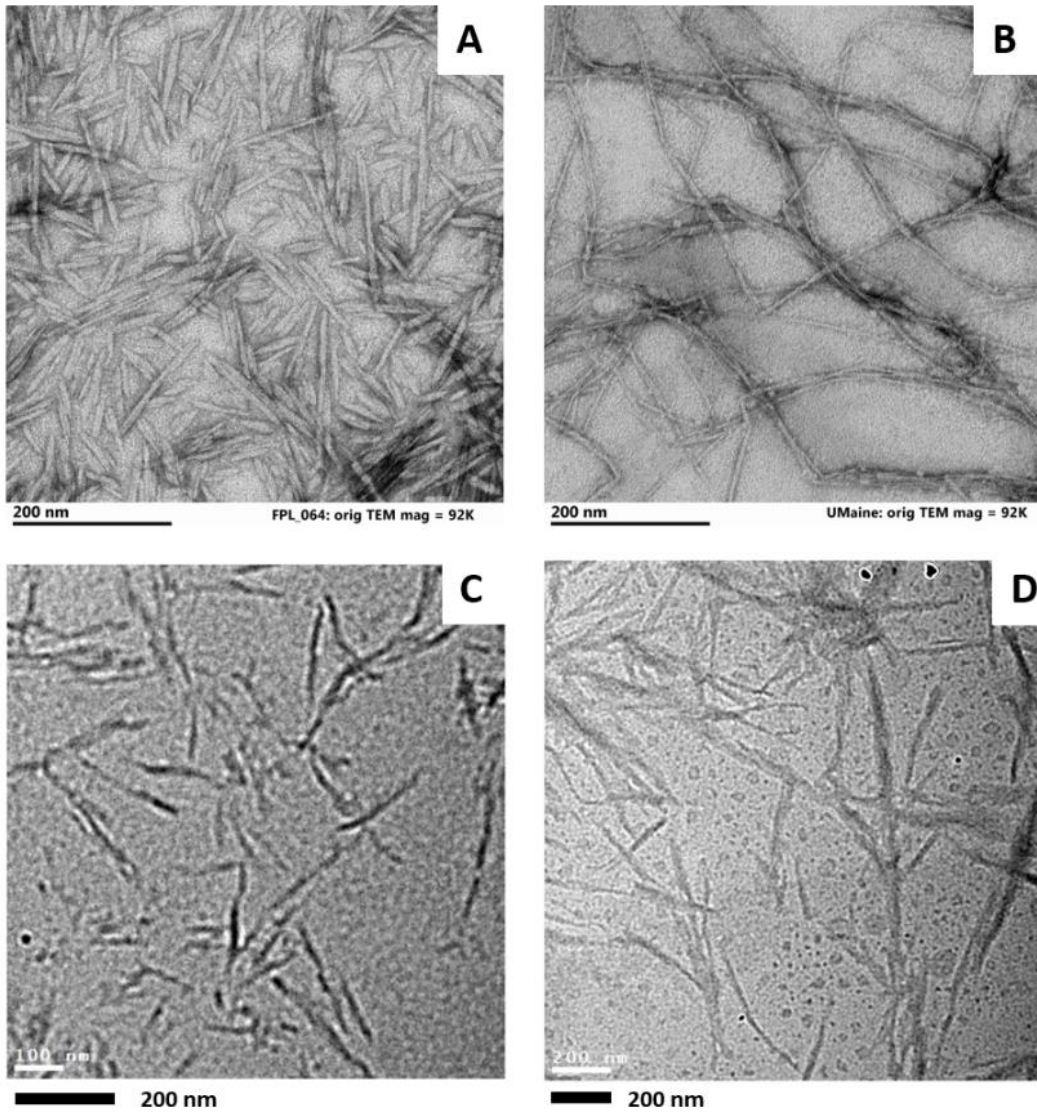


Figure 4.2 TEM images of A) CNC from water B) mechanically fibrillated CNF from water C) modified mCNC-C12 D) and mCNF-C12 from PEG solution.

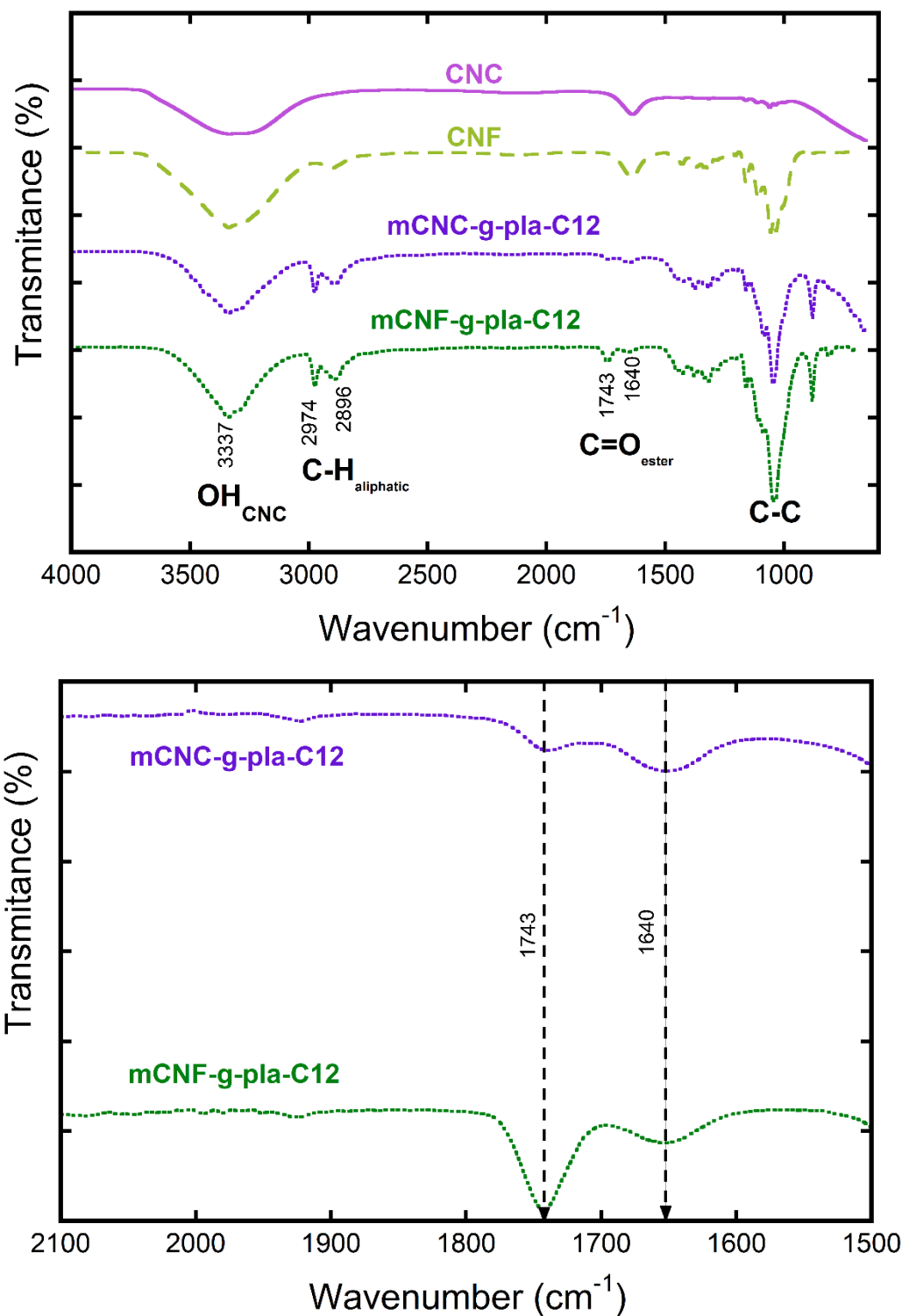


Figure 4.3 A) Summary of FTIR spectra of CNMs before and after chemical modification. B) FTIR spectra of chemically modified CNMs at a narrow wavenumber distribution showing evidence of primary peak confirming chemical modification.

Chemical modification can also produce morphological changes in the CNC or CNF. In Figure 4.2, TEM images of the unmodified products cast from water exhibited the characteristic rod-like appearance of CNCs (Figure 4.2 A) and the entangled network of mechanically fibrillated CNF (Figure 4.2 B). After modification, the mCNC-C12 morphology remained unchanged (Figure 4.2C) while the mechanically fibrillated CNF morphology and dimensions changed after modification (Figure 4.2 D). After modification, the mCNF-C12 exhibited a more rod-like structure compared to the unmodified particles which were long, bent and entangled, although some entanglements were preserved in the mCNF-C12. The mCNF-C12 exhibited a width and length reduction (Table 4.1); previously the length of individual mechanically fibrillated CNF could not be easily quantified as the particle lengths exceeded the dimension limit of the TEM and individual particles could not be identified for measurement within the highly entangled network. mCNF-C12 width was 26.2 +/- 9.6 nm (compared to 45.7 +/- 18 for unmodified CNF) and the lower limit of the length, estimated from individual nanoparticles, was 384.5 +/- 109.7 nm. CNCs are highly crystalline (54-88%) compared to mechanically fibrillated CNF [2] and it may be that less crystalline regions of the CNF were destroyed during the modification process while the CNC, which are more crystalline initially, were more resistant to heat and the acidic environment of the modification process.

Table 4.1 CNM particle dimensions.

<b>CNMs</b>	<b>Width (nm)</b>	<b>Length (nm)</b>	<b>Aspect ratio</b>
CNC	8.2+/-7	91.7 +/- 35.2	12.9+/-6.6
mCNC-C12	15.8 +/- 6.5	172.8+/-49.0	10.9 +/- 7.5
CNF	45.7 +/- 18	NA	NA
mCNF-C12	26.2+/-9.6	384.5+/-109.7	14.7 +/- 11.4

### 4.3.2 Appearance of Nanocomposites

Good distributive and dispersive mixing were obtained in nanocellulose composites. PEG served several purposes: nanocellulose was exchanged into PEG, which is water-soluble, to avoid introducing solvent which can cause degradation of molecular weight and PEG is a known plasticizer for PLA. Moreover, low molecular weight PEGs in the 200-1000g/mol range do not

show phase separation at low concentrations, <10%, in PLA and are effective in reducing some of the brittleness of PLA and reducing the glass transition temperature<sup>[82,83]</sup>. After compounding, samples were compression molded and subjected to two thermal histories (quench, slow cool); quenched histories were only used to study the dispersion of samples, while slowly cooled histories were used for additional tests. Quenched specimens exhibited high visual transparency with no visible signs of agglomeration on the micro-to-macro scale across all concentrations (Fig. 3). Due to refractive index matching, composites may exhibit high transparency despite poor dispersion, so cross-polarized light microscopy can be used to confirm that good dispersion was, in fact, achieved. The slow cool was sufficiently slow that PLA, a slow-crystallizing polymer, could crystallize during cooling and samples turned opaque white.

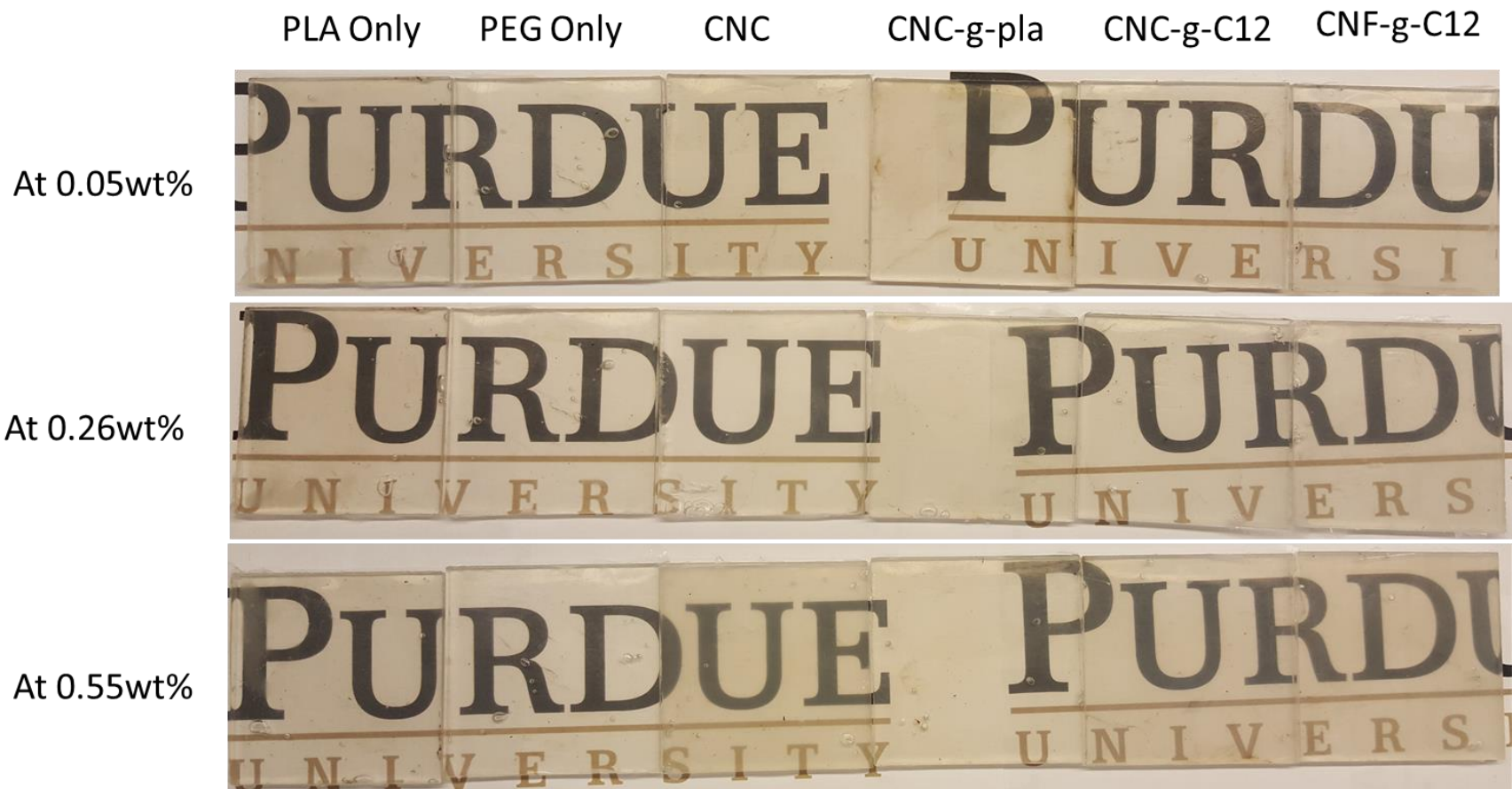


Figure 4.4 Images of nanocomposite plaques prepared with various CNMs at 0.05%, 0.26%, and 0.55% nanocelluloses with 5% PEG.

### 4.3.3 Crystallinity

PEG and nanocellulose were investigated as crystallinity enhancers. Separately, these materials have been shown to increase crystallinity by different mechanisms, i.e. plasticizers increase chain mobility and heterogeneous nucleation agents reduce the free surface energy requirement for nuclei to form. Together, PEG and nanocellulose interactions have been studied by various authors to overcome agglomeration in dried nanocellulose<sup>[93]</sup> and to facilitate dispersion in other processes<sup>[69]</sup>. It has been observed that PEG will screen neighboring CNCs and redispersion of CNCs dried with PEG exhibit good dispersion compared to pristine CNCs which form nearly inseparable agglomerations<sup>[94]</sup>. The favorable interaction of CNC/PEG and compatibility of PEG/PLA are additional compelling reasons for choosing PEG as a plasticizer during selection. With the introduction of both to the system, it was uncertain whether effectiveness would be maintained due to the favorable interactions between nanocellulose and PEG, or if the effect would be synergistic such as that seen in PEG and talc materials<sup>[49]</sup>. However, a combination of PEG/CNC and PEG/CNF has a synergistic effect on the crystallinity in PLA (Figure 4.5 A-D). In general, the crystallinity, calculated by Equation 4.3, was observed to increase compared to the neat PLA and 5% PEG controls. The integration methods for the melting and cold crystallization enthalpies followed the conventions set forth in Appendix C, Figure C. 1. Cold crystallization was reduced with the addition of 5% PEG and further reduced with the addition of nanocellulose (Table 4.2).

Equation 4.3

$$\chi (\%) = 100\% \frac{(\Delta H_m + \Delta H_{cc})}{(\Delta H_m^o (1 - x_{NC} - x_{PEG}))}$$

The effect of surface modification on crystallinity was explored. CNCs and CNFs were chemically modified with an aliphatic group to improve thermal stability within the processing window for PLA, change PLA/nanocellulose adhesion, and improve dispersion by eliminating spots for H-bonding between neighboring CNCs. The factors which affect adhesion and dispersion will also affect nucleation efficiency. In this case, the surface modification did not produce a large improvement in  $\chi$  between mCNC-C12 and CNC (Table 4.2). The  $\chi$  values and values of  $T_{cc}$ ,  $T_g$  and  $T_m$  were quite similar between concentrations of mCNC-C12 and CNC, which the exception of the 0.55% CNC which showed the highest  $\chi$  of the CNCs. Since surface modification effectively reduces the polarity of nanocellulose as hydroxyl groups are replaced with non-polar molecules it

was expected, based on a previous study, that the interfacial energy at high temperature would increase by chemically modifying the CNC with an aliphatic group<sup>[95]</sup>. Furthermore, the interaction of PEG with nanocellulose/PLA during crystallization is unknown. Previously, it was suggested that PEG compatibilized CNC with various polymers because of the adsorption of PEG to the CNC surface and hydrogen bonding in PEO/CNC and PEO/CNF composite films has been measured via infrared spectroscopy<sup>[60]</sup>. Strong hydrogen bonding may keep some of the available PEG adsorbed to the surface during melt compounding in which case surface modification would reduce this interaction as well.

▲ EXO UP

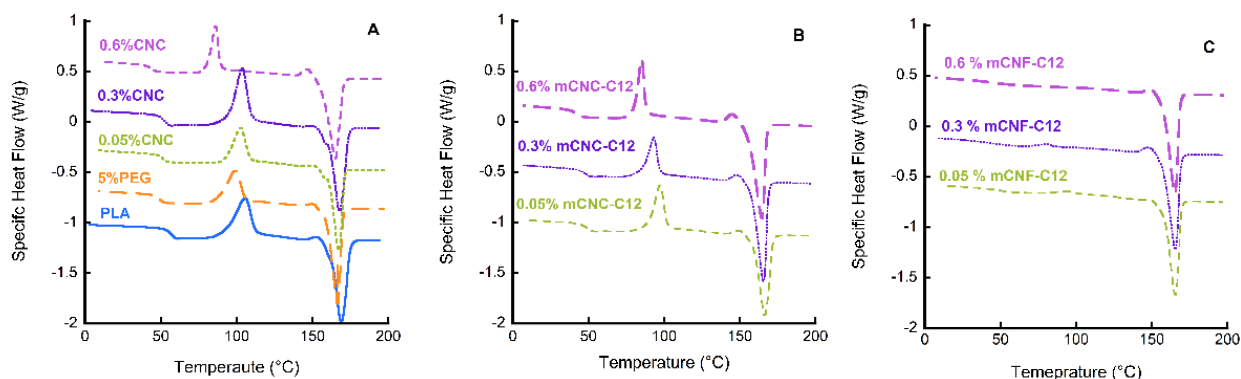


Figure 4.5 DSC thermograms of the second heat on A) CNC nanocomposites B) mCNC-C12 nanocomposites, and C) mCNF-C12 nanocomposites. Exothermic is up in all thermograms.

Particle size and shape effects were explored for the modified nanocellulose. Interestingly, the largest improvements in  $\chi$  were observed for mCNF-C12 (Table 4.2). Across concentrations, mCNF-C12 composites exhibited little to no detectable cold crystallization upon heating and obtained relatively high degrees of crystallinity after cooling at 10°C/min (Figure 4.5). Additionally, the  $T_g$  moved below detectable limits during a 10°C/min heating rate by differential scanning for the mCNF-C12 composites, which is further evidence that these materials are highly crystalline. Compared to CNCs, CNFs are long nanoparticles that are highly entangled. After chemical modification, Figure 4.2, the mCNF-C12 nanoparticles retained some of this character as they are both longer than either the CNCs and mCNC-C12s and entanglements still exist. These entanglements are thought to be the source of stiffness and strength improvements in CNF

composites. However, the expectation is that CNF networks would not improve crystallinity because they are highly entangled, and the entangled network would act as a barrier to kinetic processes like crystallization. Although at small concentrations this may not be the case. This unexpected effect on crystallinity may be due to enhanced dispersion of the CNFs with PEG as well as morphology changes due to chemical modification. If the mCNF-C12 were more functionalized as a result of the less crystalline material dissolving away during chemical modification, that may produce a much more attractive nucleation surface compared to the mCNC-C12 which underwent the same modification process.

Table 4.2 Summary of thermal properties for preliminary plasticized PLA nanocomposites.

Material	PEG (%)	CNC/CNF (%)	T <sub>g</sub> (°C)	T <sub>cc</sub> (°C)	T <sub>m</sub> (°C)	H <sub>cc</sub> (°C)	H <sub>m</sub> (°C)	χ (%)
PLA	0	0	57.65	107.50	168.40	28.90	37.75	9.52
5% PEG	5	0	49.10	99.01	166.52	20.51	42.69	23.85
CNC	5	0.05	43.31	84.37	163.56	16.30	38.99	22.67
CNC	5	0.25	47.45	85.92	165.17	15.97	40.61	24.70
CNC	5	0.55	46.36	91.37	164.48	12.50	42.53	30.19
CNC- C12	5	0.05	50.03	97.36	166.63	23.57	38.72	15.16
CNC- C12	5	0.25	48.57	93.25	165.69	20.10	41.07	21.02
CNC- C12	5	0.55	43.64	85.14	164.61	19.35	41.29	22.06
CNF- C12	5	0.05	49.91	95.17	165.59	2.93	42.87	42.97
CNF- C12	5	0.25	-	81.26	165.52	1.55	47.31	49.33
CNF -C12	5	0.55	-	-	165.22	-	44.27	47.87

#### 4.3.4 Heat Deflection Temperature of Nanocellulose/PLA Composites

Like poly(ethylene terephthalate) (PET) and polystyrene (PS), the heat deflection temperature (HDT) of PLA is close to its glass transition. However, unlike these polymers, the T<sub>g</sub> of PLA is usually 50-60°C which is impractical for many applications because it is so low (PET 70-80°C; PS 95-100°C). For instance, plastic products made of PLA cannot be easily sterilized in food applications as heating will often cause the product to deform. By increasing the crystallinity or mechanically reinforcing the polymer the heat deflection temperature can be improved. The present study examined a range of concentrations where nanocellulose was primarily a nucleation aid and not a mechanical reinforcement. Figure 4.6, showed that the heat deflection of all specimens for the slow cool history was improved with the addition of PEG and with nanocellulose

compared to neat PLA. The addition of 5% PEG alone produced a 20°C improvement in the HDT. The addition of any of the nanocellulose particles did not appear to produce a significant increase or decrease in the HDT. Although the DSC measurements predicted a difference in the crystallinity between nanoparticle types for a relatively quick cooling rate (10°C/min), the cooling rate in the compression molding process may be much slower, than the rate reported by the thermocouple which was located on the outside of the mold. By allowing the materials more time to crystallize during cooling in the molding process, materials could theoretically reach similar degrees of crystallinity but have reached them at different points in time.

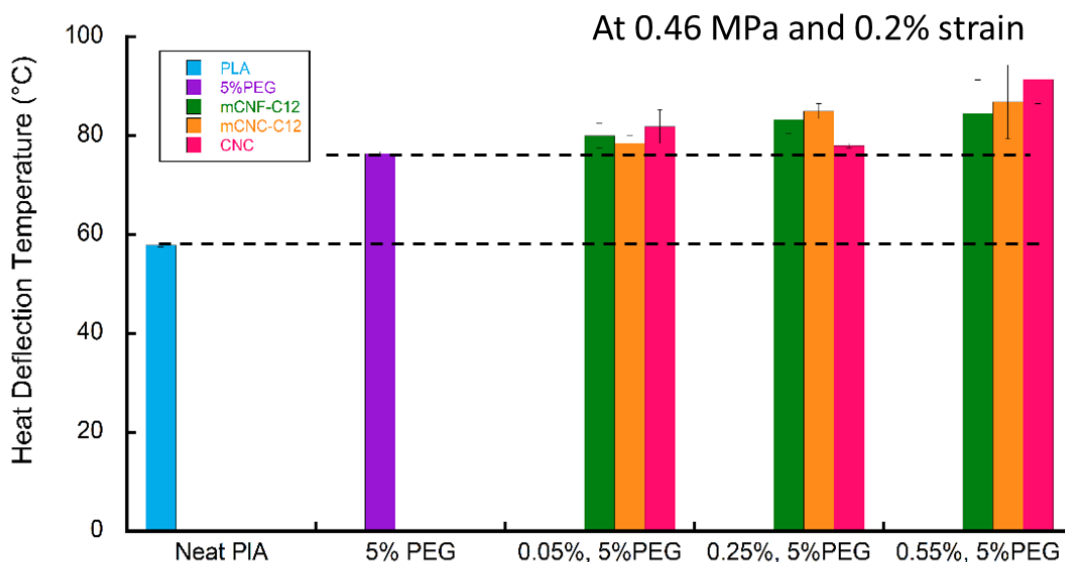


Figure 4.6 Heat deflection data for slow-cooled, compression molded samples.

#### 4.4 Conclusions on Bulk Properties of PLA Nanocomposites

Of the nanocomposites tested in the preliminary study, the mCNF-C12 showed the most promise as a heterogeneous nucleation agent based on the heating curves from the DSC, which showed higher degrees of crystallinity for these samples compared to either control or the samples containing CNCs. Moreover, there was no difference in HDT between samples, which suggests that any of the nanoparticles, for that thermal history, could be used to improve the HDT of PLA. However, due to the lack of availability of the chemically modified product, unmodified CNCs were chosen as the nanomaterial to proceed with future investigations since it was observed that small concentrations still improved the crystallinity and HDT.

## 5. SMALL CONCENTRATIONS OF CELLULOSE NANOFIBRILS AND CELLULOSE NANOCRYSTALS IN PLASTICIZED PLA: CRYSTALLIZATION KINETICS

All lab work in this chapter was performed by Caitlyn Clarkson. Sami M. El Awad Azrak wrote the MatLab codes used in this chapter and published in Appendix C. All writing was done by Caitlyn Clarkson with guidance and editing by Dr. Youngblood, Dr. Scheuneman, Dr. Snyder, and Sami M. El Awad Azrak.

This chapter contains work that was previously published by C. M. Clarkson, S. M. El Awad Azrak, G. T. Schueneman, J. F. Snyder, J. P. Youngblood, *Polymer*. **2020**, *187*, 122101. Copyright 2020 Polymer.

### 5.1 Introduction

Plasticization and heterogeneous nucleation of PLA have been investigated to increase total crystallinity and accelerate the crystallization rate of PLA, which is relatively slow <sup>[96]</sup>. Typical plasticizers for PLA and PLA blends include citrate esters, glycerol, polyethylene glycol (PEG), and polypropylene glycol <sup>[49,97,98]</sup>. Although plasticizers can impart many benefits, there is a trade-off with performance. For instance, plasticizers increase ductility and toughness but typically decrease stiffness and strength. Nucleation agents and fillers can mitigate losses. Nucleation agents and fillers, which reduce the surface energy requirement for stable nuclei formation, impact the crystallinity by increasing the number of crystallites. Talc is a common nucleation agent/filler in PLA when faster crystallization kinetics are desirable <sup>[49,78,96]</sup>. The combination of plasticizers and nucleation agents has a synergistic effect on the crystallization rate. For instance, the addition of talc to PLA can reduce the crystallization half-time significantly, but the addition of PEG and talc further reduces the half-time and extends the crystallization window to lower temperatures <sup>[49]</sup>.

Acquisition of more efficient and renewable nucleation agents has inspired exploration and development of various organic materials from nanocellulose, including pristine CNCs <sup>[99]</sup> and lignin-coated CNCs <sup>[31]</sup>. The efficacy of nanocellulose as a heterogeneous nucleation agent depends on specific surface area and dispersion in the polymer matrix. However, while nanocellulose has a high specific surface area to volume ratio which is good for nucleation, native CNC/CNF has poor compatibility with PLA and so disperses poorly leading to aggregation and

inefficient crystallization. Commonly, the organic solvent has been used to overcome this issue [21,62,99]. However, surface grafting has also been employed to improve the compatibility of nanocellulose with PLA through various modifications [6,100], utilizing grafted PLA chains [101,102], as well as grafting of known-plasticizers, like PEG, onto CNCs and CNFs [74,77]. However, using unmodified nanocellulose may offer significant cost savings if dispersion can be achieved. Some of the potential benefits of exploring organic nanoparticles as nucleation agents are speeding up crystallization kinetics or reducing crystallite size, as well as increased optical transparency, and tertiary effects like modifying the rheology of the polymer melt.

In many cases, the observed effects on crystallization are not intended as the CNC/CNF are used as reinforcements, and as such the concentration is high (above 1.0 wt%), while typical nucleant concentrations are much lower. Concentration is a critical parameter in promoting nucleation as above a critical concentration many heterogeneous nucleation aids, including nanocellulose, can inhibit molecular processes due to network formation. Gupta et al. demonstrated that lignin coated CNCs could be efficient nucleation aids at small concentrations (0.3%) but did not explore lower concentrations after observing that 0.1% of the lignin-coated CNC did not improve crystallization rates in PLA [31]. Moreover, CNC and CNF have been shown to affect the crystallization of PLA [18,20,24–26], but the majority explored high concentrations that bear little relevance to more typical nucleant concentrations.

The present work explores the combination of nanocellulose and plasticizer, specifically PEG, on the crystallization kinetics and morphology of PLA. To disperse nanocellulose in PLA, nanocellulose (CNC and CNF) were melt-compounded into PLA using a method reported by Clarkson et al. where CNC were first mixed with low molecular weight PEG through a process similar to conventional solvent exchange [6]. The solvent-free CNC/PEG and CNF/PEG solid solutions were melt-compounded into PLA to produce a fixed content of 5 wt% PEG and very small concentrations of CNC or CNF. Avrami analysis was performed on isothermal data spanning 90-130°C and melting peak data was collected for all thermal histories for a Hoffman-Weeks estimate of the equilibrium melting temperature. Lastly, secondary nucleation theory was applied to further quantify the nucleation efficiency and the morphology was analyzed by scanning electron microscopy for select isothermal histories.

## 5.2 Materials and Methods

### 5.2.1 Materials

Two types of nanocellulose were purchased from the University of Maine, Orono, ME, USA: Mechanically fibrillated CNF (Lot # U22; 3% CNF-water slurry; 90% fines) and sulfuric acid-derived CNCs (2014-FPL-CNC-065; 11.9 % CNC-water slurry; 0.99wt% sulfur on dry CNC)<sup>[2]</sup>. Transmission electron microscopy (TEM) images for these materials are provided in Chapter 1, Figure 1.1 or Chapter 4, Figure 4.1. CNC dimensions were 8.2 $\pm$ 7nm by 91.7 $\pm$ 35.2 and CNF were 45.7 $\pm$ 18nm wide and length dimensions exceeded the TEM view. Additionally, preliminary studies also examined chemically modified CNCs and CNFs from the one-pot process developed by Yoo *et al.* Modified nanocellulose solutions were produced in ethanol and will be referred to as mCNC-C12 and mCNF-C12.

Polyethylene glycol (PEG) was purchased from Millipore Sigma, St. Louis, MO, USA (Mn = 600g/mol) and Nature Works INGENEO-3001D polylactic acid was purchased from Jamplast, Ellisville, MO, USA. The comparison material, Arcos Organics talc (Lot A0381563; <75 $\mu$ m /-200mesh; MW= 379.26g/mol), was purchased from VWR International, Radnor, PA, USA. De-ionized, ultra-clean water was produced in house using a Barnstead device and was used for all solutions to avoid extra contamination. PLA pellets were vacuum dried at 70-100 $^{\circ}$ C for 3-4 hours before use.

### 5.2.2 Processing of Nanocomposites

As reported elsewhere, prior to compounding, solutions of CNC and CNF with PEG were prepared<sup>[6]</sup>. In brief, a solution of PEG in water was prepared by mechanically mixing. Meanwhile, CNC and CNF solutions were diluted with water and ultrasonicated using a Branson Ultrasonifyer at 30% power amplitude for 30 sec with a 1-sec pulse and 1-sec rest for a total energy of 1800 J/g CNC. The respective CNC and CNF solutions were then poured into the PEG/water solution and allowed to mechanically mix on low heat for several hours before being ultrasonicated similarly a second time. A rotary evaporator at 70 $^{\circ}$ C and 125 Torr was used to remove the bulk of the water from the nanocellulose/PEG solution. A higher vacuum (2 Torr) at 70 $^{\circ}$ C was used to remove the remaining water. The procedure was used to create 1 wt% and 10 wt% CNC in PEG and 1 wt% CNF in PEG solutions; initial dispersion of nanocellulose in PEG is shown in polarized optical

micrographs (Figure 5.1). The 1 wt% CNC solution showed the best dispersion with little to no micron-scale agglomerations while increasing to 10 wt% CNC some agglomerations are present in the material (Figure 5.1). The 1 wt% CNF shows evidence of agglomerations and entanglements which is expected since, as Figure 5.1 shows, CNF entanglements can persist despite best efforts to disperse the nanoparticles. Using this method, it was difficult to obtain higher concentrations of CNF in PEG for comparison to the CNC nanocomposites as the CNF starts at a much lower concentration in water compared to CNC and phase separation was a concern. Immediately after drying, the CNC/PEG and CNF/PEG solutions were injected with a syringe-style hopper into PLA (dried at 100°C for 12hrs) at fixed quantities to produce the following compositions with 5 wt% PEG: 0.05 wt% CNF, 0.05 wt% CNC, and 0.55 wt% CNC. Talc was premixed with PEG to produce a 1 wt% solution for compounding using mechanical mixing and ultrasonication in line with the method used to prepare the nanocellulose compositions. Compounding was performed in a twin-screw 5cc Xplore micro-compounder with continuous feed hopper at 200°C and 100 rpm for 5 min for all compositions. Cross-polarized optical microscopy of all samples showing dispersion is in Figure 5.2.

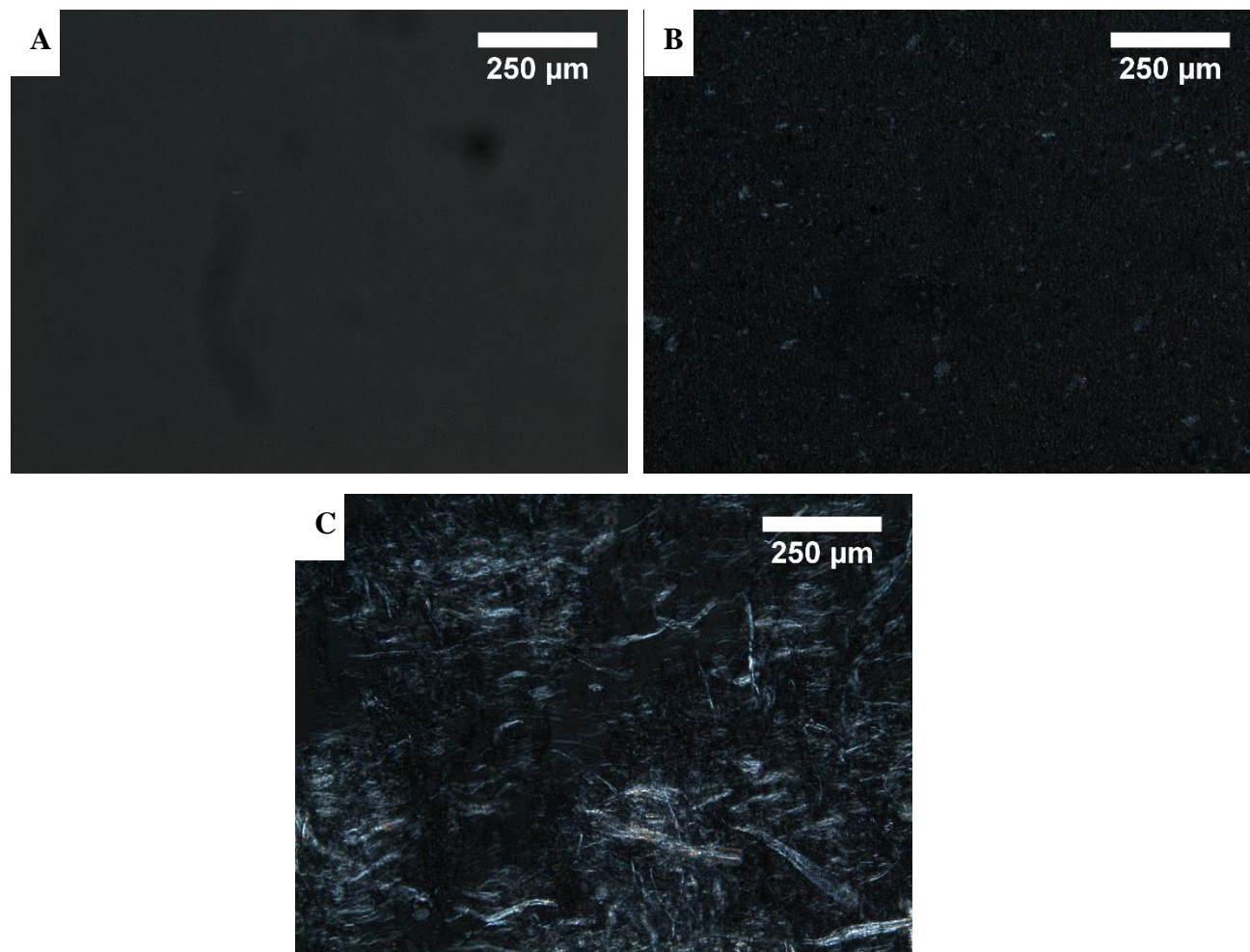


Figure 5.1 Polarized optical micrographs of cellulose nanocrystal (CNC) and polyethylene glycol (PEG) solutions at A) 1 wt% CNC, and B) 10 wt% CNC and cellulose nanofibril (CNF) in polyethylene glycol at C) 1 wt% CNF.

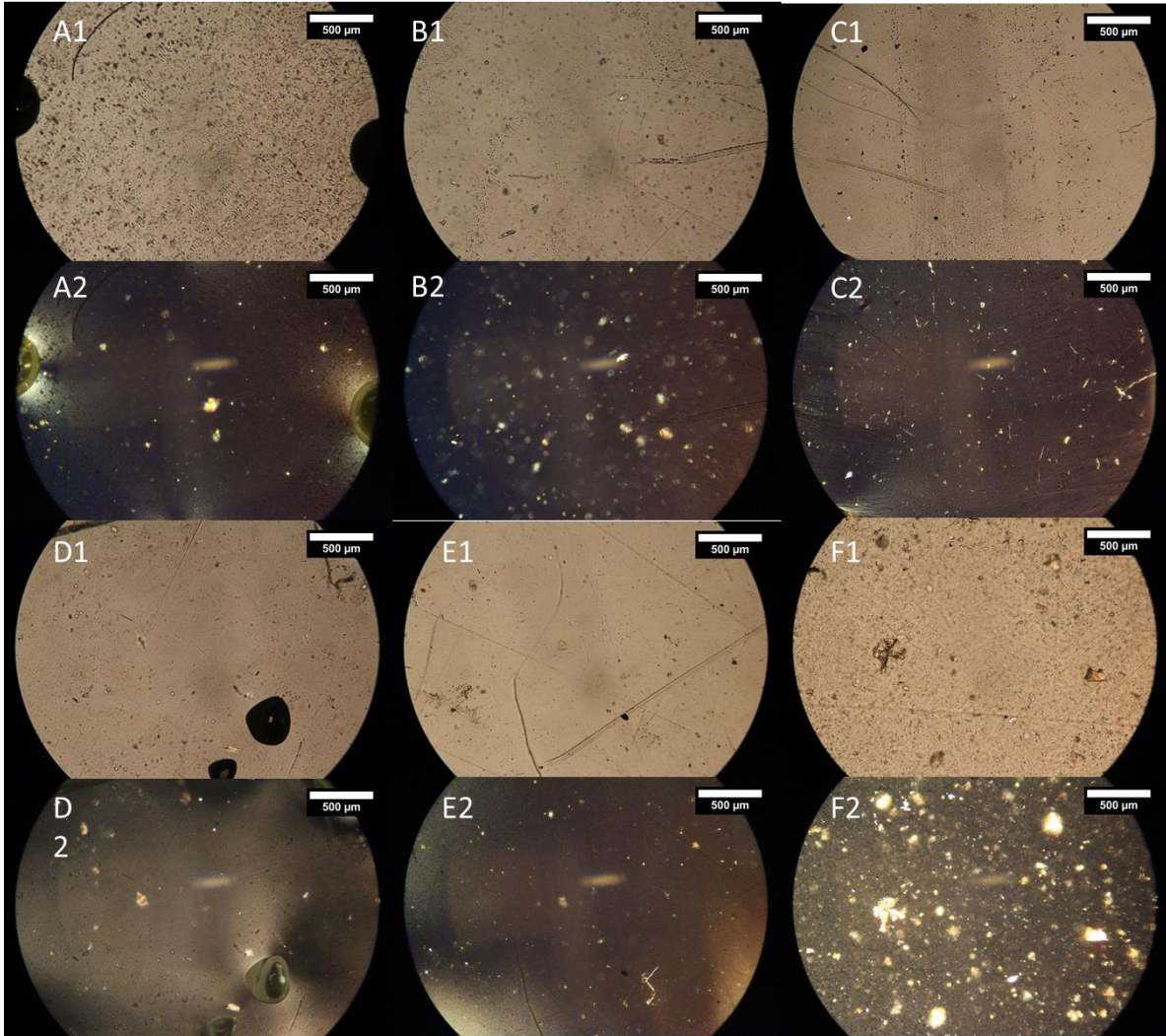


Figure 5.2 Non-polarized and polarized optical microscopy images of nanocomposites after compounding: A1-2) PLA, B1-2) PLA+5%PEG C1-2) 0.05% CNF-5%PEG-PLA, D1-2) 0.05% CNC-5%PEG-PLA, E1-2) 0.55% CNC-5%PEG-PLA F1-2) 0.05% Talc-5%PEG-PLA.

### 5.2.3 Methods for Thermal Analysis

All thermal experiments were performed in a Thermal Analysis (TA) Q800 differential scanning calorimeter (DSC). Samples were prepared in hermetically sealed aluminum pans with a mass of 11.1 +/- 2.9 mg. For non-isothermal experiments, materials were first held at 200°C for 2-5 min, quenched at 50°C/min and reheated to 200°C at 10°C/min; experiments were run in triplicate. Isothermal experiments were performed by first allowing the materials to fully melt at 200°C for 3-5 minutes then quenching (50°C/min) to the desired isothermal temperature ( $T_c = 90^\circ\text{C}$ , 100°C, 115°C, 120°C, and 130°C). All samples were held until crystallization had completed (indicated by a flat baseline) before a quench to 0°C and subsequent heat at 10°C/min to 200°C.

### 5.2.4 Characterization of PLA Spherulites

An FEI Quanta 650 FEG scanning electron microscope was used to image crystal morphology for chemically etched specimens. For this analysis, DSC samples were removed from the aluminum hermetic pans after isothermal aging at 90°C or 130°C and then quenched to room temperature. Chemical etching of isothermal specimens was performed by submersing specimens in a solution of 0.025mol/L NaOH in a 1:1 ratio of water/methanol for 4 hrs at 65°C following the procedure of He et al. [103,104]. After etching, samples were rinsed with water and methanol, then dried in a high vacuum for 30 min at room temperature to remove any residual solvent. Samples were sputter-coated prior to imaging with palladium/gold using an SPI Sputter Coater. SEM parameters for imaging were as follows: small working distance of 9-12mm, 2-5 KeV accelerating voltage, and a spot size of 3-4.

## 5.3 Results and Discussion

### 5.3.1 Avrami Crystallization Kinetics

Non-isothermal and isothermal history data capture the complex relationships of nucleation and growth with time and temperature and the effects of these different thermal histories can be observed in subsequent heating cycles. The following parameters were measured from DSC thermograms: glass transition ( $T_g$ ) measured as the inflection point, cold crystallization temperature ( $T_{cc}$ ) taken as the peak temperature, and melting point  $T_{m1}$  or  $T_{m2}$  as the temperature at the minimum of the well.  $T_{m1}$  is the melting point of the first melting peak (if exhibited) and  $T_{m2}$

is the second melting peak. The appearance of two melting peaks in PLA is commonly associated with the formation of the ordered and disordered  $\alpha$  and  $\alpha'$  phase, respectively [105–107]. The enthalpy of melting,  $\Delta H_m$  and enthalpy of cold crystallization,  $\Delta H_{cc}$ , are opposite in sign and were used to calculate the relative degree of crystallinity,  $\chi$ , from Equation 5.1 where  $\Delta H_m^\circ$  is the theoretical maximum melting enthalpy, 93 J/g [43,82,100]. For samples exhibiting an exothermic shoulder immediately before melting, the area under this peak was also subtracted from  $\Delta H_m$ ; details are in Appendix C, Figure C. 1.

Equation 5.1

$$\chi (\%) = 100\% \frac{(\Delta H_m + \Delta H_{cc})}{\Delta H_m^\circ (1 - w_{NC} - w_{PEG})}$$

A quench and subsequent heat indicated no detectable crystallization upon cooling at 50°C/min for the compositions explored and provided a baseline for material properties (Figure 5.3). The materials properties ( $T_g$ ,  $T_{cc}$ , and  $T_{m1}$ ,  $T_{m2}$ ) measured upon heating from Figure 5.3, were recorded in

Table 5.1. Compared to the neat PLA, all compositions showed a decrease in  $T_g$ ,  $T_{m1}$ , and  $T_{m2}$ , although only neat PLA and 0.05 wt% talc exhibited strong double melting peaks (Figure 5.3).

$T_g$  suppression is one of the measures for determining plasticizer efficiency and the observed values are comparable in magnitude to other PLA/PEG studies [82,83]. Likewise, decreased  $T_{cc}$  and  $T_m$  have been observed with the addition of nanocellulose as well as talc, which agreed with previous crystallization studies for both classes of materials [31,49,108]. Importantly, a decrease in

$T_{cc}$  (

Table 5.1) can be desirable as it implies that the crystallization window is moving to lower temperatures. For processing, this is better as thermal gradients in the part govern the degree of crystallinity throughout the component and by expanding this window, the crystallinity for the entire component can effectively be increased or the processing temperature can be lowered leading to more efficient processes.

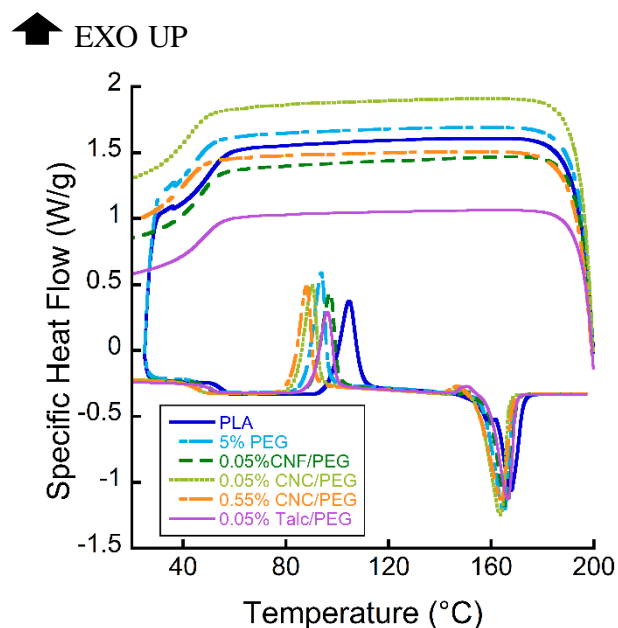


Figure 5.3 Experimental data for a 50°C/min cool followed by subsequent heating at 10°C/min. Exothermic is up in all thermograms.

Table 5.1. Thermal properties measured from non-isothermal experiments.

Sample	Nanocellulose (wt%)	PEG (wt%)	T <sub>g</sub> (°C)	T <sub>cc</sub> (°C)	T <sub>m1</sub> (°C)	T <sub>m2</sub> (°C)
Neat PLA	0	0	58.6±2.7	105.3±1.0	161.3±1.6	168.4±1.0
PEG	0	5	48.2±0.1	92.3±1.0	-	164.1±0.2
CNF/PEG	0.05	5	48.4±1.8	94.4±2.0	-	165.2±0.5
CNC/PEG	0.05	5	44.9±1.0	88.0±2.0	-	163.4±0.4
	0.55	5	45.8±1.0	88.6±1.2	-	163.6±0.2
Talc/PEG	0.05	5	50.4±3.2	95.7±4.2	-	164.7±1.8

The crystallization window provided by the temperature range of T<sub>cc</sub> was the basis for selection of isothermal crystallization temperatures, T<sub>c</sub>, and isothermal experiments were run at 90°C, 100°C, 110°C, 115°C, 120°C, and 130°C. While growth is favored at higher T<sub>c</sub>,

investigation of low  $T_c$  is industrially relevant as many plastic components are exposed to cooler surfaces during processing. For instance, low mold temperatures in injection molding are desirable as reducing mold temperature reduces cycle times and lowers cost if the mold does not have to be heated as high in temperature. As an example, in Figure 5.4 A-C, specific heat flow,  $\Delta H(t)/\Delta H_{total}$ , which has been used to calculate relative crystallinity conversion,  $\chi_c$ , is shown for 100°C. Generally, a steep slope suggests faster crystallization kinetics. From 100°C to 130°C,  $\chi_c$  is observed to take longer and longer times to complete conversion ( $\chi_c=1$ ) for a specific  $T_c$ . At the lowest  $T_c$ , 90°C,  $\chi_c$  is observed to shift right as well, suggesting that the maximum crystallization rate is between 90-110°C. To quantitatively determine the crystallization rate, the Avrami formalism was employed.

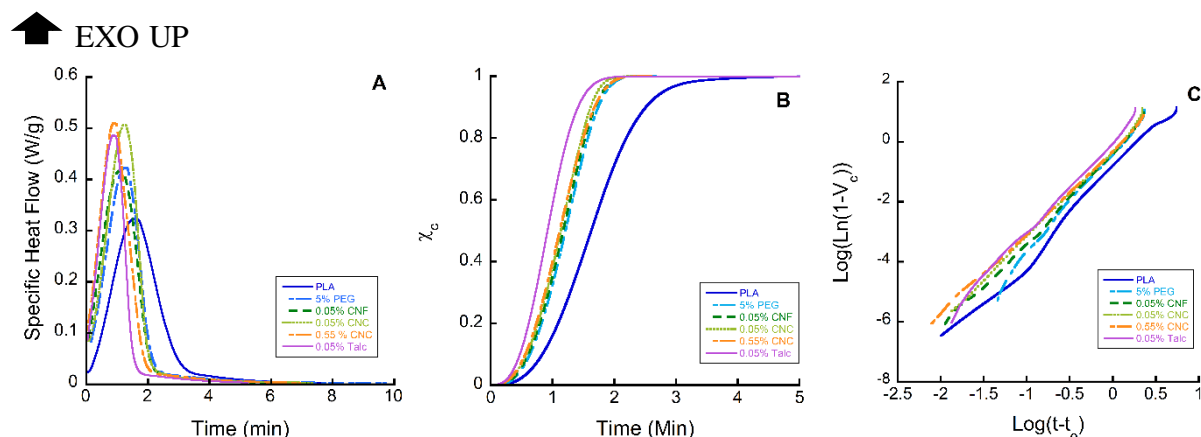


Figure 5.4 Progression of Avrami analysis from isothermal data at 100°C: A) Experimental isothermal data, B) Crystallinity conversion versus experiment time and C) Avrami type plot of  $\text{Log}(\text{Ln}(1-V_c))$  vs  $\text{Log}(t-t_0)$ . Exothermic is upwards in all thermograms.

Analysis of the isotherms was performed in Origin® with a custom Origin® plugin designed for Avrami and Lauritzen-Hoffman analysis by Lorenzo et al. [109]. In brief, a baseline was subtracted from the isotherms, for example, Figure 5.4 A and converted to  $\chi_c$  shown in Figure 5.4 B (all temperatures and compositions are provided in Appendix C, Figure C. 2 and Figure C. 3). The mass fraction of crystallized material,  $w_c$ , shown in Equation 5.2 is proportional to  $\chi_c$ . The volume fraction of converted material ( $V_c$ ) is then calculated from Equation 5.3, where the amorphous and crystalline densities were assumed to be  $\rho_a=1.25\text{g/cc}$  and  $\rho_c=1.359\text{g/cc}$  for poly(L-lactic acid) (PLLA). The software uses Equation 5.2 through Equation 5.5 to create the ‘Avrami

plot' of  $\text{Log}(-\text{Ln}(1-V_c))$  vs.  $\text{Log}(t-t_0)$ . A representative plot is shown in Figure 5.4 C. The Avrami index ( $n$ ) and rate constant,  $k$ , were determined from a linear regression of the Avrami plot for  $V_c=1-40\%$  to obtain an  $R^2=0.99$ . The rate constant,  $k$  combines the nucleation and growth rate contributions to describe the total crystallization rate. The Avrami exponent,  $n$ , is a value between 1-4 and is the sum of the dimensionality,  $n_d$ , and nucleation,  $n_n$ , components<sup>[110]</sup>. Theoretically,  $n_d$  can be integer values of 1, 2, or 3, and  $n_n$  can be either 0 (instantaneous nucleation) or 1 (sporadic nucleation)<sup>[110]</sup>. However, non-integer values of  $n$  are often observed because many materials are thought to be in a transition state between clearly defined modes. Generally, the morphology of the sample corresponds with  $n=1$  for a line,  $n=2$  is a sheet, and above  $n=3$  are spherulites<sup>[110]</sup>. Lastly, time for 50% conversion or the half-time,  $\tau_{1/2}$ , can be calculated from Equation 5.6<sup>[31,103,111]</sup>. These values are recorded in Table 5.2.

Equation 5.2

$$w_c \sim \chi_c = \frac{\Delta H(t)}{\Delta H_{\text{total}}}$$

Equation 5.3

$$V_c = \frac{W_c}{W_c + (\rho_c/\rho_a)(1 - W_c)}$$

Equation 5.4

$$1 - V_c(t) = \exp(-kt^n)$$

Equation 5.5

$$\text{Log}[-\text{Ln}[1 - V_c(t)]] = \text{Log}(k) + n\text{Log}(t)$$

Equation 5.6

$$\tau_{1/2} = \left(\frac{\ln(2)}{k}\right)^{1/n}$$

As the growth rate depends on the diffusion of polymer chains, the addition of PEG, which will improve molecular mobility, will affect the crystallization rate. Previous studies have observed improvement in crystallization for low molecular weight PEGs in PLA at concentrations of 5-20 wt%<sup>[83,112-114]</sup>. While it was expected that the addition of PEG would have a similar effect

here, the effects were relatively small. In Table 5.2,  $k$  was observed to increase slightly compared to the neat PLA, and  $\tau_{1/2}$  decreased for  $T_c=90-120^\circ\text{C}$ . The Avrami exponent,  $n$ , did not change significantly from that of neat PLA which was around  $n=3$  for 3 dimensional or spherulitic growth.

Table 5.2 Avrami isothermal kinetics data.

	<b>Nanocellulose (wt%)</b>	<b>PEG (wt%)</b>	<b><math>T_c</math> (<math>^\circ\text{C}</math>)</b>	<b><math>k</math> (<math>\text{min}^{-1}</math>)<sup>n</sup></b>	<b><math>n</math></b>	<b><math>\tau_{1/2}</math> (<b>min</b>)</b>
<b>Neat PLA</b>	0	0	90	0.0312	3.1	2.73
			100	0.161	2.9	1.66
			110	0.06	3.0	2.27
			115	0.0086	3.1	4.26
			120	0.00091	3.1	8.78
			130	0.000012	3.6	21.1
<b>PEG</b>	0	5	90	0.096	2.7	2.06
			100	0.17	2.9	1.63
			110	0.072	2.9	2.18
			115	0.053	2.7	2.55
			120	0.0065	3.1	4.58
			130	0.0000528	3.1	21.9
<b>CNF/PEG</b>	0.05	5	90	0.412	2.8	1.21
			100	0.404	2.9	1.20
			110	0.087	2.7	2.12
			115	0.027	3.0	3.04
			120	0.009	2.8	4.64
			130	0.00012	3.1	16.42
<b>CNC/PEG</b>	0.05	5	90	0.435	2.6	1.17
			100	0.436	2.7	1.16
			110	0.166	2.7	1.67
			115	0.095	2.7	2.04
			120	0.055	2.8	2.47
			130	0.00026	3.0	14.26
	0.55	5	90	0.37	2.8	1.25
			100	0.47	2.7	1.14
			110	0.078	2.8	2.14
			115	0.039	2.8	2.78

Table 5.2 continued

			120	0.0099	2.9	4.20
			130	0.000179	2.9	18.21
<b>Talc/PEG</b>	0.05	5	90	0.70	2.8	0.99
			100	0.84	2.8	0.93
			110	0.26	3.3	1.36
			115	0.186	3.0	1.53
			120	0.00265	3.9	4.3
			130	0.0000389	3.4	17.80

Table 5.3 Surface energies of various materials.

Material	Temperature (°C)	$\gamma_s^D$ (mJ/m <sup>2</sup> )	$\gamma_s^P$ (mJ/m <sup>2</sup> )	$\gamma_s$ (mJ/m <sup>2</sup> )	Reference
Poly(L-lactic acid), Natureworks Grade 4403	25	32.5	8.2	40.7	[95]
	190			26.9	
Sulfate-half ester CNC, FPI Innovations	25	40.9	28	68.9	[95]
	190			18.6	
Sulfate-half ester CNC, Forest Products Lab	30	46.5-66.9*	-	-	[115]
	60	37.3-48.8*	-	-	
TEMPO-oxidized CNF (ARBOCEL), JRS	30	44.3-52.4*	-	-	[115]
	60	39.1-44.7*	-	-	
Fibrillated ligno-CNF, in-house synthesis	-	43.2-48.6	3.5-8.5	46.7-53.9	[116]
Talc (natural)	-	38.1	13.2	51.3	[117]
Talc (synthetic)	-	46.2	18.3	64.5	[117]

\*Surface energy range represents different processing methods (air-drying, spray drying, and freeze-drying) for drying CNCs or CNFs for single source of the material. TEMPO-oxidized CNF were not used in this study, but due to limited data, are used as an analogue for mechanically fibrillated CNF.

With the addition of nucleation agents, larger changes in  $k$  and  $\tau_{1/2}$  were observed. The addition of CNC or CNF with 5% PEG caused  $k$  to increase more substantially than 5% PEG

suggesting that CNC and CNF are improving crystallization rate, specifically at low  $T_c$  like 90°C or 100°C (Table 5.2, Figure 5.5A). Consequently, an overall decrease in  $\tau_{1/2}$  was also observed (Table 5.2, Figure 5.5 B). At 0.05% CNF and both CNC compositions,  $k$  more than doubled at  $T_c=100^\circ\text{C}$  where the fastest crystallization rates were observed for all conditions. While the talc composition was faster at low  $T_c$ , the CNC was faster at 120°C and 130°C and the CNF was faster at 130°C. The comparison material, in this case, was a known nucleation agent for PLA, talc, and as expected, it improved the crystallization kinetics of PLA of which surface area and surface energy are important factors in determining nucleation efficiency [49]. Compared to CNC, the surface area/volume ratio of talc should be smaller since the talc particles were micron-scale, however, the surface energy of talc is probably lower than that of CNC or CNF at low temperature (Table 5.3). Furthermore, the surface energy is not expected to remain constant with temperature. As Khoshkava and Kamal demonstrated, the surface energy of CNC at room temperature is above PLA, but at 190°C, it is significantly lower [95]. This may explain why the CNC and CNF demonstrated faster crystallization at higher temperatures.

Interestingly, at low concentration, the crystallization rate of CNC and CNF are very similar despite the large difference in size between nanoparticles. Although CNFs have comparable widths, they are very long (several microns) compared to CNCs which are 5-20 nm wide and 20-500 nm long [2]. CNCs, which provide a higher total surface area per volume compared to CNFs are expected to be the superior nucleation agent. Also, CNFs have been observed to exhibit entanglements (Figure 1.1) which further limit the available surfaces for nucleation as these entanglements will most likely be carried over into the composite to some extent.

Several potential reasons exist for the observation that the CNC and CNF effects at small concentrations are very similar. First, surface energy differences between CNC and CNF may arise from the processing of these materials. The CNC has a sulfate half-ester that is substituted for some of the OH- in the acid hydrolysis process, which puts a negatively charged sulfate half ester,  $-\text{OSO}_3^- \text{H}^+$ , on the surface [33,118]. While the negative charge is effective at stabilizing CNC/water suspensions, it may also account for a slight change in surface energy making the CNC more hydrophilic compared to mechanically fibrillated CNF, and thus, less compatible with PLA. Comparing surface energy measurements for similar nanocellulose materials, this appears to be the case (Table 5.3). Secondly, the interfacial energy between the nanocellulose and PLA may be

changed by the addition of a plasticizer such as PEG due to the adsorption of the PEG onto the surface of CNC/CNF. A study by Angles et al. demonstrated that the interfacial energy between glycerol and cellulose whiskers was higher than the starch matrix these materials were meant to modify [119]. Thirdly, CNC/CNF may have a higher affinity for PEG than PLA causing partitioning of the PEG to the nanocellulose interphase. This has been observed for CNCs in polyurethanes where the CNC preferentially located in the polyol-rich soft blocks [120]. One would expect that a more hydrophilic CNC to be more affected than CNF. These additional factors could explain why the surface area is not the only driving factor in improving the crystallization rate.

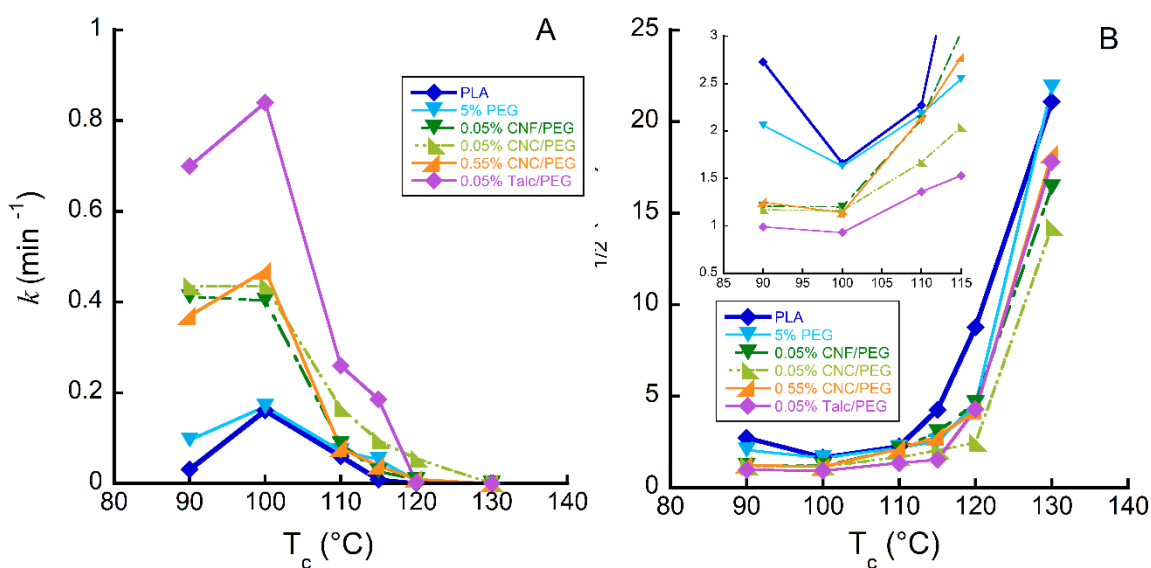


Figure 5.5 A) crystallization rate,  $k$ , and B) Half-time,  $\tau_{1/2}$ , versus  $T_c$  for all compositions

While the nanocomposites showed no optical indication of agglomeration, sub-micron agglomerations could persist despite best efforts to distribute and disperse the nanoparticles. In turn, this could reduce the effective surface area. Numerous studies have investigated the use of PEG as a material to help re-disperse dried CNC and have shown that in dried products, PEG does shield neighboring CNC interactions and CNC/PEG exhibited reversible hydrogen bonding when re-dispersed in water [94]. They also showed that the shielding was not 100% effective as after redispersion particle size was still larger than before [94]. Though similar behavior may be expected in the dry nanocellulose/PEG solutions employed in the present study, between the two concentrations examined here, the degree of agglomeration in the 10 wt% CNC/PEG solution

(Figure 5.1), appears to be slightly higher than lower CNC counterparts. CNC agglomeration would result in a lower effective surface area/volume ratio despite more CNCs being present. This may explain why a significant improvement in rate or half-time was not observed between 0.05 wt% and 0.55 wt% CNC despite an over ten-fold increase in nanoparticle concentration. Alternatively, higher concentrations of CNCs acting as a barrier to molecular motion, such as growing crystallites, has been proposed in several other materials and could be the case here as well, though the concentrations are much lower than expected <sup>[62]</sup>.

↑ EXO UP

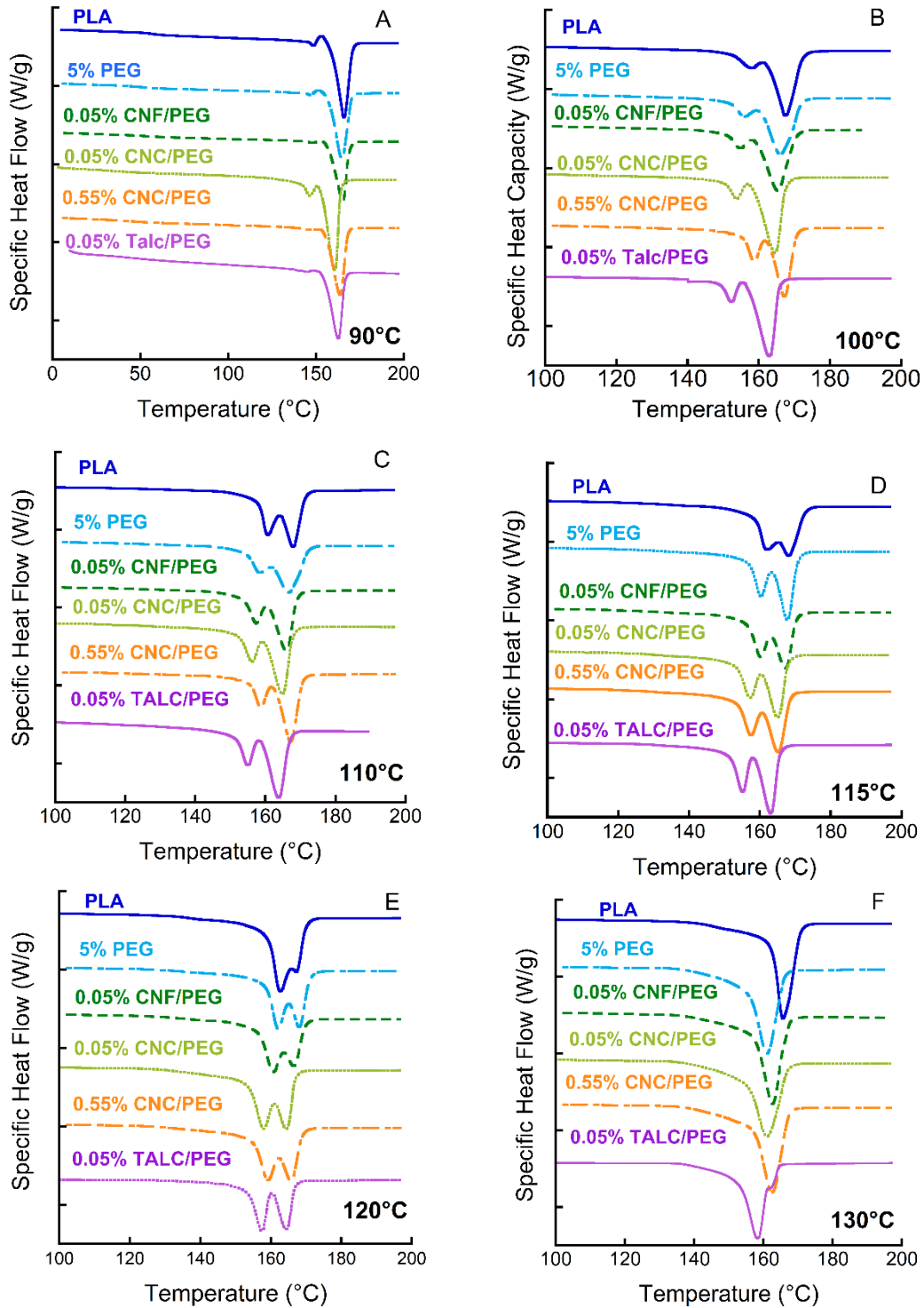


Figure 5.6 Thermograms after isothermal crystallization at A) 90°C B) 100°C C) 110°C D) 115°C E) 120°C F) 130°C. Exothermic is upwards in all thermograms.

### 5.3.2 Effects on Melting Behavior

Composition was shown to affect the melting behavior of isothermally crystallized samples as shown in Figure 5.6. PLA commonly crystallizes into an ordered  $\alpha$  phase and disordered  $\alpha'$  phase [105,121]. The two crystal structures are very similar and can be difficult to distinguish by wide-angle x-ray diffraction, however, the appearance of double melting peaks can be quite indicative of crystallization processes [105]. In poly(L-lactic acid) (PLLA), the  $\alpha'$  phase is known to crystallize at low  $T_c$  while  $\alpha$  phase crystallizes at high  $T_c$ ; the transition coincides with the appearance of the double melting peaks and the shoulder on the melting exotherm which sometimes appears is the  $\alpha'$  to  $\alpha$  transition [105–107,122]. The  $\alpha'$  phase is thought to undergo a solid-solid phase transition to the ordered  $\alpha$  phase when an exothermic shoulder is observed during heating cycles [107]. Both phenomena were observed in Figure 5.6. At 90°C, PLA and 5 wt% PEG compositions exhibited distinct exothermic shoulders immediately before the melting endotherm. The samples containing nucleation agents exhibited a very shallow melting endotherm, except for 0.05 wt% CNC which exhibited a strong endotherm, instead. However, all samples exhibited the shoulder in the non-isothermal history which would have undergone crystallization over a wide temperature range (Figure 5.3). After the materials switched to the melt recrystallization mechanism, either  $T_c = 90^\circ\text{C}$  or  $100^\circ\text{C}$ , the peaks in Figure 5.6 showed a distinct temperature dependence, where at low  $T_c$  the first melting peak is distinct from the second peak and as  $T_c$  increases, the two peaks become merged. At very high  $T_c$ , a single peak is observed ( $130^\circ\text{C}$ ) which agrees well with expectation [101,105]. While the melting points of peak 1,  $T_{m1}$ , increased with increasing  $T_c$ ,  $T_{m2}$  showed only weak temperature dependence which is to be expected as at elevated temperature, reorganized/regrown crystals will be more uniform in size and perfection (Appendix C, Figure C. 4). Of the nucleated compositions, talc exhibited the largest suppression in melting point,  $T_{m1}$ , followed by 0.05 wt% CNC, 0.55 wt% CNC, 0.05 wt% CNF, and then 5 wt% PEG (Appendix C Table C. 1). Smaller  $T_{m1}$  and broadening of the melting endotherm, like in Figure 5.6, suggests a smaller and/or less perfect, but wider distribution of crystallite sizes. Since the  $k$  increased, it is expected that crystallite size, and therefore  $T_{m1}$ , should decrease because of more nuclei growing means a smaller average size before growing into a neighboring crystal. Melting point suppression suggested that the 0.05% CNC and 0.05% talc would be the fastest crystallizing materials since these materials would be expected to have the smallest crystallite size distribution. Slight variations in experimental melting points could be due to variation between

samples as well as lamellar thickening during the thermal experiment either during crystallization or during subsequent heating. Regardless, a larger melting temperature can lead to higher temperature usage in polymers.

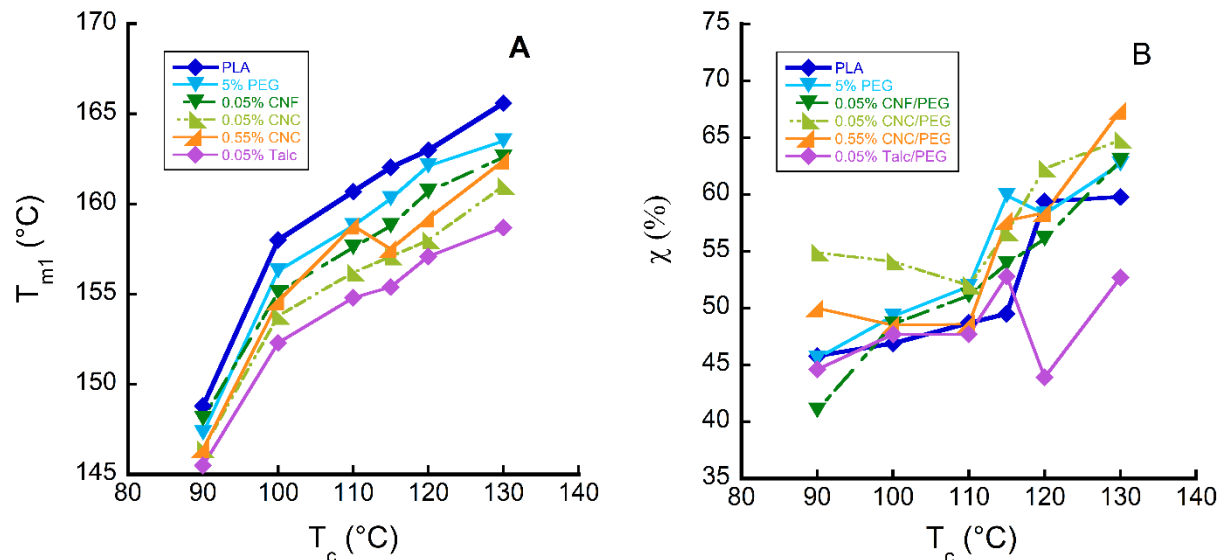


Figure 5.7 A)  $T_{m1}$  versus  $T_c$  and B) the crystallinity,  $\chi$ , versus  $T_c$ .

During isothermal crystallization, samples are held at  $T_c$  until the crystallization process is complete, and from the second heat, the degree of crystallinity,  $\chi$ , can be calculated using Equation 5.1. At higher  $T_c$ , the molecular mobility is higher and larger molecular weight chains can be more easily incorporated into the crystal. Consequently,  $\chi$  is observed to increase with increasing  $T_c$  over the range selected (Figure 5.7 B; Appendix C Table C. 1). Although the total degree of crystallinity is improved at higher  $T_c$ , the rate of crystallization, Table 5.2, decreases with increasing  $T_c$  even if growth is favored at higher temperatures and the time to complete crystallization at a given temperature dramatically increases. This is because, at higher  $T_c$ , nucleation is the limiting factor in determining the crystallization rate. Samples containing nanocellulose exhibited higher  $\chi$  compared to the neat PLA, 5% PEG, and 0.05% talc. Interestingly, from Table 5.2, the half-time was comparable or smaller for these materials which suggest that the nanocellulose/PEG combination is improving growth in addition to nucleation, the primary contribution in improving the crystallization kinetics of PLA. Larger  $\chi$  is generally correlated to better properties such as heat deflection temperature and gas barrier and is a major reason that nucleants are added to

polymers. In this case, nanocellulose may be superior in some instances as it leads to higher overall crystallinity than nucleants such as talc.

### 5.3.3 Nonlinear Hoffman-Weeks Extrapolation of the Equilibrium Melting Temperature

The non-linear Hoffman-Weeks expression, Equation 5.7, was used to estimate the equilibrium melting temperature,  $T_m^\circ$ , from experimental melting point data [123]. The expression was fit using Matlab. The Matlab code is reported in Appendix C.

Equation 5.7

$$\frac{T_m^\circ}{T_m^\circ - T_m} = \gamma \frac{\sigma_e^1}{\sigma_{em}} \left( \frac{T_m^\circ}{T_m^\circ - T_c} + a \right)$$

Where  $\sigma_e^1$  and  $\sigma_{em}$  are folding surface energies and the approximation that  $\sigma_e^1 = \sigma_{em}$  was assumed. The thickening coefficient,  $\gamma$ , was assumed to be  $\gamma=1$  for PLA [103]. Five values ( $T_c=100, 110, 115, 120,$  and  $130^\circ\text{C}$ ) were fit. For more information, see Chapter 3 of Polymer Crystallization by J. M. Schultz [110].

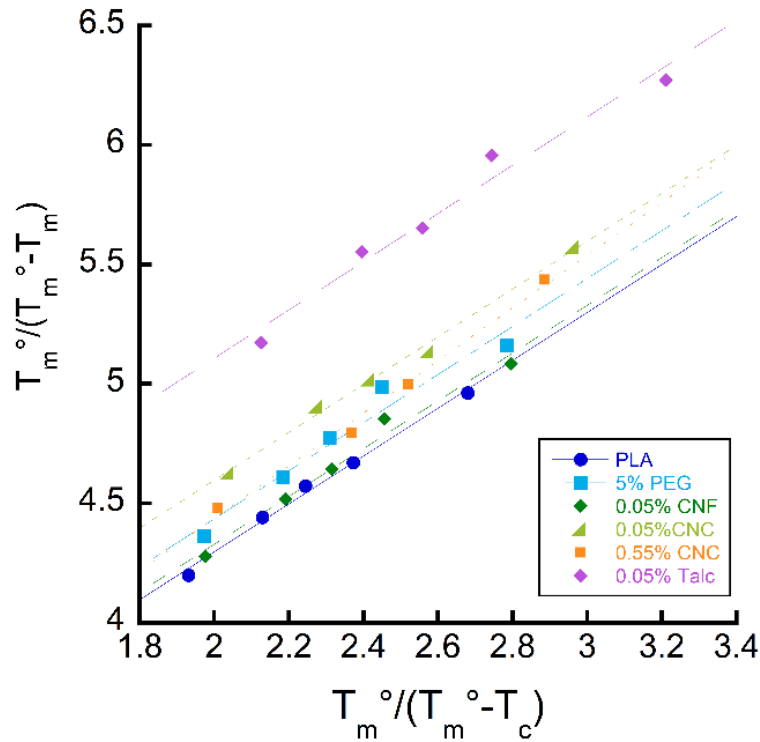


Figure 5.8 Summary plot of nonlinear Hoffman-Weeks estimation of the equilibrium melting temperature for all materials.

### 5.3.4 Nucleation Efficiency from Secondary Nucleation Theory

Secondary nucleation theory provides access to additional information about nucleation efficacy and growth. Lauritzen and Hoffman's expression for the growth rate in Equation 5.9 consists of two primary components: the activation energy barrier for diffusion of chains to the growth front and the surface energy component to overcome during the addition of strands on a layer, i.e. the initial process of nucleation<sup>[110]</sup>. While the former is represented by the first exponent, the latter is represented in the second in which  $K_g$  is the nucleation constant. The growth rate data were approximated as,  $G=1/\tau_{1/2}$ , where  $U^*=1500$  cal/mol,  $T_\infty= T_g-30^\circ\text{C}$  (

Table 5.1),  $R$  is the ideal gas constant,  $\Delta T= T_m^\circ-T_c$ , and  $f$  is a correction factor ( $f=2T_c/(T_c+T_m^\circ)$ )<sup>[31]</sup>. The equilibrium melting temperature,  $T_m^\circ$ , was estimated from a nonlinear Hoffman-Weeks extrapolation (Figure 5.8) and is reported in Table 5.4<sup>[110]</sup>.  $T_m^\circ$  estimates were in the acceptable range for various PLA materials<sup>[31,103,122–126]</sup>. Variation in  $T_m^\circ$  could be the consequence of lamellar thickening during the isothermal experiments<sup>[103]</sup>. Equation 5.8 was rearranged and plotted in Figure 5.8 where the slope of the line is  $K_g$ .

Equation 5.8

$$G = G_o \exp\left(\frac{-U^*}{R(T_c-T_\infty)}\right) \exp\left(\frac{-K_g}{T_c \Delta T f}\right)$$

Surface energy terms that describe nucleation are buried in  $K_g$  (Equation 5.9). In Equation 5.9,  $K_g$  is the energy required for nuclei of a critical size to form which depends on several factors such as the free energy of folding,  $\sigma_e$ , the lateral surface energy,  $\sigma$ , thickness of a single layer,  $b$ , the Boltzmann constant,  $k_B$ , enthalpy of melting per unit volume,  $\Delta H_f$ , and  $n$ , which corresponds to the three crystallization regimes<sup>[110]</sup>. The three regimes are regime I, regime II, and regime III<sup>[110]</sup>. In regime I and regime III,  $n=4$  and in regime II  $n=2$ <sup>[110]</sup>. Polymers can exhibit a combination of the regimes or a single regime. PLA most often exhibits regimes II and III<sup>[124,127]</sup>.

Equation 5.9

$$K_g = \frac{nb\sigma\sigma_e T_m^\circ}{\Delta H_f k_B}$$

All compositions exhibited linear behavior in Figure 5.9. As PLA can exhibit multiple regimes across the temperature range explored, a test was applied to determine quantitatively if one or two regimes were present. Since  $n=4$  for regimes I and III and in regime II  $n=2$ , the ratio of various slopes at high and low temperatures can be used to test whether two regimes are present.

$T_c = 115\text{ }^\circ\text{C}$  was initially assumed to be the division point when testing for the presence of multiple slopes in data.  $K_{gIII}/K_{gII} = 2$  by measuring the ratio of slopes between high and low  $T_c$  from Figure 5.9, there was no conclusive evidence that any of the compositions exhibited a second regime above  $115\text{ }^\circ\text{C}$ . The slopes in Figure 5.9 are observed to decrease as the composition is changed which indicated that the energy for nuclei to form is decreasing as well. Theoretically,  $T_m^\circ$  should not change since only the PLA is crystallizing. However, for the present study, unique  $T_m^\circ$  was estimated for each composition and so, the data is also observed to shift right as the experimentally fit  $T_m^\circ$  was observed to decrease for the more efficient nucleating compositions. The exhibited regime was assumed to be regime III as regime 3 is the commonly observed regime in PLA and is typically reported to cover the temperature region below  $115\text{-}125\text{ }^\circ\text{C}$ . The parameters used for the custom Origin plugin developed by Lorenzo et al. where:  $a = 5.17$ ,  $b = 5.97$ , and  $\Delta H_f = 1.26 \times 10^8 \text{ J/m}^3$  [109]. The results of the linear regression of Figure 5.9 are shown in Table 5.4 where the slopes of the trend lines,  $K_g$ , are tabulated and additional parameters from Eq. 8 have been calculated and reported.

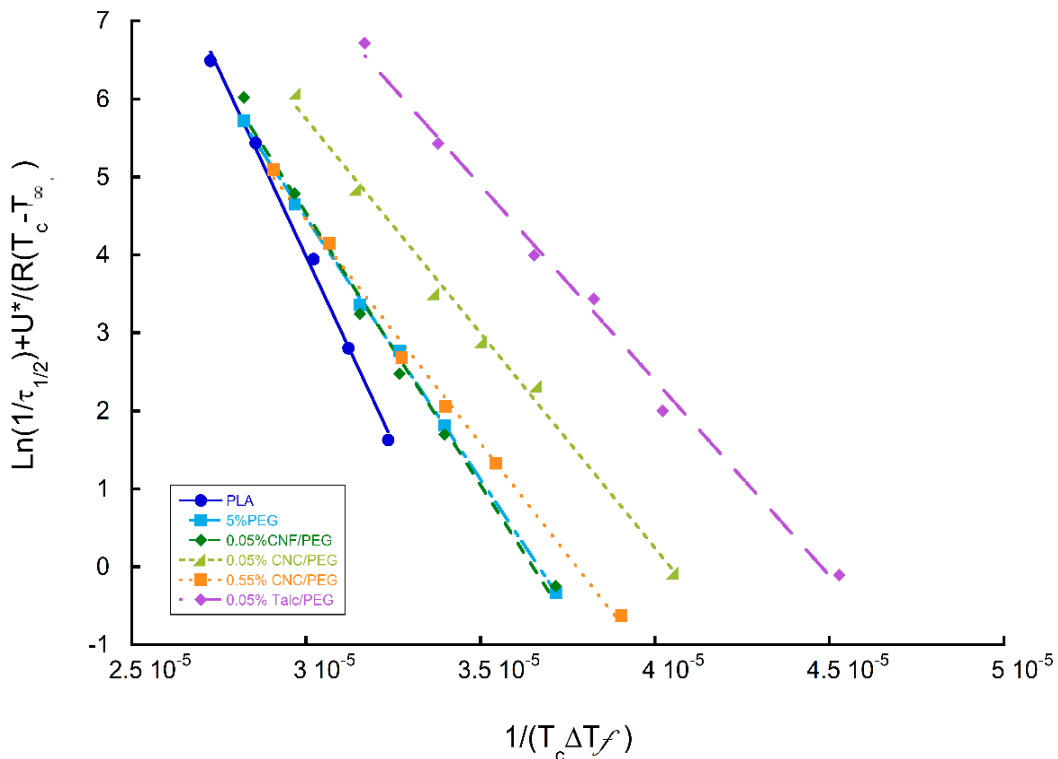


Figure 5.9 Plot of  $\ln(1/\tau_{1/2}) + U^*/(R(T_c - T_\infty))$  vs.  $1/(T_c \Delta T_f)$ .

From Table 5.4, it was observed the  $K_g$  and  $\sigma_e$  both decreased with the addition of PEG and nucleation agents. From,  $\sigma_e$  was observed to decrease for all compositions. The reduction in  $\sigma_e$  was largest for talc, followed by CNC indicating that, at this concentration, these materials are the superior nucleation agent as the energy required to create a new fold is reduced in the presence of a desirable nucleation surface. Between 0.05 wt% CNC and 0.55 wt% CNC,  $\sigma_e$  was very similar (141 and 146.1 erg/cm<sup>2</sup>) which is to be expected and the difference between the two concentrations is acceptable in light of previous CNC concentration studies [31]. At small concentrations, CNC is not expected to form a percolation network that can inhibit crystallization and the difference in  $\sigma_e$  may simply be due to variation in the fitting of the growth rate or  $T_m^\circ$  or experimental variation. The 5 wt% PEG and 0.05 wt% CNF appear to be very similar in Figure 5.9. The addition of PEG produced a decrease in  $K_g$  indicating that increasing the mobility of PLA chains is enough to reduce  $\sigma_e$  while the addition of 0.05% CNF did not further reduce  $\sigma_e$  or  $K_g$ .

Table 5.4 Secondary nucleation theory parameters.

Material	$T_m^\circ$ (°C)	$K_g$ (10 <sup>5</sup> K <sup>2</sup> )	$\sigma_e$ (erg/cm <sup>2</sup> )	$\sigma$ (erg/cm <sup>2</sup> )	$\sigma \sigma_e$
Neat PLA	207.4	8.69	217.3	7.02	1525.5
5 wt% PEG	202.8	6.71	169.3	7.02	1188.5
0.05 wt% CNF 5 wt% PEG	202.4	6.97	176.1	7.02	1236.2
0.05 wt% CNC 5 wt% PEG	196.2	5.51	141.0	7.02	989.8
0.55 wt% CNC 5 wt% PEG	199.0	5.7	146.1	7.02	1025.6
0.05 wt% Talc 5 wt% PEG	188.8	5.0	130.2	7.02	914.0

### 5.3.5 Crystal Morphology

Crystal morphology is of key interest as crystallite size and morphology, in part, determine materials properties such as opacity or melting point. Neat PLA and PLA blends have been previously shown to exhibit banded spherulitic structures under certain conditions [128–130]; e.g. blends of poly(ethylene oxide) (PEO) and PLA exhibited highly periodic banded spherulites when crystallized at 125°C [128]. The morphology of compositions in the present study was examined by SEM after chemically etching samples that had been isothermally crystallized at two temperatures: 90°C and 130°C (Figure 5.10 and Figure 5.11). Conceptually, the poor solvent mixture dissolved the less crystalline and amorphous areas of the surface as well as the water-soluble PEG; only highly crystalline areas were left behind. At low  $T_c$ , SEM micrographs showed non-spherulitic, unordered structures similar to that of the low  $T_c$  PLA structures observed previously (Figure 5.11) [103]. At low  $T_c$ , growth will be severely hindered and so a large amount of material remained amorphous/disordered and was dissolved during etching. Likewise, samples crystallized at low  $T_c$  exhibited smaller  $\chi$  values upon reheating compared to high  $T_c$ , and crystallized structures, which were very small, would be expected to have low melting points like those observed (Figure 5.6). High  $T_c$  conditions produced spherulites across all compositions. The centers, containing the nuclei of the spherulites, were also dissolved during etching. This has been observed by other authors for PLA and a potential reason for the etching out of centers is that the nuclei are disordered compared to the outer layers that are placed later [103,104]. This phenomenon was observed across all high  $T_c$  samples, but to different degrees along with spherulite size as the nucleate type and concentration was varied.

The addition of PEG alone changed the crystal morphology of PLA. PLA spherulites were denser and fuller (very fine lamella), with distinct interfaces between neighboring spherulites comparable to those previously observed for high molecular weight PLA [103]. The addition of PEG produced large, coarse spherulites where small gaps between neighboring crystals could be observed; this space may be caused by the ejection or exclusion of PEG to the interface during crystallization. Additionally, larger pores or pockets of free space were observed in the samples after etching (Figure 5.10 C-D). The spherulites in Figure 5.10 are not reminiscent of banded spherulites since they do not exhibit a periodic structure across the spherulite but are isolated. Two potential reasons are solute ejection and/or phase separation of the PEG during crystallization or spherulite fall-out/pull-out. Full phase separation is unlikely as no distinct melting or

crystallization peaks around 15-25°C, which correspond to low molecular weight PEG, were observed in the DSC thermograms (Figure 5.6). However, solute ejection of the PEG ahead of the crystallization front may still be occurring if the PEG is simply higher in concentration and forming a solid solution. Studies on the solubility of PEG in PLA have reported that phase separation occurs above 10% and coincides with the appearance of a melting/crystallization peak in the DSC thermogram <sup>[83]</sup>, so that if solute ejection is happening, the concentration of PEG in PLA cannot be above this value. Thus, it is more likely that pull-out, where loose spherulites would have fallen out during chemical etching as the amorphous regions were dissolved, occurred instead, although any solute ejection that raises the PEG concentration locally at the periphery may make this more likely.

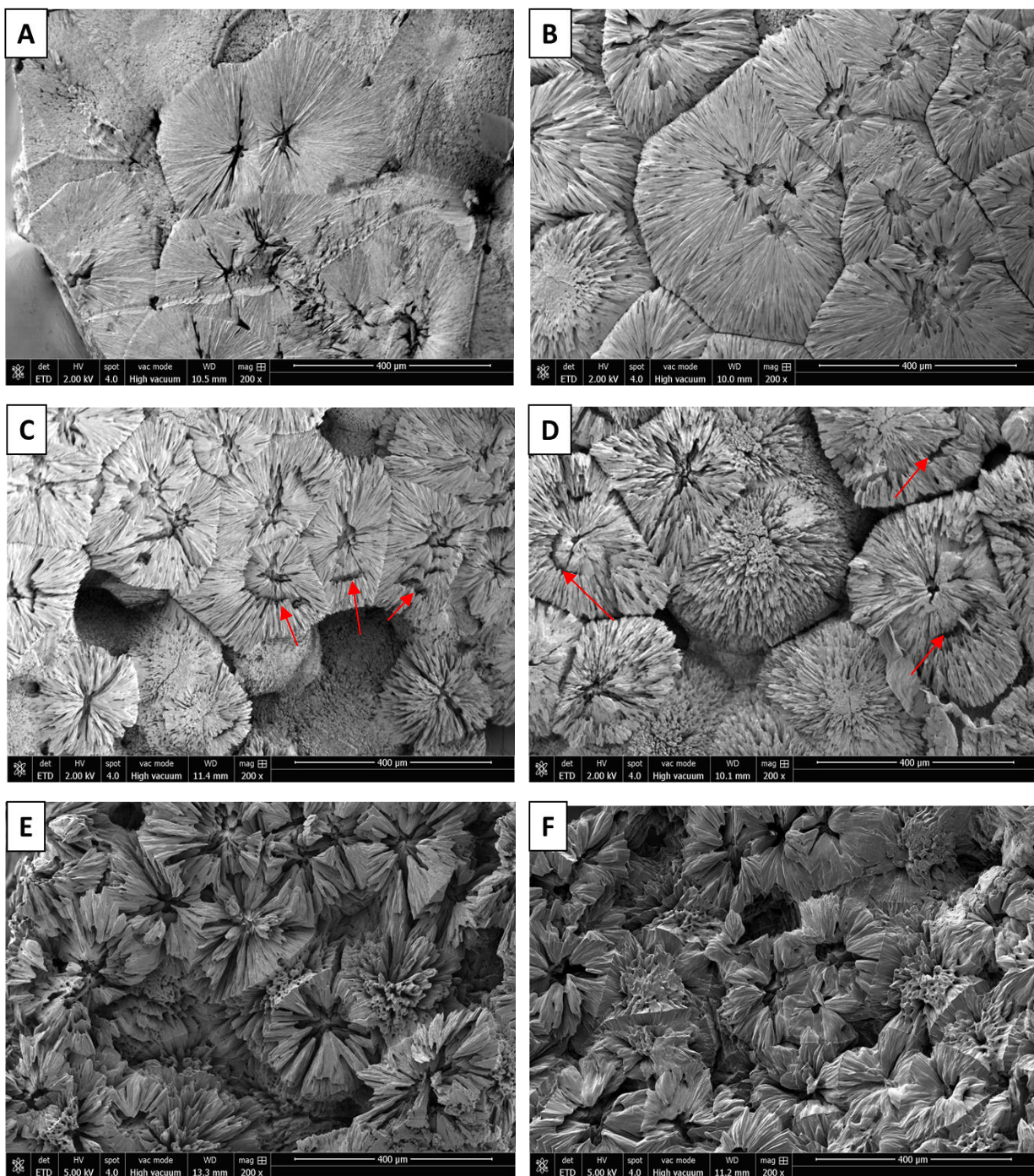


Figure 5.10. Scanning electron micrographs of chemically etched specimens isothermally crystallized at 130°C: A) Neat PLA, B) 5 wt% PEG, C) 0.05 wt% CNF-5 wt% PEG, D) 0.05 wt% CNC-5 wt% PEG, E) 0.55 wt% CNC-5 wt% PEG, and F) 0.05 wt% Talc-5 wt% PEG. Arrows indicate regions where “core-shell” morphologies (single bands which were preferentially etched away) formed in some of the spherulites.

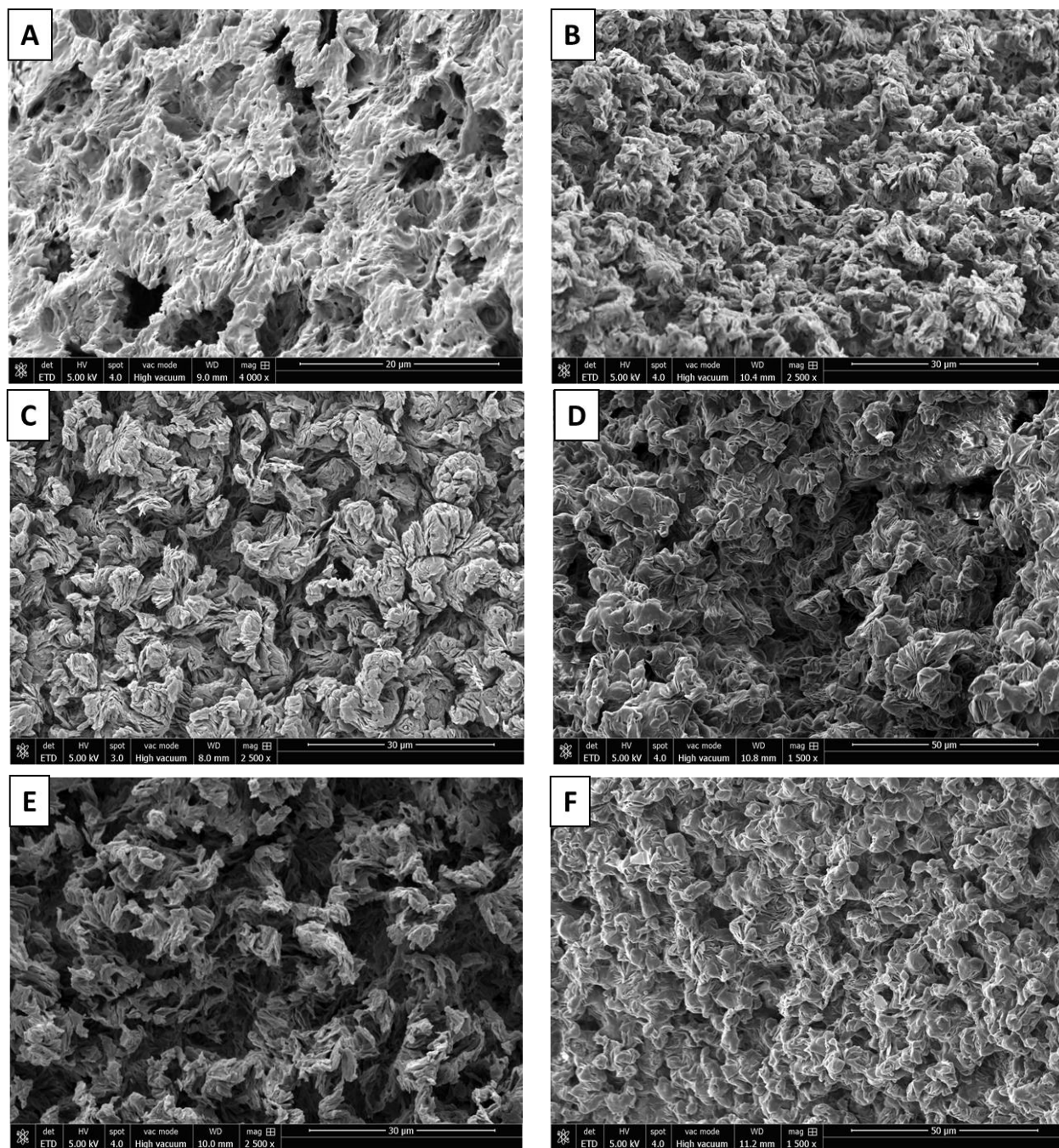


Figure 5.11 Scanning electron micrographs of compositions isothermally crystallized at 90°C and then chemically etched for 4hrs in a 1:1 ratio of water and methanol with 0.025mol/L NaOH. Compositions are as follows: A) Neat PLA, B) 5 wt% PEG, C) 0.05 wt% CNF-5 wt% PEG, D) 0.05 wt% CNC-5 wt% PEG, E) 0.55 wt% CNC-5 wt% PEG, and F) 0.05 wt% Talc-5 wt% PEG.

The addition of nucleation agents (CNC, CNF, or talc) resulted in additional changes to the crystal microstructure of PLA. Like the 5 wt% PEG, samples containing a nucleation agent and PEG also exhibited evidence of crystallite pull-out (Figure 5.10 C-D). Unlike the neat PLA, samples with additives are growing faster due to enhanced growth from mobility and nucleation and thus, significant coarsening of the microstructure is observed. Coarsening of the microstructure and large grain size can lead to poor mechanical performance. For the 0.05 wt% nanocellulose compositions, a shell microstructure can be observed around some crystallites (Figure 5.10 C-D; Figure 5.12). Although talc compositions did not exhibit a similar shell around spherulites, talc did show a slight reduction in size compared to samples containing nanocellulose or only PEG. As expected, talc is a good nucleation agent for PLA as many nuclei were formed, the crystallization rate was improved (Table 5.2) and the surface energy reduction (Table 5.4) was largest for talc.

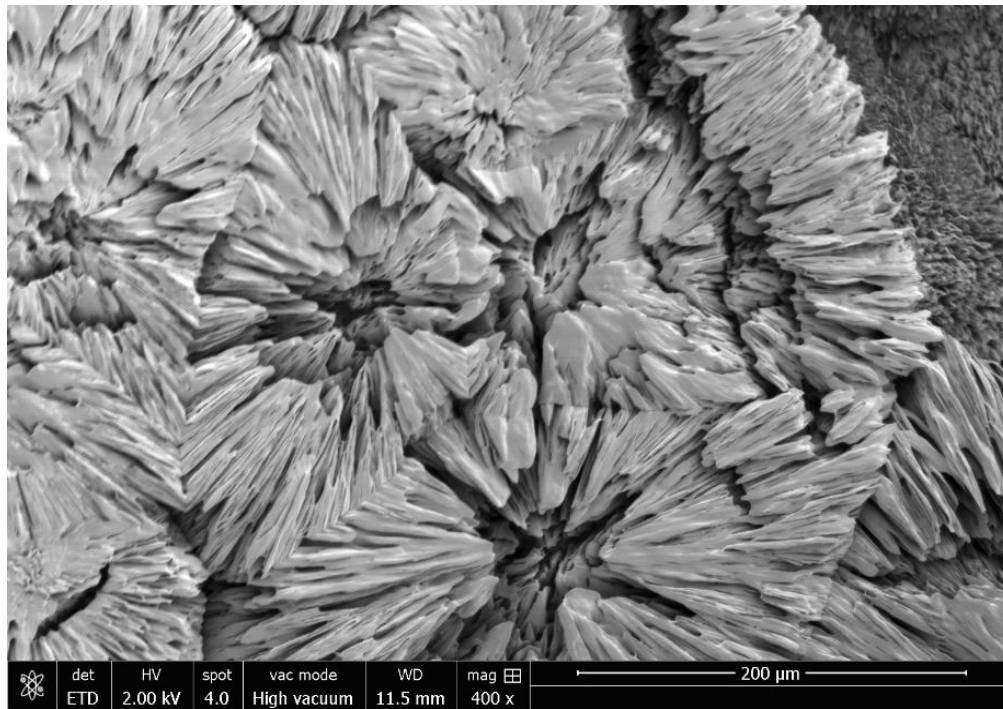


Figure 5.12 Micrograph of 0.05 wt% CNF-5 wt% PEG isothermally crystallized at 130°C and then chemically etched.

## 5.4 Conclusions for Crystallization Kinetics

In the present study, polymer nanocomposites were prepared using PEG as a plasticizer and as a compatibilizer for CNC and CNF as nucleants for PLA, with talc being used as a commercial comparison. Very small concentrations of CNC and mechanically fibrillated CNF, similar to those used for commercial nucleation agents, were investigated as heterogeneous nucleation agents using conventional kinetics approaches: Avrami and Lauritzen-Hoffman formalisms. Isothermal crystallization kinetics were studied for a wide temperature zone that spanned the temperature range where  $\alpha'$  to  $\alpha$  transitions. At high  $T_c$ , the CNC and CNF containing compositions were faster than talc. The Lauritzen-Hoffman analysis showed a decrease in the nucleation constant,  $K_g$ , and a decrease in the surface energy of folding,  $\sigma_e$ , suggesting that at very small concentrations CNC and CNF are good potential nucleation agents for PLA.

Additionally, the spherulite morphology was studied through chemical etching of the isothermally crystallized samples and morphologically, the nucleation agents produced very different results. For isothermal samples at  $T_c=130^\circ\text{C}$ , the addition of 5 wt% PEG produced a coarse structure which was made coarser by the addition of CNC or CNF and suggested that these composites were indeed crystallizing faster at the higher  $T_c$  compared to talc. While the microscopy images cannot provide an estimate of spherulite size, the spherulites of the nanocellulose compositions did appear smaller, but not as small as the talc comparison group which exhibited both lower melting points in the DSC thermograms and visually smaller spherulites in the micrographs.

Overall, the CNC and CNF were found to be efficient nucleants with faster crystallization kinetics than talc, a commercial PLA nucleant, at high temperatures, and with a similar morphology for the concentrations examined. Importantly, CNF and, especially, CNC were found to give a significantly higher overall crystallinity, indicating that they may, ultimately, give better properties than the commonly used talc for the concentrations examined.

## 5.5 Acknowledgments for Crystallization Kinetics

The authors would like to thank Professor Alejandro Müller for sharing the custom Origin Plugin used for the Avrami and Lauritzen-Hoffman analysis in this study.

The authors would like to acknowledge financial support from the Private-Public Partnership for Nanotechnology in the Forestry Sector (P3Nano) under Grant No. 107528, the Forest Products Laboratory Grant Number 17000384, and National Science Foundation Integrative Graduate Education and Research Traineeship: Sustainable Electronics Grant (Grant Number 1144843).

## 6. PRELIMINARY PROCESSING OF NANOCELLULOSE/POLYAMIDE COMPOSITES

All lab work in this chapter was performed by Caitlyn Clarkson. All writing was done by Caitlyn Clarkson.

### 6.1 Introduction

Polyamides have challenged researchers as high processing temperatures have hindered attempts to create nanocomposites<sup>[7]</sup>. However, polyamides like nylon 6, nylon 11, and nylon 12 are industrially very relevant polymers. Nylon 6 is ubiquitous as it is used in many products from the textile industry to the automotive industry. It is also one of the higher melting point nylons (210-220°C) compared to nylon 11 (180-190°C) or nylon 12 (170-180°C) due to the frequency of hydrogen bonding groups along the polymer backbone; i.e. the number of carbons between the aliphatic diamine part and the aliphatic carbonyl part is only six. Regardless, there is interest in putting nanocellulose in nylons because of the potential for mechanical reinforcement<sup>[7]</sup>.

This chapter discusses the initial investigation into applying the processing concepts developed for melt-processing nanocellulose into PLA to create nylon 6 nanocomposites. A similar approach, where a known additive is chosen to carry/compatibilize the nanocellulose is employed. Several studies have recently examined alternative plasticizers for nylon 6 and nylon 66/6 copolymers<sup>[131-133]</sup>. Of these studies, a few potential plasticizers were selected. In a computational study by Alperstein *et al.*, methyl-4-hydroxybenzoate (M4HB) was predicted by to reduce the T<sub>g</sub> and be a more efficient plasticizer compared to other plasticizers like glycerol monostearate (GMS) and benzene sulfonamide<sup>[132]</sup>. All three of these plasticizers were chosen as was ethyl-4-hydroxybenzoate (E4HB), which is similar in chemical structure to M4HB. The following section discusses the thermal properties of plasticizers, method for incorporating CNCs into GMS, and initial thermal properties of nylon 6 nanocomposite films prepared for two types of CNCs. Additionally, Appendix D contains initial work on determining the Hansen solubility parameters (HSP) for the nanoparticles used in this chapter and for predicting polymer and additive compatibility based on the cohesion parameters.

## 6.2 Methods and Materials

### 6.2.1 Materials

Nanocelluloses were purchased from two providers. Sulfuric acid CNCs were purchased from the University of Maine, Orono, ME, USA: Forest Products Laboratory (FPL CNCs) (2014-FPL-CNC-065; 1.9 % CNC-water slurry; 0.99wt% sulfur on dry CNC). Blue Goose (BGB) Ultra carboxyl CNCs (BGU<sup>2</sup> CNC), obtained from a transition metal-catalyzed oxidative process, were purchased from Blue Goose Biorefineries Inc., Saskatoon, SK Canada (Lot number: VPU07-001; 8 % CNC-water; Carboxyl content, 0.15mmol/g). Nanoparticle dimensions for FPL-CNCs are in Table 4.1 and BGU<sup>2</sup> CNCs, provided by the manufacturer, is 9-14 nm by 100-150 nm. From Millipore Sigma, St. Louis, MO, USA, the following analytical purity chemicals were purchased: polyethylene glycol (PEG600,  $M_n = 600\text{g/mol}$ ); nylon 6; methyl-4-hydroxybenzoate (M4HB); ethyl-4-hydroxybenzoate (E4HB); benzenesulfonamide, glycerol monostearate (GMS). All other solvents were analytical grade with a purity of >99%. All water was nano-pure, deionized water generated in-house using a Barnstead device.

### 6.2.2 Exchanging CNCs from Water into Additives

A general process for exchanging CNCs into ethanol-soluble plasticizers was developed. First, A 70% ethanol solution of GMS was prepared by mechanically mixing GMS at 70°C. Meanwhile, CNCs from water was diluted with additional water (to create a 30% water-70% ethanol final solution composition) and sonicated using Branson Sonifyer (30% power, 30 sec total, 1 min on and 1 min off). After diluting that CNCs, the solution was preheated to 70°C while being mechanically mixed. Once both solutions were preheated, the CNC/water solution was gradually added to the GMS/ethanol solution under vigorous mechanical mixing. The solution was then transferred to a round bottom flask that had been preheated to 70°C in the rotary evaporator water bath. Solvents were removed from the plasticizer/CNC solution in three vacuum stages. First, the rotary evaporator at 250 mTorr was used to remove the bulk of the solvent. Second, the rotary evaporator was set to maximum vacuum (80mTorr) and the additional solvent was removed while the sample was cooled to 25°C in the water bath. After cooling to room temperature, the plasticizer/CNC solution had formed a thick, white, tacky paste. In the third vacuum stage, the paste was deposited onto a glass tray and put into a high vacuum at 70-80°C for 4-5 hrs or until all

solvent had been removed as confirmed by TGA. After drying, the powders were ground into a fine powder using a mortar and pestle. All materials were stored in a desiccator to prevent water absorption before use.

### **6.2.3 Nylon 6 Nanocomposite Processing**

An Xplore 5CC twin-screw microcompounder, equipped with a continuous feed hopper and nitrogen blanket was used to process nanocomposites. The nitrogen blanket is essentially a nozzle that releases nitrogen over the hopper and barrel of the compounder. Since nitrogen is heavier than oxygen, it will displace the air in the hopper to create a low oxygen/low humidity environment. The utmost care was taken to ensure that all materials were dry before use as nylon is very sensitive to water. Nylon 6 was dried at 90°C for 4-5 hrs before use and stored in airtight containers filled with desiccant. A premeasured quantity of nylon 6 and plasticizer/CNC were measured by mass on the scale located immediately next to the microcompounder to prevent water adsorption prior to processing. The premixed powder and pellets were added into the continuous hopper while the screws ran at 200 rpm. All temperature zones were set to 235°C. The materials were compounded in the closed chamber for 3 min before being collected between two metal plates and flattened to form pre-flattened sheets for compression molding. A clearing batch of nylon was run between compositions or when the material appeared to be oxidizing heavily.

Films were compression molded from the compounded material on a Carver benchtop hydraulic press. The temperature was set to 235°C. To prepare samples, 4 grams of pre-flattened material was measured and then stacked on top of each other on polytetrafluoroethylene (PTFE) sheets with a metal shim insert. The shim was 0.25µm thick and a square of 15 cm x 15 cm was cut from the middle. A second PTFE sheet was placed on top of the assembly and then the mold was sandwiched between two preheated stainless steel plates and loaded onto the press. The assembly was warmed up, without pressure, for 5.5 min. Then a pressure of 0.75 metric tons was applied for 1.5 min. The mold assembly was removed and cooled between two 4 cm thick aluminum heat sinks until it reached room temperature and then was de-molded.

#### **6.2.4 Thermal Properties of Potential Additives and Nanocomposites**

A Thermal Analysis (TA) Instruments Q 500 TGA was used to determine the onset of thermal degradation. Since all melt compounding procedures would be conducted under a nitrogen blanket to reduce oxidation of nylon 6, the tests were run in nitrogen at 15°C/min from 25°C to 900°C.

A TA Q2000 DSC was used to collect the thermal properties of additives and nanocomposites. Tzero hermetic pans with each additive were prepared at approximately 10 mg +/- 2 mg. Samples were run through a heat-cool-heat program where the rate was 10°C/min. Generally, the program was 0°C to 250°C unless the thermal degradation temperature was below 250°C in which case the upper limit was 200°C.

### **6.3 Results for Polyamide Processing**

#### **6.3.1 Thermal Properties of Polymers and Potential Additives**

Thermal degradation and the melting point of various potential additives were measured and are reported in Table 6.1. As a rule of thumb, the processing temperature for polymers is about 20-30° higher than the melting point. For nylon 6, that is 215°C, so the polymer was melt compounded at 235°C. Considering this criterion, several potential additives could be eliminated from the list immediately. E4HB and M4HB were eliminated as the onset of thermal degradation for these materials were well below the processing temperature. Of the additives surveyed, that left GMS and benzenesulfonamide. Of these two plasticizers, benzenesulfonamide is very compatible with CNCs based on its HSP (Appendix D). It is within the HSP spheres of both BGU<sup>2</sup> CNC and FPL CNC, while the three monoglycerides used as approximations for GMS are not. Solubility tests showed that GMS could be dissolved in 30% water-70% ethanol at 70°C which could also be used to disperse CNCs. While benzenesulfonamide is soluble in methanol, this additive was not chosen initially as mixtures of methanol/water could not be obtained where CNCs and benzenesulfonamide both stayed in solution.

Table 6.1 Table of thermal properties for polymers and potential additives for nylon 6 composites.

Material	T <sub>m</sub>	T <sub>deg</sub> Onset Peak 1	T <sub>deg</sub> Peak 1	T <sub>deg</sub> Peak 2	T <sub>deg</sub> Peak 3
GMS (from ethanol)	61.2	231.7	267.6	407.6	
M4HB	126.5	173.1	209.2	-	-
E4HB	116.7	175.6	209.3	-	-
Benzene sulfonamide	153.6	222.13	252.97	-	-
Nylon 6	215.2	431.9	460.6	-	-

### 6.3.2 Nylon 6/CNC Composites

CNC/nylon 6 nanocomposites were prepared at 5% GMS and 10% GMS via melt-compounding for FPL CNC and one concentration at 5% and 0.55% for BGU<sup>2</sup> CNC (Figure 6.1 A). The additive solutions showed no evidence of browning since they were made at 70°C. Visually, there was no difference between the FPL CNC/GMS and BGU<sup>2</sup> CNC/GMS powders developed as the first additive combination (Figure 6.1 B). Furthermore, the as-processed materials showed marginal browning after compounding for samples compounded with GMS and more browning for samples with CNCs. In particular, BGU<sup>2</sup> CNC/GMS nanocomposites showed the most browning compared to GMS controls, nylon 6, and FPL CNC/GMS nanocomposites (). This is surprising considering that browning is often attributed to sulfuric acid CNCs in the literature<sup>[7]</sup>.

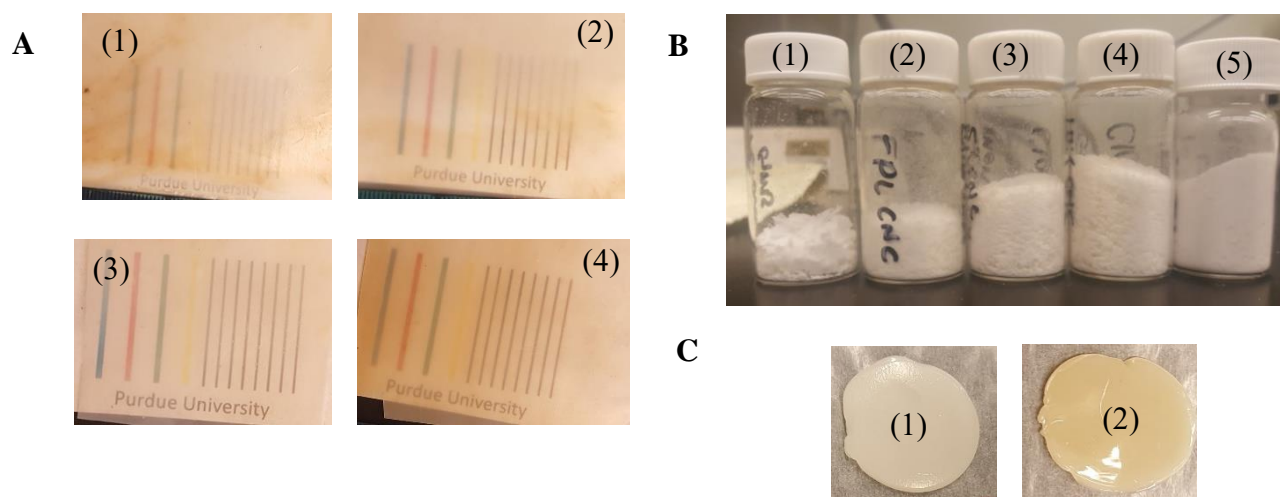


Figure 6.1 A) Compression molded films of nylon 6 nanocomposites: nylon 6 (1), 5 wt% GMS (2), (3) 5 wt% GMS-0.55 wt% FPL CNC; (4) 5 wt% GMS-0.55 wt% BGU<sup>2</sup> CNC. B) Plasticizer solutions used to prepare films: (1) GMS; (2) 1 wt% FPLCNC-GMS; (3) 5 wt% FPL CNC-GMS; (4) FPL CNC-GMS; (5) BGU

However, all controls and nanocomposite films show evidence of browning after compression molding at 235°C for 7-8 additional minutes (Figure 6.1 A).

### 6.3.3 Thermal Properties of Nylon 6/CNC Composites

Table 6.2 shows DSC data collected for controls and nanocomposites containing GMS and either FPL CNC or BGU<sup>2</sup> CNC. Three concentrations of FPL CNCs were prepared to determine the effect of CNC concentration and plasticizer content. The DSC thermogram of the as-made compounded material prior to compression molding is shown in Figure 6.2. In Figure 6.2 A, little difference is observed between concentrations, however, there does appear to be a very slight dip around the glass transition temperature of nylon 6. In Figure 6.2 B this peak is more pronounced and is centered around 60°C, the melting point of GMS. This is evidence that close to 5% GMS in nylon 6 has reached the solubility limit of this material. Furthermore, it obscures the T<sub>g</sub> so that the suppression of the T<sub>g</sub> can be determined from these measurements. The enthalpy of melting, ΔH<sub>m</sub> stays approximately the same for all FPL CNC compositions shown in Table 6.2 and the melting point increased with the addition of 10% GMS and FPL CNC from 217°C to 220°C.

Table 6.2 Thermal properties of nylon 6 composites.

Material	GMS (wt%)	CNC (wt%)	T <sub>g</sub> (°C)	T <sub>m1</sub> (°C)	T <sub>m2</sub> (°C)	ΔH <sub>m</sub> (J/g)
<b>Compounded</b>						
Neat Nylon 6	0	0.0	47.5	217.26	-	57.4
FPL CNC/GMS	5	0.05	42.6	219.5	-	55.5
FPL CNC/GMS	5	0.25	43.0	216.0	-	56.7
FPL CNC/GMS	5	0.55	43.2	215.3	-	55.0
FPL CNC/GMS	10	0.10	-	220.5	-	56.1
FPL CNC/GMS	10	0.50	-	220.6	-	54.9
FPL CNC/GMS	10	1.10	-	220.2	-	55.7
<b>Films</b>						
5 wt% GMS	5	0.0	40.8	214.5	220.7	39.8
BGU <sup>2</sup> CNC/GMS	5	0.55	-	211.2	222.4	61.8
FPL CNC/GMS	5	0.55	-	211.3	221.3	65.9

Since the DSC thermograms of the compounded material exhibited a GMS melting peak superimposed on the T<sub>g</sub> of nylon 6, future studies only examined 5% GMS. Figure 6.2C is shown

for three samples which were compression molded to make the films in Figure 6.1 A. The melting behavior of these samples changed. For reference, the compounded samples would have a very fast cooling history because they were quenched immediately, while the films have time to develop crystallinity during the slower cool down in the film process. Interestingly, there appears to be a second peak which appears as a shoulder on the primary melting peak (Figure 6.2). This peak could correspond to melt crystallization, or it could be a second crystal structure that is nucleated during the film processing history. Further investigation is needed, but an estimate of the shoulder peak temperature is provided in Table 6.2 alongside the primary melting peak ( $T_{m2}$  for thermograms showing two melting peaks). Like the compounded materials, the  $T_m$  of the primary melting peak increased.

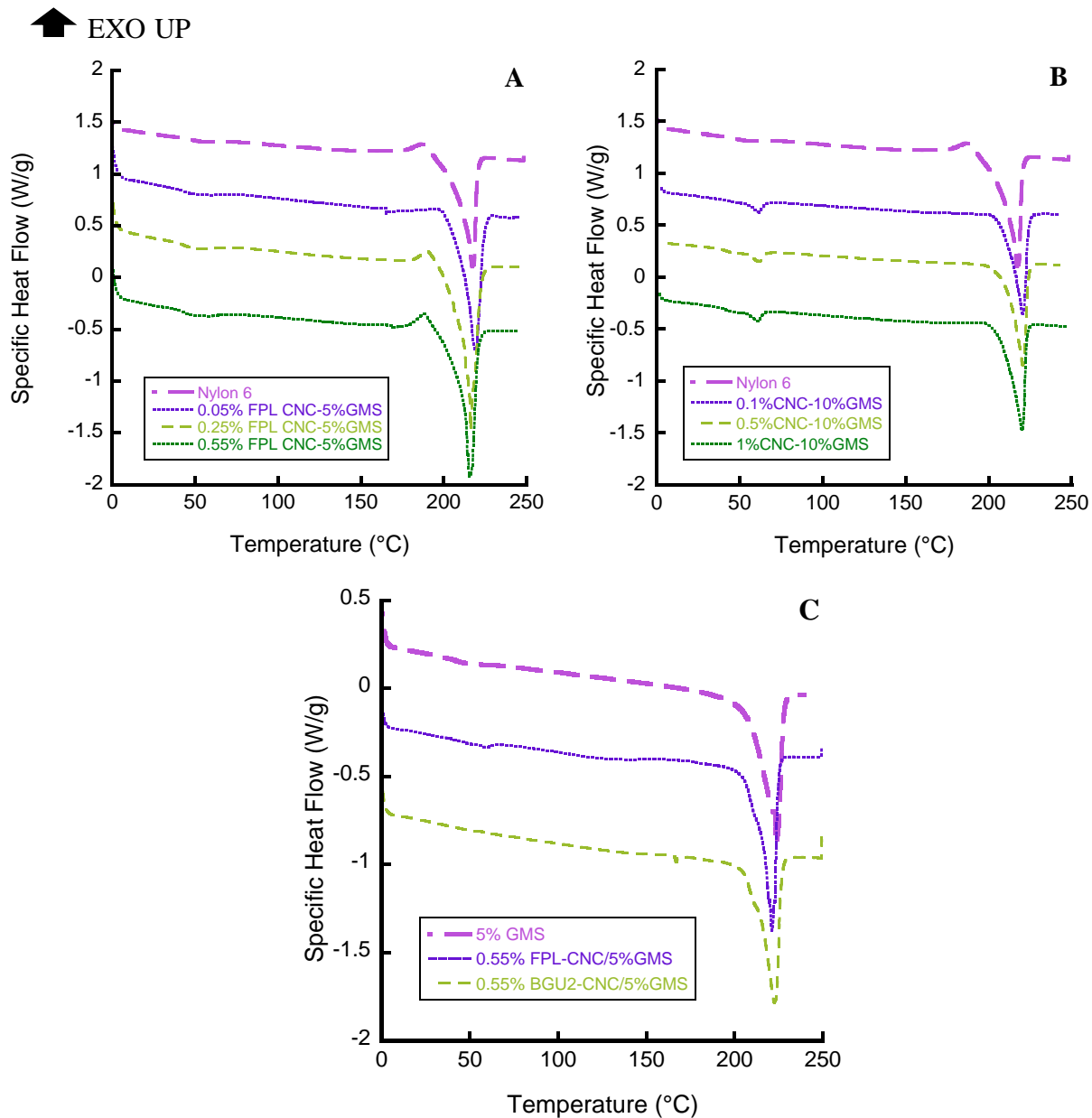


Figure 6.2 DSC thermograms of heating cycles of A) 5 wt% GMS-nylon 6 and B) 10 wt% GMS in nylon 6; both are with FPL CNC at 0.05 wt%, 0.25 wt% and 0.55 wt% and C) comparison of 5 wt% GMS and 5 wt%GMS/0.55 wt% CNC (BGU<sup>2</sup> CNC or FPL CNC). Exothermic is up in all DSC thermograms.

## 6.4 Summary and Future Work

Nylon6/GMS/CNC plasticizer mixtures were prepared using a similar concept to the plasticized PLA/CNC or PLA/CNF composites addressed in Chapters 3-5. This method appears promising despite the fact the GMS and CNCs are not highly compatible based on the HSP spheres shown in Appendix D. However, the mechanical performance needs to be tested to determine the how effective small concentrations can be and to determine if GMS is an efficient plasticizer for nylon 6 as the computations predicted by nylon 66/6 <sup>[132]</sup>.

Future work could explore the exchange of CNMs into benzenesulfonamide. Potential methods for doing so include the solvent-based methods such as the methods used for CNM/PEG or CNC/GMS. However, considering the compatibility prediction between these materials, melt mixing of dried CNMs into benzene sulfonamide may prove a promising avenue. Since GMS reaches a solubility limit in nylon 6 at around 5%, another avenue for future investigation would be to use a combination of plasticizers (GMS and benzenesulfonamide for instance). The benefit being that CNCs could be exchanged into one of the materials which would act as a compatibilizer while the other serves primarily as a plasticizer for the material.

## 7. SUMMARY

This thesis covered five projects intimately related to the processing and characterization of nanocellulose/polymer composites. Individual project objectives were oriented under two primary thrusts: 1) improving mechanical properties and 2) improving crystallization kinetics in PLA as it is a slow crystallizing polymer. Under the first thrust in improving mechanical properties were two fiber spinning projects, and under the second was the crystallization kinetics study of PLA. This also covered preliminary work leading up to the conceptualization of the crystallization kinetics project as well as preliminary work in creating nylon 6 nanocomposites using concepts developed in the melt-processing projects for PLA.

The fiber spinning projects had several notable discoveries. In the first project, a method to dry-spin CNC/PLA nanocomposite fibers was developed and fibers with up to 5% CNC were produced at various screw rotation speeds. Since dimethylformamide was used as the solvent, the process was performed at elevated temperatures to help drive off the higher boiling point solvent. Interestingly, the onset of melt fracture was observed in fibers which were not alleviated by the addition of CNCs. This phenomenon has been observed previously by researchers using good solvents as well<sup>[38]</sup>. In the second fiber spinning study, a process to melt-spin mCNF-C12/PLA nanocomposite fibers was developed. This work was inspired by the solvent-assisted method of Herrera et al. who used a liquid assisted melt-process to create nanocellulose composites<sup>[21]</sup>. A key benefit to the method developed and what differentiated it was that the method was solvent-less which meant that no specialized compounding equipment with the capability to vent large amounts of water was needed to create the fibers. Furthermore, the process demonstrated that small concentrations of nanoparticles could be effective in improving the mechanical properties, especially when coupled with hot-drawing the fibers along the fiber axis. Up to 600% improvement in elastic modulus was observed for this study. This work motivated the preliminary study of small concentrations of CNMs in plasticized PLA.

In the crystallization kinetics project, the combined effect of CNCs and CNFs with a plasticizer, PEG, was studied. To the best of the author's knowledge, this is one of two studies in the field which explored CNCs as a heterogeneous nucleation agent in plasticized PLA<sup>[58,134]</sup>. Also, the study examined very small concentrations of CNCs and CNFs, typical of commercial nucleation agents. The crystallization rate was improved with the addition of these materials,

though not to the extent that talc can accelerate the crystallization rate. Additionally, the morphology of samples was examined by chemically etching the surface which enabled the observation of microstructural changes in nanocomposites isothermally aged at a high and low temperature.

Lastly, preliminary work on the development of a process to melt-compound nylon 6 nanocellulose composites which produced minimal discoloration was presented. In support of this project, the Hansen Solubility Parameters (HSP) were estimated using relative sedimentation time for an entirely water-miscible system.

## APPENDIX A: DRY-SPINNING POLY(LACTIC ACID) NANOCOMPOSITE FIBERS

Table A. 1 Thermal properties of CNC/PLA composite fibers.  $T_{cc}$  is the cold crystallization temperature and  $\chi$  is the degree of crystallinity.

<b>CNC Content (%)</b>	<b><math>T_{cc}</math> (°C)</b>	<b>X (%)</b>
0 wt% (as cast)	133.00 +/- 1.49	2.40 +/- 1.5
<b>5 RPM</b>		
0	84.90 +/-1.49	27.40 +/-1.27
1	90.77 +/-2.83	36.86 +/-6.96
3	89.28 +/- 0.64	28.64 +/-2.02
5	90.89 +/- 0.10	26.23 +/-2.86
<b>25RPM</b>		
0	122.00 +/- 6.90	24.02 +/- 0.85
1	116.00 +/- 8.90	31.53 +/- 4.74
3	114.90 +/- 8.10	28.00 +/- 2.92
5	112.00 +/- 11.50	27.79 +/- 4.66
<b>50 RPM</b>		
0	90.46 +/- 6.43	26.01 +/-10.07
1	92.40 +/- 4.27	34.90 +/-0.24
3	91.72 +/- 0.62	18.39 +/-0.91
5	85.89 +/- 1.2	24.57 +/-1.24

Table A. 2 Mechanical properties of CNC/PLA composite fibers.

<b>CNC Content (%)</b>	<b>Strength at Failure (20-35 <math>\mu\text{m}</math>)</b>	<b>Strength at Failure (40-55 <math>\mu\text{m}</math>)</b>	<b>Strength at Failure (60-75 <math>\mu\text{m}</math>)</b>
0	93.30 +/- 40.00	34.45 +/- 18.00	33.80 +/- 3.34
1	71.80 +/- 18.00	23.30 +/- 6.00	25.40 +/- 2.89
3	99.20 +/- 31.80	55.46 +/- 2.59	26.80 +/- 2.68
5	58.55 +/- 5.90	44.13 +/- 4.41	
<b>CNC Content (%)</b>	<b>Elastic Modulus (20-35 <math>\mu\text{m}</math>)</b>	<b>Elastic Modulus (40-55 <math>\mu\text{m}</math>)</b>	<b>Elastic Modulus (60-75 <math>\mu\text{m}</math>)</b>
0	5.78 +/- 1.87	3.22 +/- 0.49	2.07 +/- 0.20
1	5.51 +/- 2.34	4.50 +/- 1.45	4.63 +/- 0.72
3	5.55 +/- 0.65	5.48 +/- 5.48	3.55 +/- 1.39
5	4.43 +/- 0.44	6.57 +/- 0.32	

## APPENDIX B: MELT SPINNING POLY(LACTIC ACID) NANOCOMPOSITE FIBERS

### Thermogravimetric Analysis (TGA) of Unmodified and Modified Nanocellulose Fibrils

TGA was performed on dried, unmodified and modified CNF materials in air at a ramp rate of 10°C/min (Figure B. 1 A-B). It clearly shows two degradation transitions for both materials. The first degradation temperature of both modified mCNF-C12 and unmodified CNF was 314.0°C and 305.7°C, respectively. However, the upper degradation temperatures are very different. The onset of thermal degradation is 469.2°C and 526.7°C for CNF and mCNF-C12, respectively. Low-temperature weight loss in these specimens is most likely due to water evaporation.

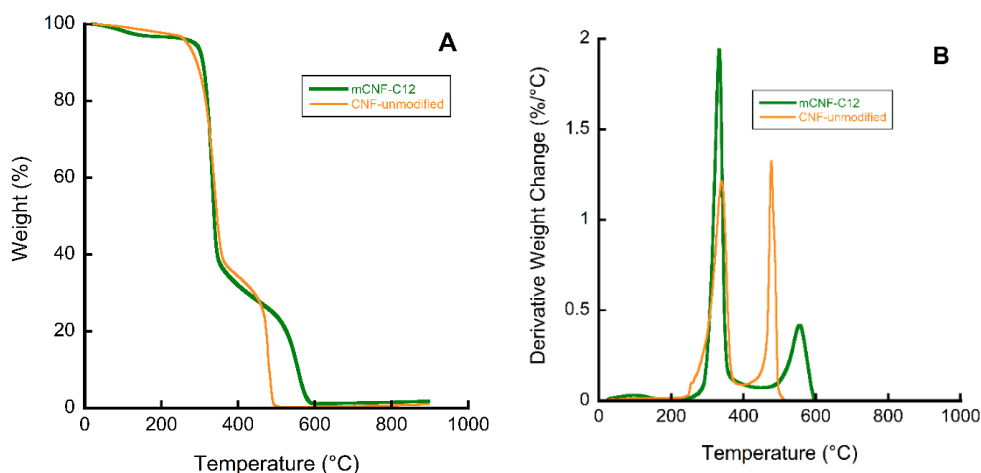


Figure B. 1 Thermogravimetric analysis (TGA) curves of modified and unmodified mechanically fibrillated CNF in air after drying. A) Weight change with temperature and B) derivative weight change with temperature are shown.

### Differential Scanning Calorimetry (DSC) Measurements

Methods for the determination of thermal values from DSC measurements are provided in this section. An example is shown in Figure B. 2 DSC thermogram of PLA fibers showing the areas of integration for the enthalpies recorded in Table 3.1 and the positions for  $T_{cc}$  and  $T_m$  for as-spun PLA fibers.

- $T_g$  was measured as the inflection point/midpoint at the transition between 40-60°C.

- $T_{cc}$  and  $T_m$  were measured as the maximum and minimum peak temperature positions, respectively.
- $\Delta H_{cc}$  is the enthalpy of cold crystallization for the area shown in Figure B. 2 DSC thermogram of PLA fibers showing the areas of integration for the enthalpies recorded in Table 3.1 and the positions for  $T_{cc}$  and  $T_m$ .
- $\Delta H_m$  is the enthalpy of melting for the area shown in Figure B. 2 DSC thermogram of PLA fibers showing the areas of integration for the enthalpies recorded in Table 3.1 and the positions for  $T_{cc}$  and  $T_m$ . (the melting enthalpy minus the exothermic enthalpy peak immediately before melting which corresponds to the re-organization of the disordered  $\alpha'$  phase).

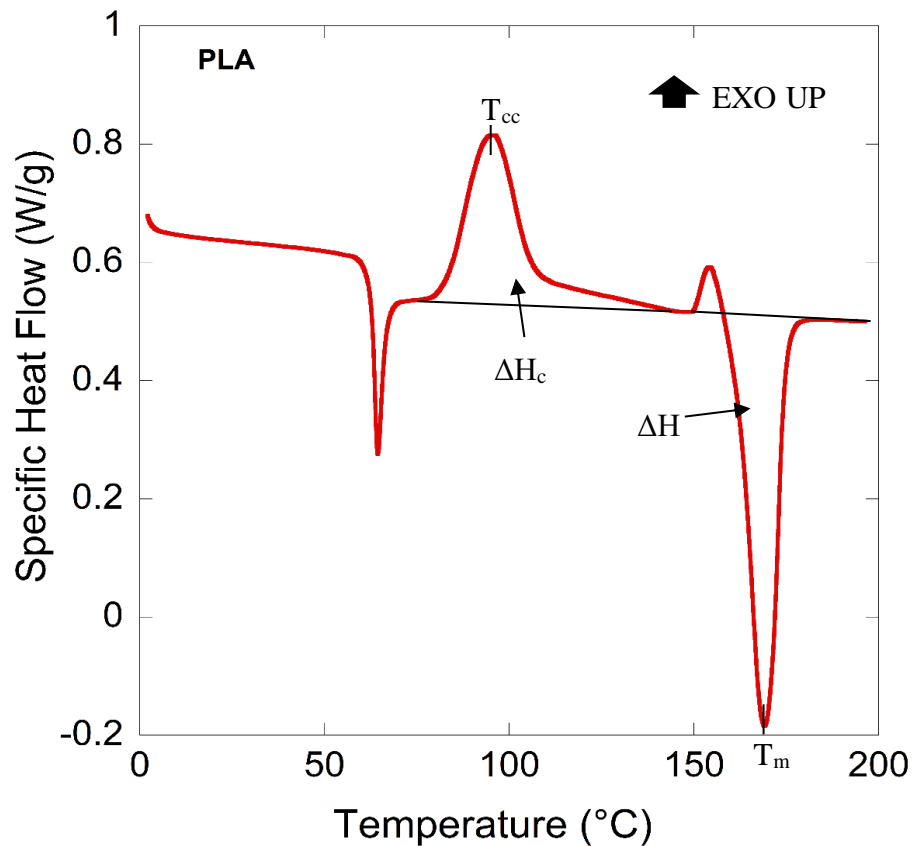


Figure B. 2 DSC thermogram of PLA fibers showing the areas of integration for the enthalpies recorded in Table 3.1 and the positions for  $T_{cc}$  and  $T_m$ .

Table B. 1 Mechanical properties of mCNF-C12 composites.

As-Spun			Elastic Modulus	Strength at Failure
DR	%PEG	% mCNF-C12	GPa	MPa
0	0	0	1.4 +/- 0.1	55.0 +/- 1.0
0	5	0	1.2 +/- 0.3	42.0 +/- 0.26
0	5	0.05	1.5 +/- 0.6	59.3 +/- 3.0
0	5	0.3	1.6 +/- 0.3	67.0 +/- 23.0
0	5	0.6	2.2 +/- 0.2	60.0 +/- 3.0
0	5	1.3	4.8 +/- 1.2	30 +/- 5.0
Intended DR: 2X				
2	0	0	3.1 +/- 0.7	135.0 +/- 0.4
2	5	0	2.0 +/- 1.0	62.0 +/- 7.7
2	5	0.05	2.9 +/- 0.3	173.0 +/- 21.0
2	5	0.3	2.5 +/- 0.7	72.0 +/- 47.0
2	5	0.6	2.2 +/- 0.7	60.0 +/- 16.0
2	5	1.3	7.3 +/- 1.5	102.5 +/- 2.5
Intended DR: 3X				
3	0	0	2.8 +/- 0.1	232.0 +/- 18.5
3	5	0	2.0 +/- 0.3	58.0 +/- 3.0
3	5	0.05	2.8 +/- 0.02	167.0 +/- 18.5
3	5	0.3	3.8 +/- 0.7	166.0 +/- 27.0
3	5	0.6	3.9 +/- 2.0	56.0 +/- 9.0
3	5	1.3	7.8 +/- 3.0	120.0 +/- 5.0
Intended DR: 4X				
4	0	0	4.4 +/- 0.1	287.0 +/- 93.0
4	5	0	2.2 +/- 0.6	164.0 +/- 21.0
4	5	0.05	2.9 +/- 0.6	168.0 +/- 22.0
4	5	0.3	3.4 +/- 0.4	118.0 +/- 27.0
4	5	0.6	5.7 +/- 1.0	77.0 +/- 30.0
4	5	1.3	7.8 +/- 0.5	110.0 +/- 15.0
Intended DR: 5X				
5	0	0	-	-
5	5	0	2.7 +/- 0.03	160.0 +/- 63.0
5	5	0.05	2.6 +/- 0.5	120.0 +/- 20.0
5	5	0.3	4.1 +/- 1.5	211.0 +/- 72.0
5	5	0.6	4.9 +/- 3.6	60.0 +/- 14.0
5	5	1.3	6.7 +/- 0.3	145.0 +/- 18.0
Intended DR: 6X				
4	0	0	-	-
6	5	0	3.0 +/- 0.6	230.0 +/- 1.0
6	5	0.05	4.3 +/- 1.2	138.8 +/- 46.0
6	5	0.3	5.3 +/- 0.7	272.0 +/- 18.0
6	5	0.6	7.1 +/- 0.5	196.0 +/- 53.0
6	5	1.3	10.5 +/- 0.8	236.0 +/- 5.0

## APPENDIX C: POLYLACTIC ACID NANOCOMPOSITES

Hoffman-Weeks Nonlinear Extrapolation: Original code written by Sami M. El Awad Azrak

**%THIS IS THE 5 GUESS VERSION of the Hoffman-Weeks Extrapolation**

Tm\_guess = 165:0.2:250;

Tm\_exp = [152.3 155 155.1 157.4 158.3];

Tc\_exp = [100 110 115 120 130];

n = length(Tm\_exp);

M = cell(n,1); %empty second cell array

X = cell(n,1); %empty second cell array

k = 1; %start counter for cell

%to get cell array with M

while k <= length(Tm\_exp)

    m = zeros(1,length(Tm\_guess));

    for i = 1:length(Tm\_guess)

        m(i)= Tm\_guess(i)/(Tm\_guess(i)-Tm\_exp(k));

    end

    M{k} = m;

    k = k + 1;

end

%reset counter for array

k = 1;

%second cell array with X

%the cell array contains in the first cell the all the values for the

%Tm\_guesses from start to finish with the first Tc\_exp

while k <= length(Tc\_exp)

    x = zeros(1,length(Tm\_guess));

    for i = 1:length(Tm\_guess)

        x(i)= Tm\_guess(i)/(Tm\_guess(i)-Tc\_exp(k));

    end

    X{k} = x;

    k = k + 1;

end

%Getting the x and y points to perform the linear regression (only works

%for 5 Tm\_exp and Tc\_exp values

pt\_x = zeros(5,length(Tm\_guess));

pt\_y = zeros(5,length(Tm\_guess));

for i = 1:length(Tm\_guess)

%x point column vector (Tc)

pt\_x(:,i) = [X{1,1}(i); X{2,1}(i); X{3,1}(i); X{4,1}(i); X{5,1}(i)];

```

%y point column vector (Tm)
pt_y(:,i) = [M{1,1}(i); M{2,1}(i); M{3,1}(i); M{4,1}(i); M{5,1}(i)];
end

%plot of M vs. X
scatter(pt_x(:,1),pt_y(:,1));
title('M vs. X plot for the first guess of Tm (190C)')
xlabel('X')
ylabel('M')

%performing linear regression to obtain a slope and intercept
lin_reg = zeros(2,length(Tm_guess));
[mm,nn] = size(pt_x); %getting the size of the pt_x matrix to create the XX matrix
for i = 1: length(Tm_guess)
XX = [ones(mm,1) pt_x(:,i)]; %this is the vector with a column full of ones and a column full of
the pt_x(:,i) values
lin_reg(:,i) = XX\pt_y(:,i); %this solves the equation Y = XB where Y is the column vector
containing the intercept and the slope
end

%Extracting only the slope values to be used during plotting
slope = lin_reg(2,:);

% THIS IS THE CORRECT WAY OF SOLVING FOR THE FITTED TM_FITTED
i = 1; %reset counter
k = 1; %reset counter
% solving for [gamma*X+intercept], it is organized so that the
% first column of the matrix is the values for the first guessed Tm_guess
right_side = zeros(length(Tm_exp),length(Tm_guess));
while k <= length(Tm_exp)
    for i = 1:length(Tm_guess)
        right_side(k,i)=lin_reg(2,i)*X{k,1}(i)+lin_reg(1,i);
    end
    k = k+1;
end

%Calculating the fitted experimental melting point
%Tm_predicted is a column vector where the values correspond to the
%Tm_guess starting form the first Tc_guess to the last and then switching to the next
% column which corresponds to the next Tm_guess
iii = 1; %new matrix element holder for Tm_predicted
Tm_fitted = zeros(length(Tm_guess)*3,1);
for i = 1: length(Tm_guess)
    for ii = 1:length(Tm_exp)
        Tm_fitted(iii,:) = Tm_guess(i)-(Tm_guess(i)/right_side(iii));
        iii = iii + 1;
    end
end

```

```

    end
end

%Solving for the squared difference between Tm_exp and Tm_fitted for a specific
%Tm_guess, each column in the difference matrix is for a specific Tm_guess
ii = 1; %reset counter
k = 1; %reset counter
sqr_difference = zeros(length(Tm_exp), length(Tm_guess));
while ii <= length(Tm_fitted)
    for i = 1: length(Tm_exp)
        sqr_difference (i,k) = (Tm_fitted(ii)-Tm_exp(i))^2;
        ii = ii + 1;
    end
    k = k + 1;
    if ii > length(Tm_fitted);
        break
    end
end

%calculating the sum of the squares from the sqr_difference matrix (i.e.
%the final variance S_sqr
S_sqr = sum(sqr_difference);

%Plotting the slope and the S^2 values vs. the Tm_guesses
figure % new figure
[hAx,hLine1,hLine2] = plotyy(Tm_guess, slope, Tm_guess, S_sqr);
title('PLA with Tm guesses from 190C to 210C')
xlabel('Tm-guess [C]')
ylabel(hAx(1),'Slope [gamma]') % left y-axis
ylabel(hAx(2),'S^2') % right y-axis

```

▲ EXO UP

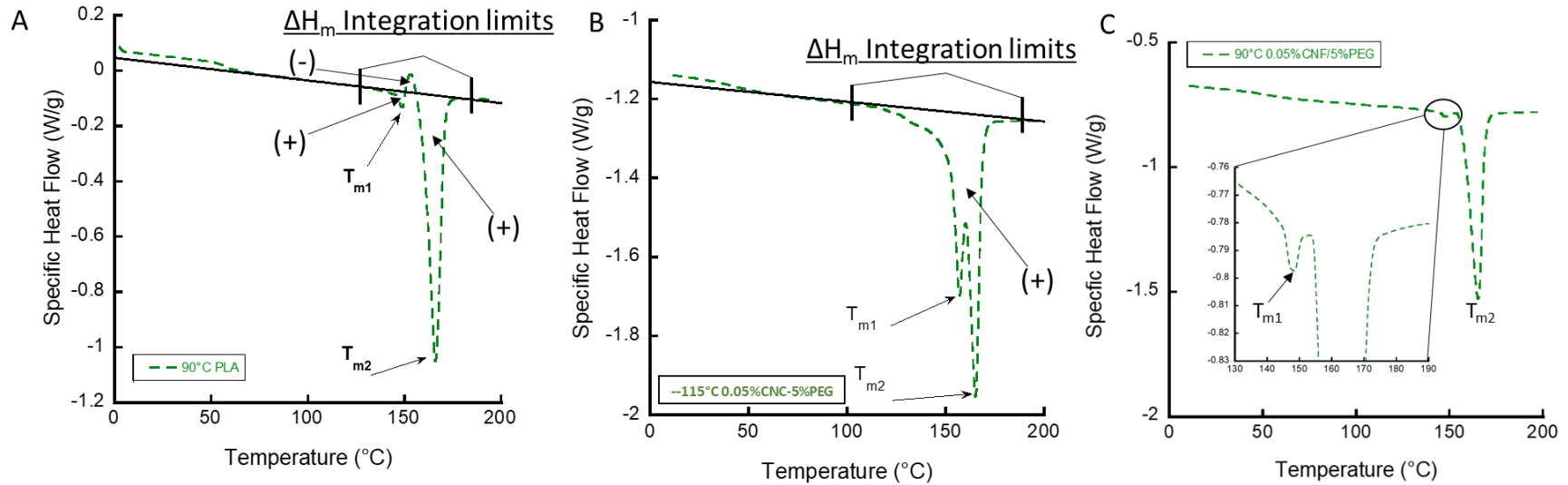
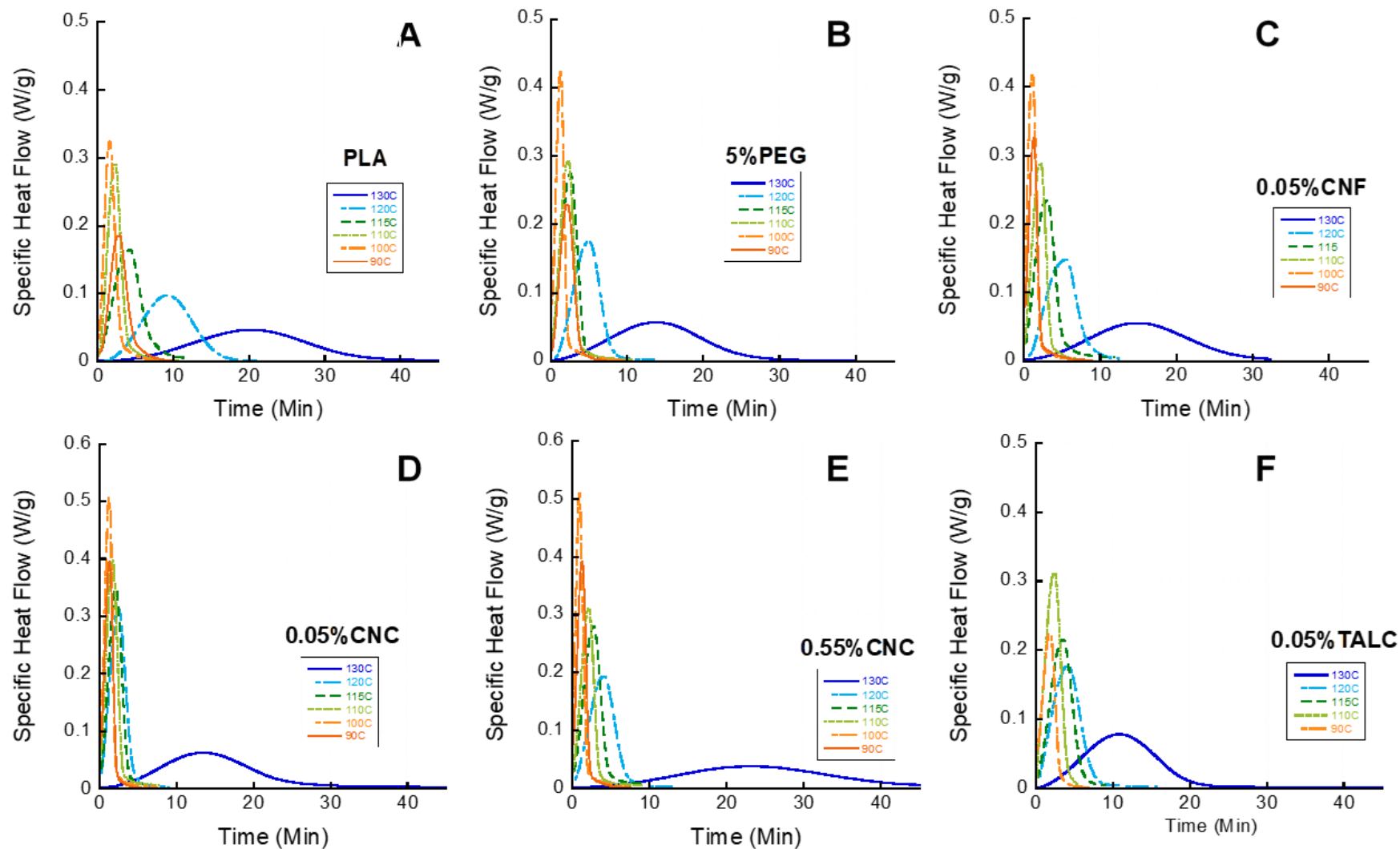


Figure C. 1 Conventions used for three special cases that appeared in the data set. A) Integration of a melting peak in which the crystallization process during heating, but above the first melting peak; positive/endothermic (+) and negative/exothermic (-) contributions to the melting enthalpy are denoted. B) Very wide melting peak for integration are observed. C) The first melting peak is barely distinguishable but is still present.

↑ EXO UP



123

Figure C. 2 Isothermal runs from 90°C to 130°C showing the progression of the isotherm with isothermal temperature selection.

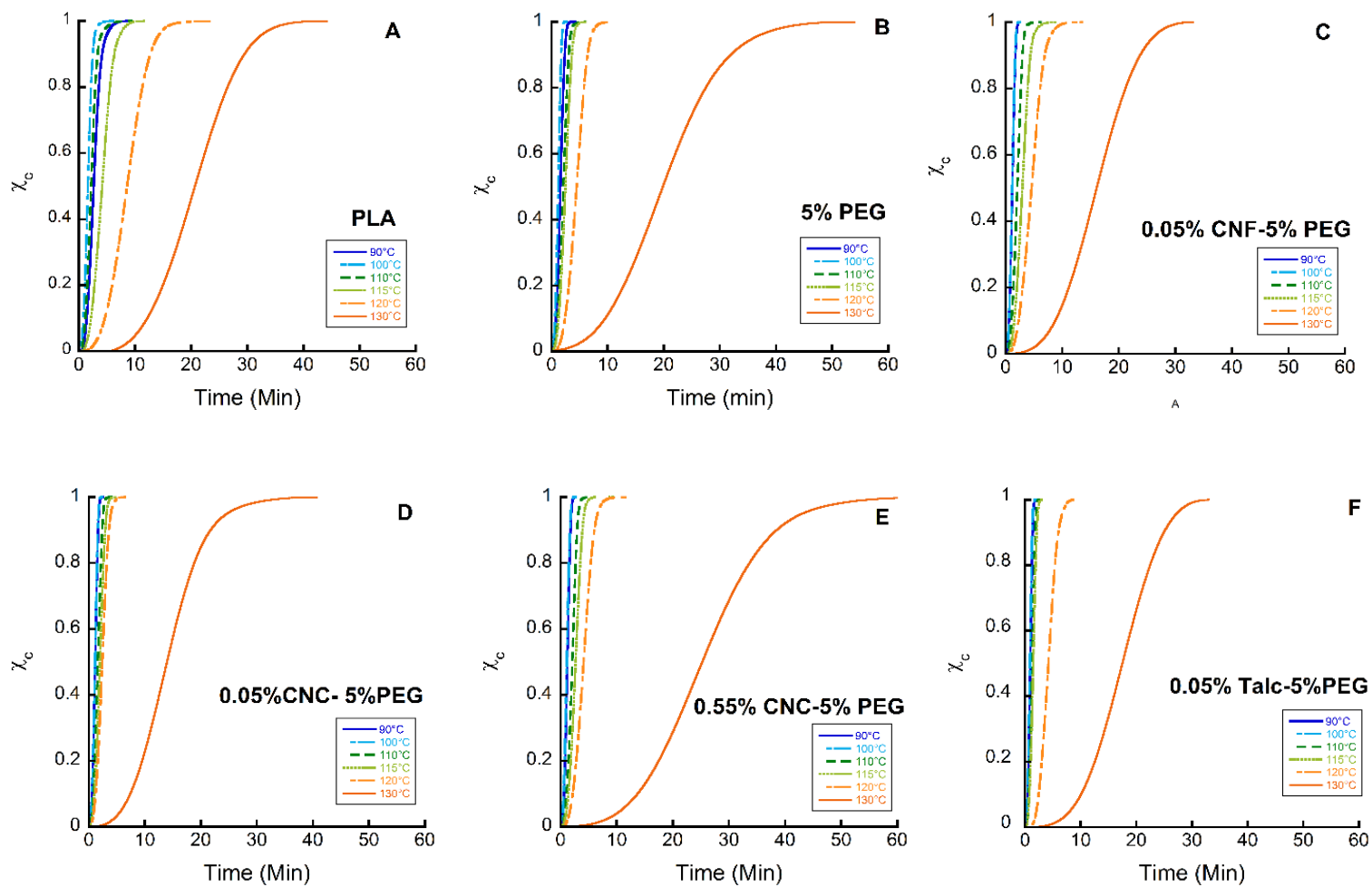


Figure C. 3 Relative crystallinity conversion,  $\chi_c$ , versus experiment time during isothermal experiments for A) PLA B) 5 wt% PEG C) 0.05 wt% CNF-5 wt% PEG, D) 0.05 wt% CNC-5 wt% PEG E) 0.55 wt% CNC-5 wt% PEG and F) 0.05 wt% Talc-5 wt% PEG.

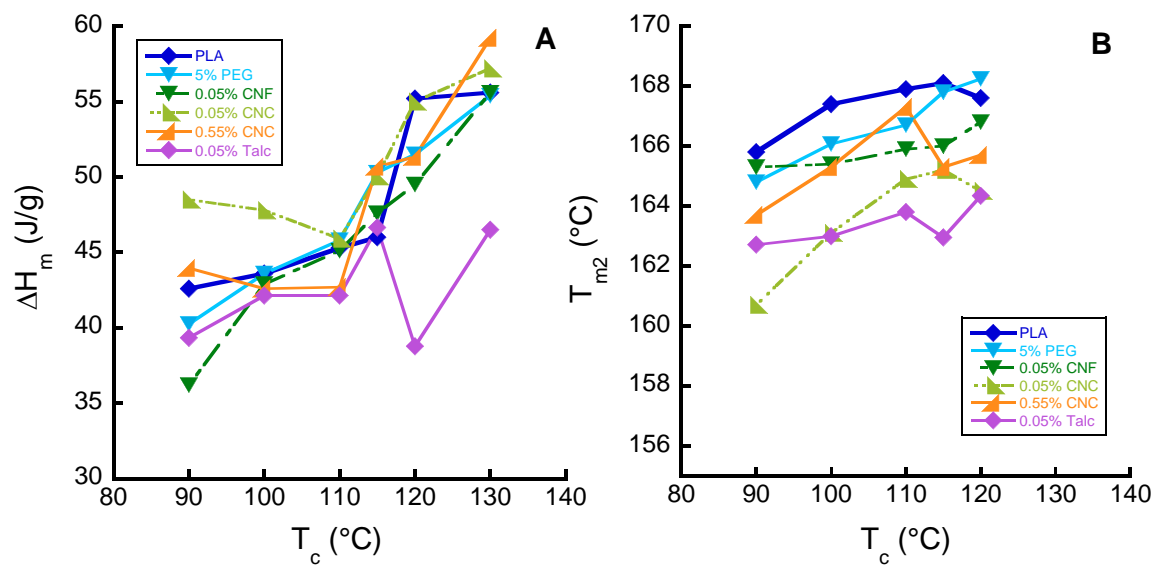


Figure C. 4 A) Melting enthalpy and B)  $T_{m2}$ , the second melting peak temperature, versus the crystallization temperature,  $T_c$ .

Table C. 1 Thermal properties measured upon reheating after isothermal crystallization.

Nanocellulose (wt%)	PEG (wt%)	T <sub>iso</sub> (°C)	H <sub>m</sub> (J/g)	T <sub>m1</sub> (°C)	T <sub>m2</sub> (°C)	X (%)
<b>Neat PLA</b>						
0	0	90	42.6	148.8	165.8	45.8
0	0	100	43.6	158.01	167.4	46.9
0	0	110	45.3	160.7	167.9	48.7
0	0	115	46.0	162.04	168.1	49.5
0	0	120	55.2	162.99	167.6	59.4
0	0	130	55.6	165.6	-	59.8
<b>PEG</b>						
0	5	90	40.25	147.3	164.8	45.6
0	5	100	43.6	156.3	166.07	49.3
0	5	110	45.81	158.8	166.7	51.9
0	5	115	50.3	160.3	167.8	56.9
0	5	120	51.5	162.12	168.24	58.3
0	5	130	55.4	163.5	-	62.7
<b>CNF/PEG</b>						
0.05	5	90	36.2	148.1	165.3	41.0
0.05	5	100	42.9	155.1	165.4	48.6
0.05	5	110	45.12	157.6	165.9	51.1
0.05	5	115	47.6	158.8	166.0	53.9
0.05	5	120	49.5	160.7	166.8	56.1
0.05	5	130	55.6	162.6	-	63.0
<b>CNC/PEG</b>						
0.05	5	90	48.5	146.4	160.7	54.9
0.05	5	100	47.8	153.8	163.1	54.1
0.05	5	110	45.90	156.2	164.9	52.0
0.05	5	115	50.04	157.1	165.2	56.7
0.05	5	120	55.0	158.0	164.5	62.3

0.05	5	130	57.2	161.0	-	64.8
0.55	5	90	43.96	146.4	163.7	50.0
0.55	5	100	42.6	154.6	165.3	48.5
0.55	5	110	42.7	158.8	167.3	48.6
0.55	5	115	50.69	157.5	165.3	57.7
0.55	5	120	51.34	159.2	165.7	58.4
0.55	5	130	59.22	162.4	-	67.4
<b>TALC</b>						
0.05	5	90	39.34	145.5	162.71	44.6
0.05	5	100	42.14	152.3	162.99	47.7
0.05	5	110	42.14	154.8	163.8	47.7
0.05	5	115	46.65	155.4	162.95	52.8
0.05	5	120	38.78	157.1	164.34	43.9
0.05	5	130	46.5	158.7	-	52.7

## APPENDIX D: POLYAMIDE NANOCOMPOSITES

Hansen solubility parameters (HSP) describe the solubility or dispersibility of a material using three basic contributions: London dispersion forces, polar (dipole-dipole), and hydrogen bonding called the HSP<sup>[135]</sup>. The basic principle is that “like dissolves like” or in this case, that “like disperses like.” All chemicals have a set of three parameters for dispersive, polar, and hydrogen bonding contributions, ( $\delta_D$ ;  $\delta_P$ ;  $\delta_H$ ), respectively, which correspond to the center of their solubility sphere in 3-dimensional HSP space. For particles with strong interactions, the distance between their HSP will be small. This distance is called Ra. The radius of the sphere,  $R_o$ , is useful for defining how alike two chemicals are and can be imagined as a cross-over point where chemical interactions go from good to bad or alike to not alike. For Ra less than  $R_o$ , the chemicals are very alike, while for larger differences they are not. Mixtures of chemicals can be approximated using a mixing rule of the chemical’s HSP. This is commonly observed for co-solvent systems<sup>[56]</sup>. Equation D. 1 is used to calculate the HSP for a mixed solvent where  $\Phi$  is the volume fraction of a number (n) of solvents for each parameter.

Equation D. 1

$$\delta_{(D,P,H),mix} = \sum_{i=1}^n \Phi_i \delta_{(D,P,H),i}$$

### Testing Nanoparticle Dispersion

It is typical to disperse dry nanoparticles or chemicals in the solvent for solubility and dispersion tests. However, the chemicals available for this study were in water. So, water-miscible co-solvent systems were selected for the analysis. Table D.1 contains a list of the water-miscible solvents initially selected for this study. To generate a large list of co-solvent systems for determining the HSP, multiple concentrations were selected for a few systems; the complete list of neat solvents (HSP, viscosity, and density at 25°C) and additional co-solvent volume ratios is shown in Table D.1. The HSP of co-solvent systems was calculated based on the volume percent of each solvent using Equation D. 1. For the 20%, 40%, 60%, and 80% water co-solvent systems, the HSP are reported in Table D. 1. For nanoparticle dispersion tests, 0.1 g in 10 mL solutions were prepared from water-based slurries by adding an amount equivalent to 0.1 g of CNC dry to

the container. For BGU<sup>2</sup> CNC, this resulted in 11.5 v% water in all co-solvent solutions and for FPL CNC, it was 8.6 v% as the initial concentration of water was different for each product. Since the water from the nanoparticle solution accounts for part of the 10 mL volume, the remaining part was one of the primary solvents listed in Table D. 1. All samples were vigorously mechanically mixed for 30 sec and then sonicated for 30 sec using a Branson Sonifyer. Samples could sit, undistributed, until the sedimentation time,  $t_{sed}$ , (Table D.1) had passed. The time for sedimentation was calculated using Equation D. 2. RST was  $1.18 \times 10^{11} \text{ s}^2\text{m}^{-2}$  and the viscosity and density values for solvents are reported in Table D.1. The  $\rho_{CNCs}$  was 1.5 g/cc for both types of CNC.

Equation D. 2

$$t_{sec} = RST \frac{\eta_{solvent}}{\rho_{CNCs} - \rho_{Solvent}}$$

After  $t_{sed}$  had passed samples were visually inspected and qualitatively ranked based on the formation of sediment. For small concentrations,  $t_{sed}$  was taken as the value of the pure solvent system reported in Table D. 1 since samples were graded in pairs after the  $t_{sed}$  had passed. For larger co-solvent volume ratios like those of ethanol, the  $t_{sed}$  of the denser solvent was used. For acetone and ethanol mixtures, that was water, so samples were graded after 48 hrs. The visual criteria used by Bruel *et al.* was adopted for this analysis were clear/transparent with no sediment is a 2, murky/turbid is a 1, and opaque, white sediment with phase separation such that text could be read through the top of the vial is a 0, such as in Figure D. 1 A<sup>[56]</sup>.

After grading all solvent tests on a 0 to 2 scale visually, the data was input into a Matlab algorithm for determining the HSP and radius,  $R_o$  published by Gharagheizi <sup>[136]</sup>. While there is an HSP software called HSPiP equipped with a database of chemicals it was not used for this study as it was not available. Instead, HSP of chemicals and solvents were found from the literature as well as the Hansen Solubility Parameters Handbook written by Charles M. Hansen which tabulates a large number of chemicals (both modeled and measured cohesion parameters) <sup>[135]</sup>. The plots prepared in this section were made in Origin.

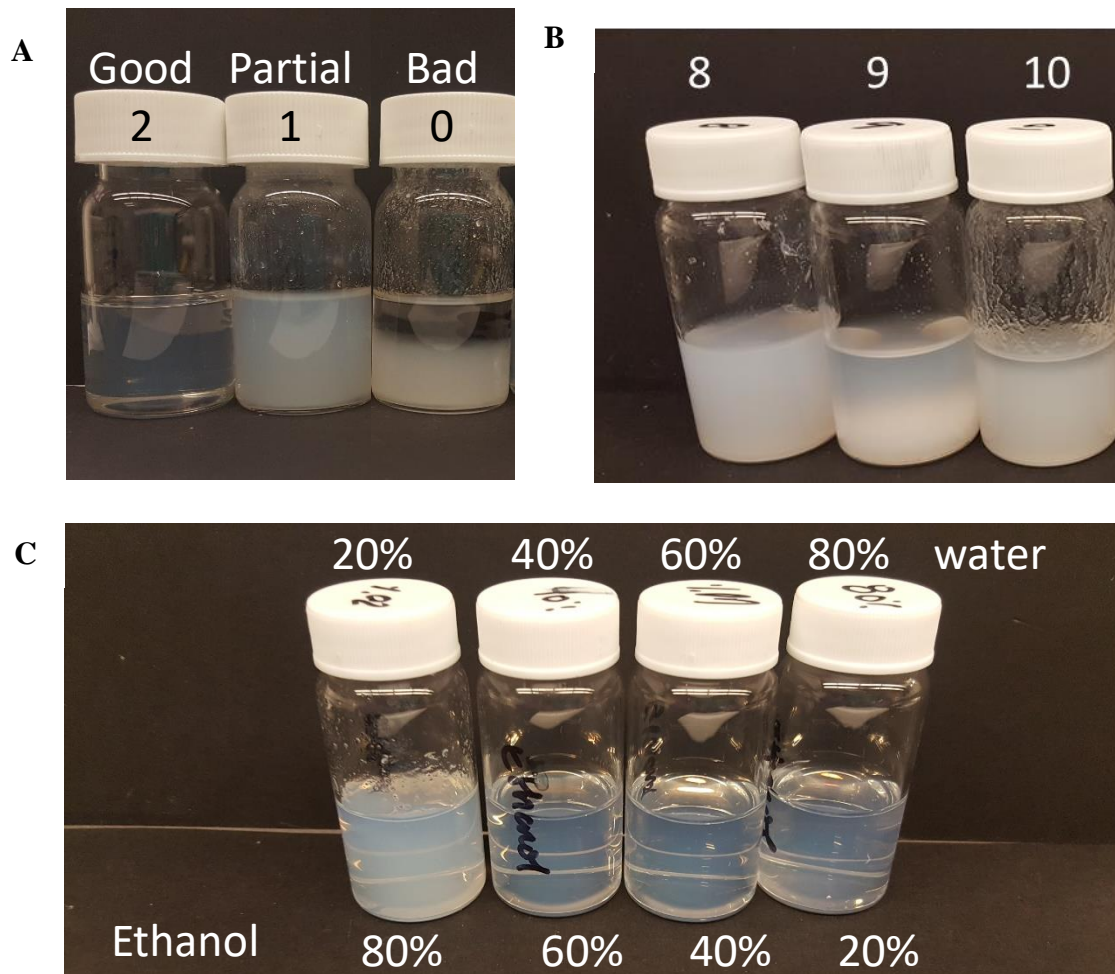


Figure D. 1 A) Examples of good/partial/bad dispersion in three solvents for BGU2. CNC B) Example of mixed solvent systems at various composites for FPL CNC.

Table D. 1 Master solvent list with HSP, solvent properties, and sedimentation time.

Solvent Number	Solvent	$\delta_D$ (MPa <sup>1/2</sup> )	$\delta_D$ (MPa <sup>1/2</sup> )	$\delta_H$ (MPa <sup>1/2</sup> )	Solv. Viscosity (mPa-sec)	Solv. Density (g/cm <sup>3</sup> )	Sed. Time (hr)
1	H2O	15.1	20.4	16.5	0.891	0.997	48.43
2	Formamide	17.2	26.2	19	3.29	1.13	229.44
3	Ethylene Glycol	17	11	26	17.2	1.11	1150.57
4	Ethanolamine	17.2	15.6	21.3	18.9	1.01	1050.00
5	Propylene Glycol	16.8	9.4	23.3	42	1.04	2458.33
6	Methanol	15.1	12.3	22.3	0.547	0.787	22.05
7	Dimethyl Sulfoxide	18.4	16.4	10.2	1.99	1.1	130.46
8	Ethanol	15.8	8.8	19.4	1.09	0.785	43.84
9	Acetonitrile	15.3	18	6.1	0.441	0.786	17.76
10	2-Propanol	15.8	6.1	16.4	2.04	0.781	81.64
11	1-Butanol	16	5.7	15.8	1.1	0.81	0.00
12	Dimethyl Acetamide	16.8	11.5	10.2	0.945	0.94	46.93
13	Acetophenone	19.6	8.6	3.7	1.68	1.03	0.00
14	Dimethylformamide	17.4	13.7	11.3	0.801	0.945	40.08
15	Pyridine	19	8.8	5.9	0.88	0.982	46.67
16	Acetone	15.5	10.4	7	0.302	0.785	12.15
17	Tetrahydrofuran	16.8	5.7	8	0.461	0.877	20.90
18	Methyl Ethyl Ketone	16	9	5.1	0.386	0.8	15.82
A	Water/Acetone						
1	80/20	15.24	18.08	17.08	-	-	48.43
2	60/40	15.38	15.76	17.66	-	-	-
3	40/60	15.52	13.44	18.24	-	-	-
4	20/80	15.66	11.12	18.82	-	-	-
B	Water/Ethanol						-
1	80/20	20	15.26	17.80	-	-	48.43
2	60/40	40	15.42	15.20	-	-	-
3	40/60	60	15.58	12.59	-	-	-
4	20/80	80	15.74	9.99	-	-	-

## Hansen Solubility Parameters for Nanoparticles

HSP was estimated for two types of CNCs using a hybrid, water-miscible method which accounts for the water content added to the solution by using wet or never-dried CNCs. The potential solvents for the method are provided in Table D.1. Of the 26 potential solvents in the master list, only 21 were selected. Polypropylene glycol, ethylene glycol, and ethanolamine were eliminated since  $t_{\text{sed}}$  for these materials was over 1000hrs (40 days). Pyridine was eliminated since it can react with water and dimethylacetamide was eliminated due to availability in the lab. The RST of  $1.18 \times 10^{11} \text{s}^2 \text{m}^{-2}$  was selected based on Bruel *et al.*'s method<sup>[56]</sup>. They determined the solubility sphere and cohesion parameters for a sulfuric acid CNC purchased from Celluforce, a commercial nanocellulose producer from Quebec, Canada.

Solubility spheres for BGU<sup>2</sup> CNC and FPL CNC are shown in Figure D. 2. For the BGU<sup>2</sup> CNC (Figure D. 2 A), the sphere appears as expected where the “good co-solvents,” solvents graded with a 2 are inside the sphere. However, one “other” solvent is located inside the sphere for BGU<sup>2</sup> CNC. This solvent is a partial (1) grade of ethanol and water and is located on the edge of the sphere closest to pure ethanol. The ethanol/water ratio experiments are denoted by an arrow in Figure D. 2 where the arrowhead points towards ethanol. Likewise, the HSP sphere of FPL CNCs is shown in Figure D. 2B. This sphere shows several discrepancies compared to the BGU<sup>2</sup> CNC. Solvents like ethanol, the 20% water/80% acetone, and the acetonitrile, which were graded as 1 or 0 are also inside the sphere. These discrepancies may come from the fact that there is some subjectivity in grading dispersion by eye and that a partial “1” may describe any of the co-solvent mixtures shown in Figure D. 1B, which could be arguably different. Errors may also arise from using model cohesion parameters rather than experimentally determined parameters. 2D projections of the HSP axes are shown in Figure D. 3, Figure D. 4, Figure D. 5.

The HSP ( $\delta_D$ ;  $\delta_P$ ;  $\delta_H$ ) tabulated from the water-miscible method were: (17.6; 18.9; 16.7) MPa<sup>1/2</sup> and (18.4; 16.84; 15.9) MPa<sup>1/2</sup>, for BGU<sup>2</sup> CNC and FPL CNC, respectively. The  $R_o$  was 8.8 MPa<sup>1/2</sup> and 9.8 MPa<sup>1/2</sup> for BGU<sup>2</sup> CNC and FPL CNC, respectively. These values are comparable to the polar sphere reported by Bruel *et al.* for sulfuric acid CNCs which were ( $\delta_D$ : 18.1 $\pm$ 0.5;  $\delta_P$ : 20.4 $\pm$ 0.5;  $\delta_H$ : 15.3  $\pm$ 0.4) MPa<sup>1/2</sup> with a  $R_o$  of 7.8 MPa<sup>1/2</sup> [56]. Determination of HSP was sensitive to how the test was graded on a scale of 0 to 2 and HSP and  $R_o$  could fluctuate a lot depending on the number of solvents and their grade. Care was taken to test as many possible different solvents in this case, but additional mixed co-solvent systems using what was available

(like ethanol or acetone) were a necessity to improve HSP determination using the code developed and published by Gharagheizi.<sup>[136]</sup> Furthermore, since all experiments were water-based, only the polar sphere of the CNCs could be determined. There are two HSP spheres; one polar and one non-polar sphere<sup>[56]</sup>. For our purposes, we care that known good solvents like dimethyl sulfoxide and water are inside the sphere as these experiments were originally designed to identify co-solvent systems for blending CNMs with additives as well as choosing potential additives.

From Figure D. 4, it is evident that only a few chemicals are within the solubility sphere of either CNC. Those are PVOH and benzenesulfonamide for BGU<sup>2</sup> CNC and FPL CNC. FPL CNC also has ethylene vinyl alcohol (EVOH) inside the sphere but considering potential errors associated with the FPL sphere, it may not be.

Table D. 2 HSP of various additives and polymers.

<b>ID</b>	<b>Material</b>	<b><math>\delta_D</math> (MPa<sup>1/2</sup>)</b>	<b><math>\delta_P</math> (MPa<sup>1/2</sup>)</b>	<b><math>\delta_H</math> (MPa<sup>1/2</sup>)</b>	<b>Reference</b>
1	Benzene Sulfonamide	20	19.5	10.7	[56]
3	E4HB	17.9	6.2	6	[135]
4	M4HB	17	8.2	4.7	[135]
5	Dibutyl Phthalate	8.2	4.2	2.0	[135]
6	Triethyl citrate	16.5	4.9	12	
7	Imwitor 900 mono	16.8	1.8	11.25	[137]
8	Capmul MCM C8 Mono	17.06	3.3	15.05	[137]
9	Capmul MCM C10 Mono	16.98	2.85	13.98	[137]
5	Dibutyl Phthalate	17.8	9.6	4.5	[138]
PE	Polyethylene	15.9	0.8	2.8	[56]
PLA	Poly(lactic acid)	18.5	8	7	[56]
PEG	Poly(ethylene glycol)	17	10	5	[56]
PVOH	Poly(vinyl alcohol)	15	17.2	17.8	[56]
EVOH	Ethylene(vinyl alcohol)	20.5	10.5	12.3	[138]
Ny6	Nylon 6	17	3.4	10.6	[139]
Ny6,6	Nylon 6,6	5.1	18.2	13.7	[140]

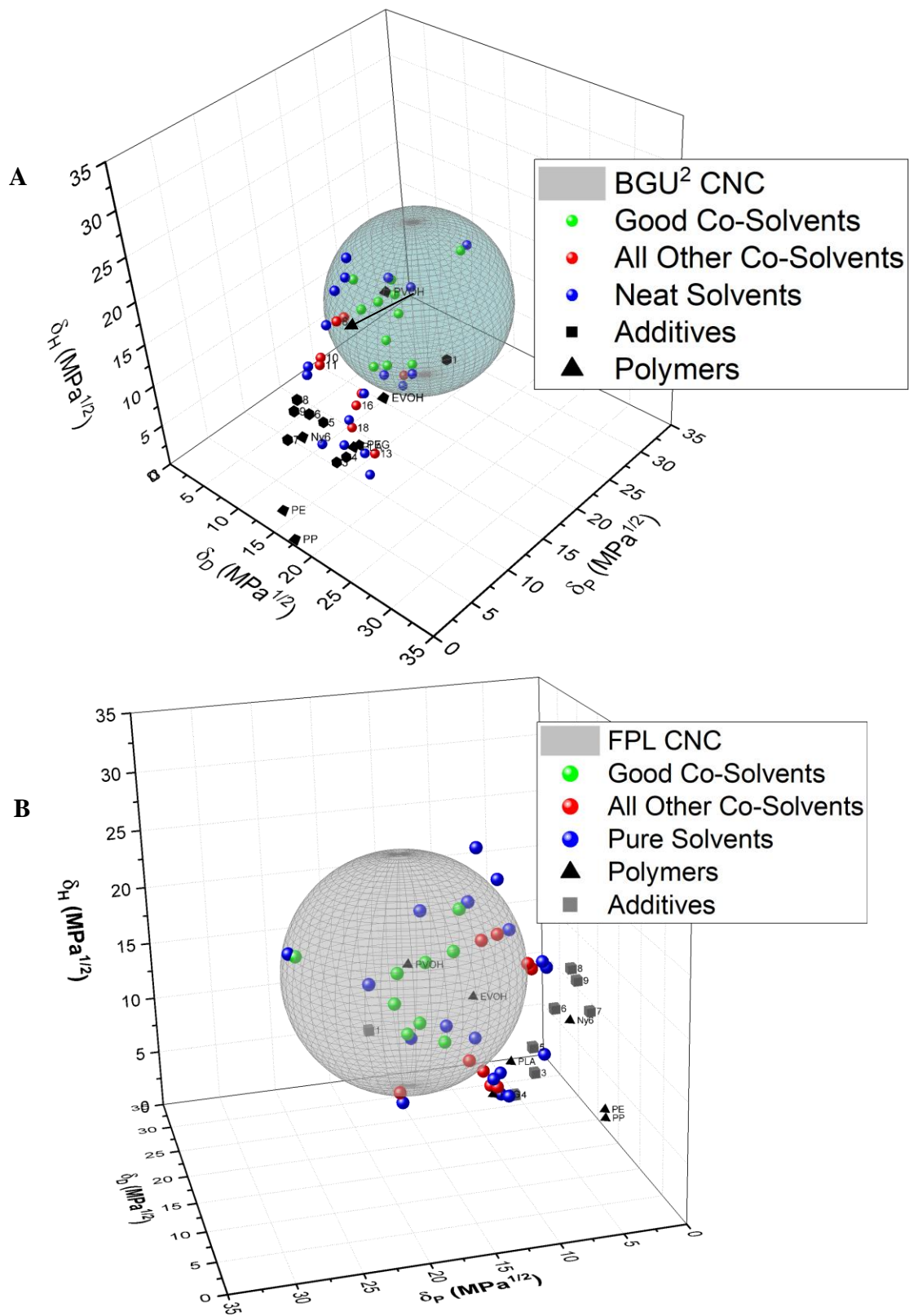


Figure D. 2 HSP sphere of A) BGU2 CNC and B) FPL CNC with labeled points for polymers and additives.

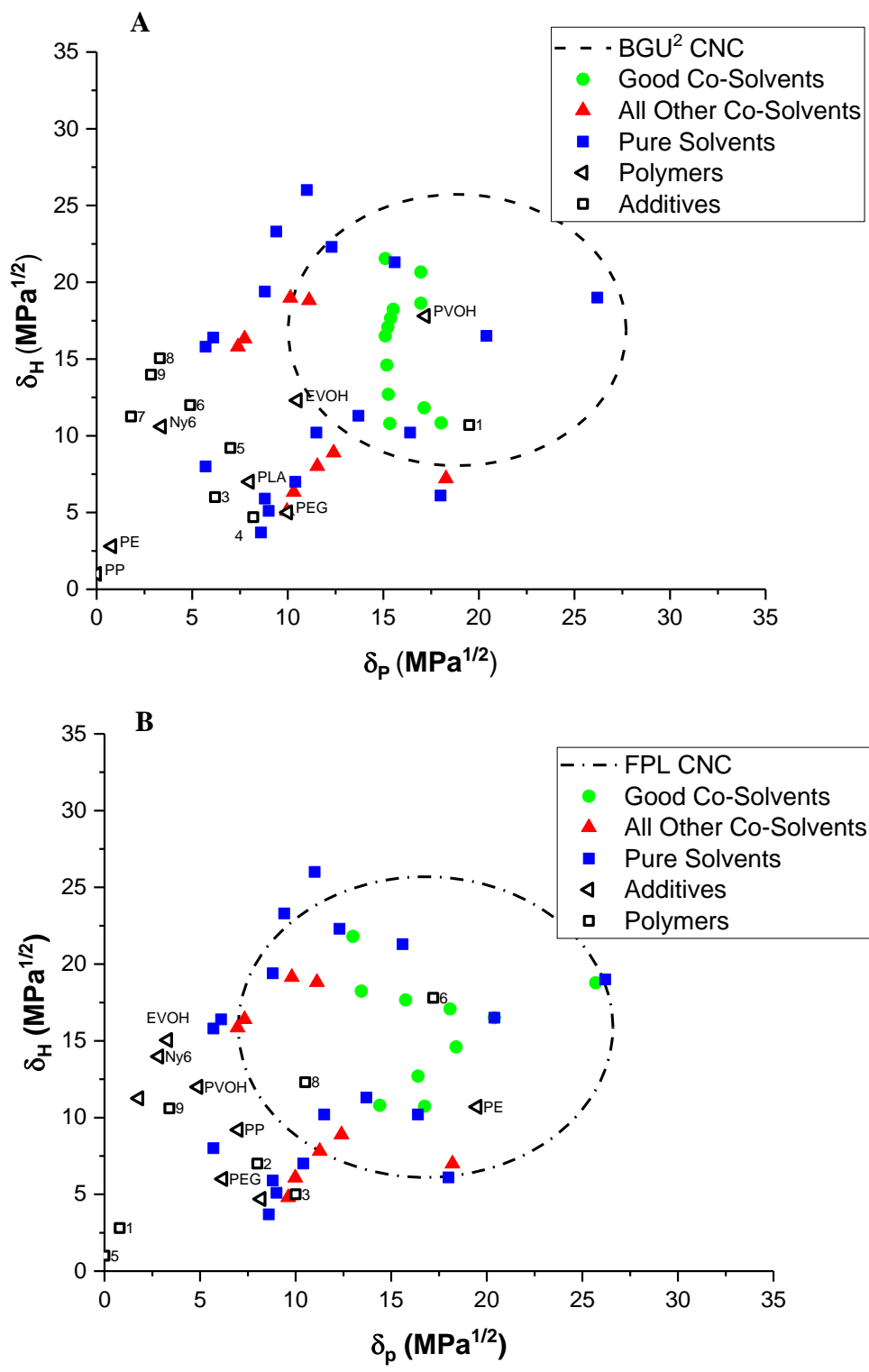


Figure D. 3 HSP hydrogen bonding contribution versus polar contribution for A) BGU2 CNC and B) FPL CNC.

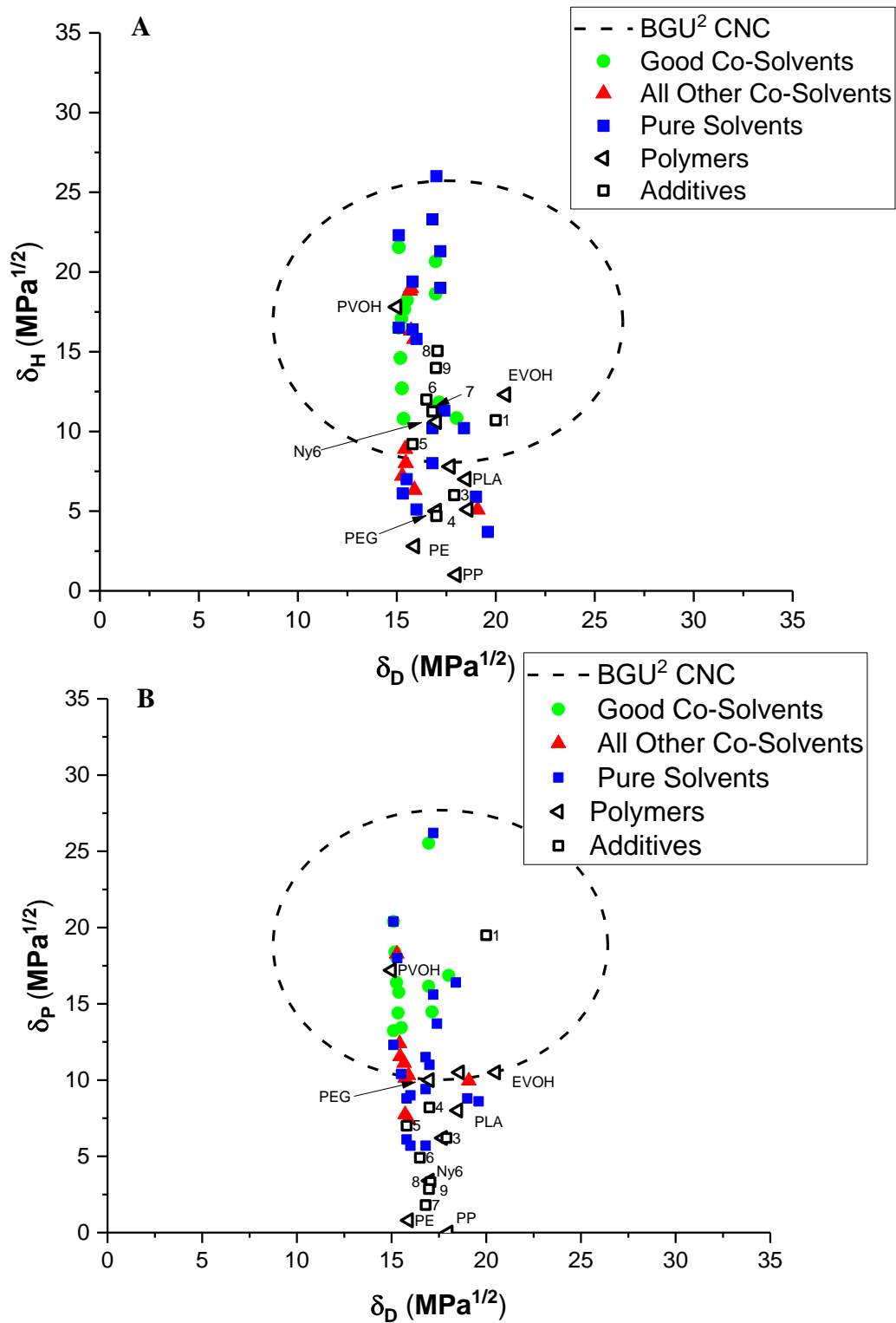


Figure D. 4 Projections of the HSP for BGU2 CNC: A) Hydrogen bonding parameter versus dispersive, and B) Polar versus dispersive.

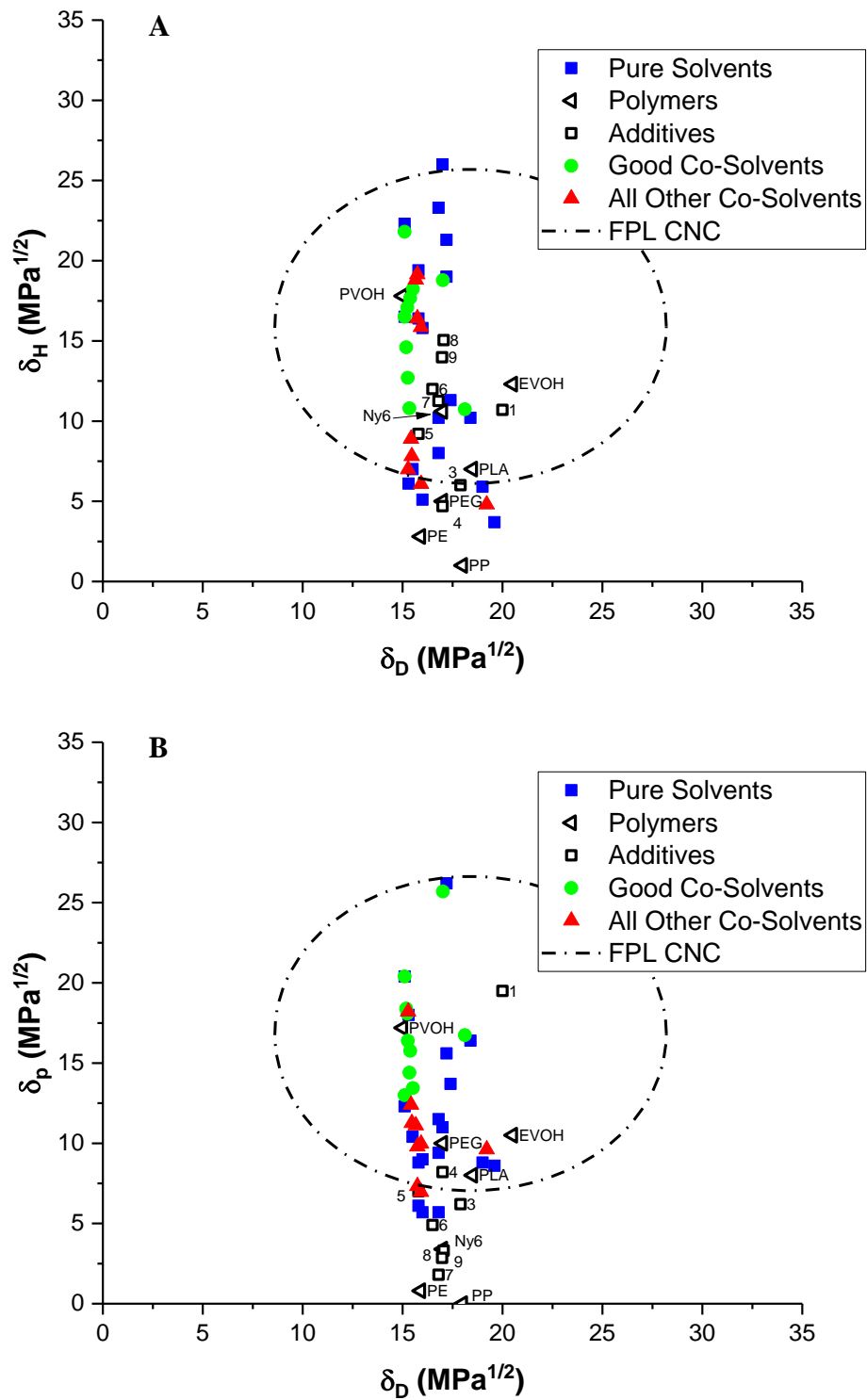


Figure D. 5 HSP for FPL CNC: A) hydrogen bonding parameter versus dispersive and B) Polar versus Dispersive.

## REFERENCES

- [1] R. J. Moon, G. T. Schueneman, J. Simonsen, *JOM* **2016**, *68*, 2383.
- [2] R. J. Moon, A. Martini, J. Nairn, J. Simonsen, J. Youngblood, *Chem. Soc. Rev.* **2011**, *40*, 3941.
- [3] J. A. Diaz, Z. Ye, X. Wu, A. L. Moore, R. J. Moon, A. Martini, D. J. Boday, J. P. Youngblood, *Biomacromolecules* **2014**, *15*, 4096.
- [4] J. A. Diaz, X. Wu, A. Martini, J. P. Youngblood, R. J. Moon, *Biomacromolecules* **2013**, *14*, 2900.
- [5] R. A. Chowdhury, M. Nuruddin, C. Clarkson, F. Montes, J. Howarter, P. J. Youngblood, *ACS Appl. Mater. Interfaces* **2019**, 1376.
- [6] C. M. Clarkson, S. M. El Awad Azrak, R. Chowdhury, S. N. Shuvo, J. Snyder, G. Schueneman, V. Ortalan, J. P. Youngblood, *ACS Appl. Polym. Mater.* **2019**, *1*, 166.
- [7] P. Venkatraman, A. M. Gohn, A. M. Rhoades, E. J. Foster, *Compos. Part B Eng.* **2019**, *174*, 106988.
- [8] A. Nicharat, J. Sapkota, C. Weder, E. Johan Foster, *J. Appl. Polym. Sci.* **2015**, *132*, 1.
- [9] D. Trache, M. H. Hussin, M. K. M. Haafiz, V. K. Thakur, *Nanoscale* **2017**, *9*, 1763.
- [10] S. Shrestha, J. A. Diaz, S. Ghanbari, J. P. Youngblood, *Biomacromolecules* **2017**, *18*, 1482.
- [11] H. Ritchie, M. Roser, "Plastic Pollution," can be found under <https://ourworldindata.org/plastic-pollution>, **2020**.
- [12] K. Sahoo, R. Bergman, S. Alanya-Rosenbaum, H. Gu, S. Liang, *Sustain.* **2019**, *11*, 1.
- [13] R. Arvidsson, D. Nguyen, M. Svanström, *Environ. Sci. Technol.* **2015**, *49*, 6881.
- [14] H. Gu, R. Reiner, R. Bergman, A. Rudie, *LCA XV Pap. Proc. – A "Bright" Green Future* **2015**, 33.
- [15] E. T. H. Vink, S. Davies, *Ind. Biotechnol.* **2015**, *11*, 167.
- [16] D. Posen, P. Jaramillo, A. E. Landis, M. W. Griffin, *Environ. Res. Lett.* **2017**, *12*, 034024.
- [17] M. Hervy, S. Evangelisti, P. Lettieri, K. Y. Lee, *Compos. Sci. Technol.* **2015**, *118*, 154.
- [18] **2019**.

- [19] R. A. Chowdhury, A. Rai, E. Glynn, P. Morgan, A. L. Moore, J. P. Youngblood, *Polymer* **2019**, *164*, 17.
- [20] S. Shrestha, F. Montes, G. T. Schueneman, J. F. Snyder, J. P. Youngblood, *Compos. Sci. Technol.* **2018**, *167*, 482.
- [21] N. Herrera, A. P. Mathew, K. Oksman, *Compos. Sci. Technol.* **2015**, *106*, 149.
- [22] T. Hees, F. Zhong, T. Rudolph, A. Walther, R. Mülhaupt, *Adv. Funct. Mater.* **2017**, *27*, 1.
- [23] K. D. Hendren, T. W. Baughman, P. A. Deck, E. J. Foster, *J. Appl. Polym. Sci.* **2019**, *48500*, 1.
- [24] N. Herrera, H. Roch, A. M. Salaberria, M. A. Pino-Orellana, J. Labidi, S. C. M. Fernandes, D. Radic, A. Leiva, K. Oksman, *Mater. Des.* **2016**, *92*, 846.
- [25] A. A. Singh, J. Wei, N. Herrera, S. Geng, K. Oksman, *Compos. Sci. Technol.* **2018**, *162*, 140.
- [26] C. M. Clarkson, G. Schueneman, J. Snyder, J. P. Youngblood, *Green Mater.* **2018**, *6*, 6.
- [27] S. Geng, K. Yao, Q. Zhou, K. Oksman, *Biomacromolecules* **2018**, *19*, 4075.
- [28] Y. Yoo, J. P. Youngblood, *ACS Sustain. Chem. Eng.* **2016**, *4*, 3927.
- [29] S. X. Peng, S. Shrestha, Y. Yoo, J. P. Youngblood, *Polym. (United Kingdom)* **2017**, *112*, 359.
- [30] S. Shrestha, R. A. Chowdhury, M. D. Toomey, D. Betancourt, F. Montes, J. P. Youngblood, *Cellulose* **2019**, *26*, 9631.
- [31] A. Gupta, W. Simmons, G. T. Schueneman, E. A. Mintz, *J. Therm. Anal. Calorim.* **2016**, *126*, 1243.
- [32] A. Gupta, W. Simmons, G. T. Schueneman, D. Hylton, E. A. Mintz, *ACS Sustain. Chem. Eng.* **2017**, *5*, 1711.
- [33] S. Chen, G. Schueneman, R. B. Pipes, J. Youngblood, R. J. Moon, *Biomacromolecules* **2014**, *15*, 3827.
- [34] C. M. Clarkson, G. T. Schueneman, J. F. Snyder, J. P. Youngblood, *Green Mater.* **2018**, *6*, 6.
- [35] A. J. Uddin, J. Araki, Y. Gotoh, *Biomacromolecules* **2011**, *12*, 617.
- [36] E. E. Ureña-Benavides, C. L. Kitchens, *Mol. Cryst. Liq. Cryst.* **2012**, *556*, 275.
- [37] R. Endo, T. Saito, A. Isogai, *Polym. (United Kingdom)* **2013**, *54*, 935.

- [38] S. Gogolewski, A. J. Pennings, *J. Appl. Polym. Sci.* **1983**, 28, 1045.
- [39] J. W. Leenslag, A. J. Pennings, *Polymer*. **1987**, 28, 1695.
- [40] V. Horacek, I., Kalisek, *J. Appl. Polym. Sci.* **1994**, 54, 1751.
- [41] A. R. Postema, A. H. Luiten, A. J. Pennings, *J. Appl. Polym. Sci.* **1990**, 39, 1265.
- [42] I. Horacek, Kalisek, *J. Appl. Polym. Sci.* **1994**, 54, 1759.
- [43] E. M. Sullivan, R. J. Moon, K. Kalaitzidou, *Materials (Basel)*. **2015**, 8, 8106.
- [44] P. K. Ilankeeran, P. M. Mohite, S. Kamle, *Mod. Mech. Eng.* **2012**, 02, 151.
- [45] R. G. Larson, *Rheol. Acta* **1992**, 31, 213.
- [46] K. B. Migler, Y. Son, F. Qiao, K. Flynn, *J. Rheol. (N. Y. N. Y.)*. **2002**, 46, 383.
- [47] E. Miller, J. P. Rothstein, *Rheol. Acta* **2004**, 44, 160.
- [48] M. Yasuniwa, S. Tsubakihara, Y. Sugimoto, C. Nakafuku, *J. Polym. Sci. Part B Polym. Phys.* **2004**, 42, 25.
- [49] H. Li, M. A. Huneault, *Polymer*. **2007**, 48, 6855.
- [50] Y. Habibi, S. Aouadi, J. M. Raquez, P. Dubois, *Cellulose* **2013**, 20, 2877.
- [51] S. X. Peng, R. J. Moon, J. P. Youngblood, *Green Mater.* **2014**, 2, 193.
- [52] B. Gupta, N. Revagade, J. Hilborn, *Prog. Polym. Sci.* **2007**, 32, 455.
- [53] E. E. Urena-Benavides, P. J. Brown, C. L. Kitchens, *Langmuir* **2010**, 26, 14263.
- [54] J. Williams, *Fracture Mechanics of Polymers*, Horwood, **1984**.
- [55] K. L. Chawla, *Composite Materials*, **2012**.
- [56] C. Bruel, J. R. Tavares, P. J. Carreau, M. C. Heuzey, *Carbohydr. Polym.* **2019**, 205, 184.
- [57] E. J. Foster, R. J. Moon, U. P. Agarwal, M. J. Bortner, J. Bras, S. Camarero-Espinosa, K. J. Chan, M. J. D. Clift, E. D. Cranston, S. J. Eichhorn, D. M. Fox, W. Y. Hamad, L. Heux, B. Jean, M. Korey, W. Nieh, K. J. Ong, M. S. Reid, S. Renneckar, R. Roberts, J. A. Shatkin, J. Simonsen, K. Stinson-Bagby, N. Wanasekara, J. Youngblood, *Chem. Soc. Rev.* **2018**, 47, 2609.
- [58] C. M. Clarkson, S. M. El Awad Azrak, G. T. Schueneman, J. F. Snyder, J. P. Youngblood, *Polymer*. **2020**, 187, 122101.
- [59] Y. Yoo, J. P. Youngblood, *ACS Sustain. Chem. Eng.* **2016**, 4, 3927.

- [60] X. Xu, F. Liu, L. Jiang, J. Y. Zhu, D. Haagenson, D. P. Wiesenborn, *ACS Appl. Mater. Interfaces* **2013**, *5*, 2999.
- [61] M. S. Peresin, Y. Habibi, J. O. Zoppe, J. J. Pawlak, O. J. Rojas, *Biomacromolecules* **2010**, *11*, 674.
- [62] C. M. Clarkson, G. Schueneman, J. Synder, J. P. J. P. Youngblood, *Green Mater.* **2018**, *6*, 1.
- [63] H. Chang, J. Luo, H. C. Liu, A. A. Bakhtiary Davijani, P. H. Wang, G. S. Lolov, R. M. Dwyer, S. Kumar, *Polym. (United Kingdom)* **2017**, *122*, 332.
- [64] H. Chang, A. T. Chien, H. C. Liu, P. H. Wang, B. A. Newcomb, S. Kumar, *ACS Biomater. Sci. Eng.* **2015**, *1*, 610.
- [65] K. Oksman, A. P. Mathew, D. Bondeson, I. Kvien, *Compos. Sci. Technol.* **2006**, *66*, 2776.
- [66] M. Jonoobi, J. Harun, A. P. Mathew, K. Oksman, *Compos. Sci. Technol.* **2010**, *70*, 1742.
- [67] M. J. John, R. Anandjiwala, K. Oksman, A. P. Mathew, *J. Appl. Polym. Sci.* **2013**, *127*, 274.
- [68] J. J. Blaker, K. Y. Lee, M. Walters, M. Drouet, A. Bismarck, *React. Funct. Polym.* **2014**, *85*, 185.
- [69] K. Oksman, Y. Aitomäki, A. P. Mathew, G. Siqueira, Q. Zhou, S. Butylina, S. Tanpichai, X. Zhou, S. Hooshmand, *Compos. Part A Appl. Sci. Manuf.* **2016**, *83*, 2.
- [70] H. Kargarzadeh, I. Ahmad, I. Abdullah, A. Dufresne, S. Y. Zainudin, R. M. Sheltami, *Cellulose* **2012**, *19*, 855.
- [71] N. Lin, A. Dufresne, *Nanoscale* **2014**, *6*, 5384.
- [72] M. Börjesson, K. Sahlin, D. Bernin, G. Westman, *J. Appl. Polym. Sci.* **2018**, *135*, 1.
- [73] S. X. Peng, H. Chang, S. Kumar, R. J. Moon, J. P. Youngblood, *Cellulose* **2016**, *23*, 1825.
- [74] S. Fujisawa, J. Zhang, T. Saito, T. Iwata, A. Isogai, *Polym. (United Kingdom)* **2014**, *55*, 2937.
- [75] E. Kloser, D. G. Gray, *Langmuir* **2010**, *26*, 13450.
- [76] L. Gan, J. Liao, N. Lin, C. Hu, H. Wang, J. Huang, *ACS Omega* **2017**, *2*, 4725.
- [77] S. Fujisawa, T. Saito, S. Kimura, T. Iwata, A. Isogai, *Biomacromolecules* **2013**, *14*, 1541.
- [78] M. J. Sobkowicz, J. R. Dorgan, K. W. Gneshin, A. M. Herring, J. T. McKinnon, *J. Polym. Environ.* **2008**, *16*, 131.

- [79] J. A. Cicero, J. R. Dorgan, J. Janzen, J. Garrett, J. Runt, J. S. Lin, *J. Appl. Polym. Sci.* **2002**, *86*, 2828.
- [80] S. Spinella, G. Lo Re, B. Liu, J. Dorgan, Y. Habibi, P. Leclere, J. M. Raquez, P. Dubois, R. A. Gross, *Polym. (United Kingdom)* **2015**, *65*, 9.
- [81] W. Ding, D. Jahani, E. Chang, A. Alemdar, C. B. Park, M. Sain, *Compos. Part A Appl. Sci. Manuf.* **2016**, *83*, 130.
- [82] B. W. Chieng, N. A. Ibrahim, W. M. Z. W. Yunus, M. Z. Hussein, *J. Appl. Polym. Sci.* **2013**, *130*, 4576.
- [83] K. Sungsanit, N. Kao, S. N. Bhattacharya, *Polym. Eng. Sci.* **2012**, *52*, 108.
- [84] E. E. Ureña-Benavides, C. L. Kitchens, *Macromolecules* **2011**, *44*, 3478.
- [85] J. Peng, T. Ellingham, R. Sabo, L. S. Turng, C. M. Clemons, *Cellulose* **2014**, *21*, 4287.
- [86] R. A. Chowdhury, S. X. Peng, J. Youngblood, *Cellulose* **2017**, *24*, 1957.
- [87] B. E. Read, J. C. Duncan, D. E. Meyer, *Polym. Test.* **1984**, *4*, 143.
- [88] L. . Alexander, *X-Ray Diffraction Methods in Polymer Science*, Krieger Publishing Co., Huntington, NY, **1979**.
- [89] J. J. Hermans, P. H. Hermans, D. Vermaas, A. Weidinger, *Recl. des Trav. Chim. des Pays-Bas* **1946**, *65*, 427.
- [90] L. Fambri, A. Pegoretti, R. Fenner, S. D. Incardona, C. Migliaresi, *Polymer.* **1997**, *38*, 79.
- [91] A. P. Mathew, K. Oksman, M. Sain, *J. Appl. Polym. Sci.* **2006**, *101*, 300.
- [92] S. X. Peng, S. Shrestha, J. P. Youngblood, *Polymer.* **2017**, *114*, 88.
- [93] D. Cheng, Y. Wen, L. Wang, X. An, X. Zhu, Y. Ni, *Carbohydr. Polym.* **2015**, *123*, 157.
- [94] M. S. Reid, H. S. Marway, C. Moran-Hidalgo, M. Villalobos, E. D. Cranston, *Cellulose* **2017**, *24*, 4743.
- [95] V. Khoshkava, M. R. Kamal, *Biomacromolecules* **2013**, *14*, 3155.
- [96] R. Auras, B. Harte, S. Selke, *Macromol. Biosci.* **2004**, *4*, 835.
- [97] O. Martin, L. Avérous, *Polymer.* **2001**, *42*, 6209.
- [98] M. A. Huneault, H. Li, *Polymer.* **2007**, *48*, 270.
- [99] M. Vestena, I. P. Gross, C. M. O. Muller, A. T. N. Pires, *J. Brazillian Chem. Soc.* **2016**, *27*, 905.

- [100] Y. Lu, M. C. Cueva, E. Lara-Curzio, S. Ozcan, *Carbohydr. Polym.* **2015**, *131*, 208.
- [101] D. Garlotta, *J. Polym. Environ.* **2002**, *9*, 63.
- [102] H. Wu, S. Nagarajan, L. Zhou, Y. Duan, J. Zhang, *Polym. (United Kingdom)* **2016**, *103*, 365.
- [103] Y. He, Z. Fan, Y. Hu, T. Wu, J. Wei, S. Li, *Polymer.* **2007**, *43*, 4431.
- [104] B. E. W. Fischer, H. J. Sterzel, G. Wegner, *Polymere* **1973**, *990*, 980.
- [105] P. Pan, Y. Inoue, *Prog. Polym. Sci.* **2009**, *34*, 605.
- [106] J. Zhang, H. Tsuji, I. Noda, Y. Ozaki, *Macromolecules* **2004**, *37*, 6433.
- [107] J. Zhang, K. Tashiro, H. Tsuji, A. J. Domb, *Macromolecules* **2008**, *41*, 1352.
- [108] X. Meng, V. Bocharova, H. Tekinalp, S. Cheng, A. Kisliuk, A. P. Sokolov, V. Kunc, W. H. Peter, S. Ozcan, *Mater. Des.* **2018**, *139*, 188.
- [109] A. T. Lorenzo, M. L. Arnal, J. Albuerno, A. J. Müller, *Polym. Test.* **2007**, *26*, 222.
- [110] J. M. Schultz, *Polymer Crystallization: The Development of Crystalline Order in Thermoplastic Polymers*, Oxford University Press, Inc., New York, **2001**.
- [111] S. Iannace, L. Nicolais, *J. Applie* **1997**, *64*, 911.
- [112] Y. Li, C. Han, Y. Yu, L. Xiao, Y. Shao, *Thermochim. Acta* **2018**, *663*, 67.
- [113] I. Pillin, N. Montrelay, Y. Grohens, *Polymer.* **2006**, *47*, 4676.
- [114] H. Li, M. A. Huneault, *Polymer.* **2007**, *48*, 6855.
- [115] Y. Peng, D. J. Gardner, Y. Han, Z. Cai, M. A. Tshabalala, *J. Colloid Interface Sci.* **2013**, *405*, 85.
- [116] E. Rojo, M. S. Peresin, W. W. Sampson, I. C. Hoeger, J. Vartiainen, J. Laine, O. J. Rojas, *Green Chem.* **2015**, *17*, 1853.
- [117] B. Fiorentino, R. Fulchiron, V. Bounor-Legaré, J. C. Majesté, J. C. Leblond, J. Duchet-Rumeau, *Appl. Clay Sci.* **2015**, *109–110*, 107.
- [118] S. Beck, J. Bouchard, R. Berry, *Biomacromolecules* **2012**, *13*, 1486.
- [119] M. N. Angles, A. Dufresne, *Macromolecules* **2000**, *33*, 8344.
- [120] J. C. Liu, D. J. Martin, R. J. Moon, J. P. Youngblood, *J. Appl. Polym. Sci.* **2015**, *132*, 1.

- [121] T. Kawai, N. Rahman, G. Matsuba, K. Nishida, T. Kanaya, M. Nakano, H. Okamoto, J. Kawada, A. Usuki, N. Honma, K. Nakajima, M. Matsuda, *Macromolecules* **2007**, *40*, 9463.
- [122] H. W. Xiao, P. Li, X. Ren, T. Jiang, J. Yeh, *J. Appl. Polym. Sci.* **2010**, *118*, 3558.
- [123] H. Marand, J. Xu, S. Srinivas, *Macromolecules* **1998**, *31*, 8219.
- [124] H. Tsuji, H. Takai, S. K. Saha, *Polymer*. **2006**, *47*, 3826.
- [125] H. Tsuji, Y. Ikada, *Polymer*. **1995**, *36*, 2709.
- [126] P. Pan, W. Kai, B. Zhu, T. Dong, Y. Inoue, *Macromolecules* **2007**, *40*, 6898.
- [127] G. Z. Papageorgiou, D. S. Achilias, S. Nanaki, T. Beslikas, D. Bikiaris, *Thermochim. Acta* **2010**, *511*, 129.
- [128] G. Sun, L. T. Weng, J. M. Schultz, C. M. Chan, *Polymer*. **2014**, *55*, 1829.
- [129] S. Nurkhamidah, E. M. Woo, *Macromol. Chem. Phys.* **2011**, *212*, 1663.
- [130] S. Nurkhamidah, E. M. Woo, *J. Appl. Polym. Sci.* **2011**, *122*, 1976.
- [131] A. Belous, R. Tchoudakov, A. Tzur, M. Narkis, D. Alperstein, *Polym. Adv. Technol.* **2012**, *23*, 938.
- [132] D. Alperstein, D. Knani, A. Goichman, M. Narkis, *Polym. Bull.* **2012**, *68*, 1977.
- [133] J. M. Younker, R. H. Poladi, H. V. Bendler, H. B. Sunkara, *Polym. Adv. Technol.* **2016**, *27*, 273.
- [134] S. Singh, M. L. Maspoch, K. Oksman, *J. Appl. Polym. Sci.* **2019**, *136*, 1.
- [135] C. M. Hansen, *Hansen Solubility Parameters: A User's Handbook*, CRC Press, **2007AD**.
- [136] F. Gharagheizi, *J. Appl. Polym. Sci.* **2007**, *103*, 31.
- [137] M. Shah, Y. Agrawal, *Pharm. Dev. Technol.* **2013**, *18*, 582.
- [138] A. F. M. Barton, *Handbook of Solubility Parameters and Other Cohesion Parameters*, CRC Press, **1991**.
- [139] "Surface Free Energy Components by Polar/Dispersion and Acid—Base Analyses; and Hansen Solubility Parameters for Various Polymers," can be found under [https://www.accudynetest.com/polytable\\_02.html?rd=self&](https://www.accudynetest.com/polytable_02.html?rd=self&), **n.d.**
- [140] "Hansen Solubility Sphere," **2020**.

## PUBLICATIONS

- **Clarkson, C. M.**; Mccoy, J. D.; Kropka, J. M. Enthalpy Recovery and Its Relation to Shear Response in an Amine Cured DGEBA Epoxy. *Polymer*. **2016**, 94, 19–30. DOI: 10.1016/j.polymer.2016.03.095
- Mccoy, J. D.; Ancipink, W. B.; **Clarkson, C. M.**; Kropka, J. M.; Celina, M. C.; Giron, N. H.; Hailesilassie, L.; Fredj, N. Cure Mechanisms of Diglycidyl Ether of Bisphenol A (DGEBA) Epoxy with Diethanolamine. *Polymer*. **2016**, 105, 243–254. DOI: 10.1016/j.polymer.2016.10.028
- **Clarkson, C. M.**; Schueneman, G.; Synder, J.; Youngblood, J. P. Dry-Spinning of Cellulose Nanocrystal/ Polylactic Acid Composite Fibers. *Green Materials*. **2018**, 6 (1), 1–9. DOI: 10.1680/jgrma.17.00027
- Chowdhury, R. A.; **Clarkson, C.**; Youngblood, J. Continuous Roll-to-Roll Fabrication of Transparent Cellulose Nanocrystal (CNC) Coatings with Controlled Anisotropy. *Cellulose* **2018**, 25 (3), 1769–1781. DOI: 10.1007/s10570-018-1688-4
- Chowdhury, R.A.; **Clarkson, C.**; Apalangya, V.A.; Naeemul Islam, S.M.; Youngblood, J.P. Roll-to-roll of cellulose nanocrystal-poly(vinyl alcohol) composite coatings with controlled anisotropy. *Cellulose* **2018**, 25 (11), 6547-6560. DOI: 10.1007/s10570-018-2019-
- Chowdhury, R., Nuruddin, MD, **Clarkson, C.M.**, Montes, F., Howarter, J., Youngblood, J.P. Cellulose Nanocrystal (CNC) Coatings with Controlled Anisotropy as High-Performance Gas Barrier Films. *ACS Applied Materials & Interfaces* **2019**, (11) 1376-1383. DOI: 10.1021/acsami.8b16897
- **Clarkson, C.M.**; El AwadAzrak, S.; Chowdhury, R.; Shuvo, S.N.; Synder, J.; Schueneman, G.; Ortalan, V.; Youngblood, J.P. Melt Spinning of Cellulose Nanofibril/Poly(lactic acid) Composite Fibers for High Stiffness. *ACS Applied Polymer Materials* **2019**, 1 (2) 166-168. DOI: 10.1021/acsapm.8b00030
- El Awad Azrak, S.; **Clarkson, C.M.**; Moon, R.J.; Schueneman, G.T.; Youngblood, J.P. Wet-stacking lamination of multi-layer mechanically fibrillated cellulose nanofibrils (CNF) sheets with increased mechanical performance for use in high-strength and light-weight structural and packaging applications **2019** DOI: 10.1021/acsapm.9b00635

- Chowdhury, R.A.; **Clarkson, C.M.**; Shrestha, S.; El Awad Azrak, S.M.; Maylan, M.; Youngblood, J.P. High-Performance Water-Borne Polyurethane Coatings Based on a Blocked Isocyanate with Cellulose Nanocrystals (CNC) as the Polyol. *ACS Applied Polymer Materials* **2019**, DOI: 10.1021/acsapm.9b00849
- **Clarkson, C. M.**; El Awad Azrak, S. M.; Snyder, J.; Schueneman, G.; Youngblood, J. P. Crystallization Kinetics and Morphology of Small Concentrations of Cellulose Nanofibrils (CNFs) and Cellulose Nanocrystals (CNCs) Melt-Compounded into Poly(lactic acid) (PLA) with Plasticizer. *Polymer* **2020**, 187, DOI: 10.1016/j.polymer.2019.122101
- **Clarkson, C.M.**; El Awad Azrak, S.M.; Forti, E.S.; Schueneman, G.T.; Moon, R.J.; Youngblood, J.P. Progress Report on Recent Developments in Cellulose Nanomaterial Composites. *Accepted to Advanced Materials*
- Korey, M.; **Clarkson, C.M.**; Frost, K.D.; Andler, J.; Wang, C.; Reeves, M.; Handwerker, C. Critical Incident Assessment as a Tool to Reflect on Student's Emotional Response During Internal Experiences. *Accepted March. 23<sup>rd</sup>, 2020 to ASEE*
- Wang, C.; **Clarkson, C.M.**; Korey, M.; Frost, K.D.; Andler, J.; Reeves, M.; Handwerker, C. Lessons Learned from the IGERT Sustainable Electronics Program: Cultivating Student Motivation in an Interdisciplinary and International Group. *Accepted March. 23<sup>rd</sup>, 2020 to ASEE*